

A Verification Suite of Test Cases for the Barotropic Solver of Ocean Models

Siddhartha Bishnu¹, Mark R. Petersen², Bryan Quaife³, and Joseph Arthur Schoonover⁴

¹Los Alamos National Laboratory

²Los Alamos National Laboratory (DOE)

³Florida State University

⁴Fluid Numerics, LLC

March 29, 2024

Abstract

The development of any atmosphere or ocean model warrants a suite of test cases to verify its spatial and temporal discretizations, order of accuracy, stability, reproducibility, portability, scalability, etc. In this paper, we present a suite of shallow water test cases designed to verify the barotropic solver of atmosphere and ocean models. These include the non-dispersive coastal Kelvin wave; the dispersive inertia-gravity wave; the dispersive planetary and topographic Rossby waves; the barotropic tide; and a non-linear manufactured solution. These test cases check the implementation of the linear pressure gradient term; the linear constant or variable-coefficient Coriolis and bathymetry terms; and the non-linear advection terms. Simulation results are presented for a variety of time-stepping methods as well as two spatial discretizations: a mimetic finite volume method based on the TRiSK scheme, and a high-order discontinuous Galerkin spectral element method. We explain the strategies that need to be adopted for specifying initial and non-periodic boundary conditions on hexagonal meshes. Convergence studies of every test case are conducted with refinement in both space and time, only in space, and only in time. The convergence slopes match the expected theoretical predictions.

A Verification Suite of Test Cases for the Barotropic Solver of Ocean Models

Siddhartha Bishnu^{1,2,5}, Mark R. Petersen¹, Bryan Quaife^{2,3}, and Joseph Schoonover⁴

¹Computational Physics and Methods Group, Los Alamos National Laboratory

²Department of Scientific Computing, Florida State University

³Geophysical Fluid Dynamics Institute, Florida State University

⁴Fluid Numerics

⁵Department of Earth, Atmospheric, and Planetary Sciences, Massachusetts Institute of Technology

Key Points:

- A suite of test cases is presented for the verification of barotropic dynamics of ocean models, with exact and manufactured solutions.
- Specifications are provided for the coastal Kelvin wave, the inertia-gravity wave, the planetary and topographic Rossby waves, the barotropic tide, and non-linear cases.
- Results are presented for a variety of time-stepping methods and two types of spatial discretizations: TRiSK and Discontinuous Galerkin Spectral Element Method.

Abstract

The development of any atmosphere or ocean model warrants a suite of test cases to verify its spatial and temporal discretizations, order of accuracy, stability, reproducibility, portability, scalability, etc. In this paper, we present a suite of shallow water test cases designed to verify the barotropic solver of atmosphere and ocean models. These include the non-dispersive coastal Kelvin wave; the dispersive inertia-gravity wave; the dispersive planetary and topographic Rossby waves; the barotropic tide; and a non-linear manufactured solution. These test cases check the implementation of the linear pressure gradient term; the linear constant or variable-coefficient Coriolis and bathymetry terms; and the non-linear advection terms. Simulation results are presented for a variety of time-stepping methods as well as two spatial discretizations: a mimetic finite volume method based on the TRiSK scheme, and a high-order discontinuous Galerkin spectral element method. The experimental procedure for conducting these numerical experiments is detailed. It underscores several key considerations that vary depending on the chosen spatial discretization method. Finally, convergence studies of every test case are conducted with refinement in both space and time, only in space, and only in time. The convergence slopes match the expected theoretical predictions.

Plain Language Summary

Before running an atmosphere, ocean, or a coupled climate simulation, every model developer should ensure the correct implementation of each term in the governing equations that drive the models forward in time. This motivates the development of idealized test cases, each of which verifies a subset of terms in the governing equations with different initial and boundary conditions. Here we present a suite of six test cases for the momentum equation and sea surface height equation for ocean models in a single-layer configuration. The computed results from the ocean model can be compared to exact solutions. The computed solution always has a small error, but is said to converge to the exact solution with reduction in grid cell size and time step. If the model converges at the expected rate, then we know that it is solving the governing equations correctly. We show results of convergence tests from two models, and share the full specifications of these test cases so that other ocean modelers may reproduce them.

1 Introduction

The verification of spatial and temporal discretizations is an important step in the development of any computational physics model based on partial differential equations (PDEs). Verification suites, with tests of increasing complexity that exercise a subset of terms, are particularly useful to identify problems as well as to compare discretization methods. Analysis metrics include the order of accuracy, stability, reproducibility, portability, computational performance, and scalability to large core counts. Atmosphere and ocean models are no different in this regard. Numerous test cases (TC) have been implemented in these models for benchmarking their results and performance against accepted standards (Bishnu et al., 2023). In this introduction, we provide an overview of the most influential test cases for geophysical fluids, and those that inspired the development of this paper. Additionally, we show that the shallow water test cases presented here satisfy a need in ocean model verification that is not provided in previous publications.

We start with the work of D. L. Williamson et al. (1992) that was published over three decades ago. They introduced a set of seven test cases for the discretized shallow water equations in a spherical geometry:

- (i) advection of a cosine bell with compact support around the sphere;
- (ii) a zonal geostrophically balanced flow, which is a steady state solution of the full non-linear shallow water equations;

- 66 (iii) a steady state non-linear zonal geostrophic flow, almost equivalent to (ii), except with
- 67 a compactly supported non-zero wind field;
- 68 (iv) forced non-linear advection of a translating low pressure center superimposed on a jet
- 69 stream that is symmetric about the equator;
- 70 (v) zonal flow impinging on an isolated mountain;
- 71 (vi) Rossby-Haurwitz waves, representing exact solutions to the non-linear nondivergent
- 72 barotropic vorticity equation; and
- 73 (vii) a numerical experiment initialized from observed atmospheric states, with results
- 74 compared to the finest possible resolution.

75 The Williamson test cases have been adopted as verification tools by numerous atmosphere
 76 and ocean models, including spectral element models in spherical geometries (Taylor et al.,
 77 1997; Thomas & Loft, 2002) and continuous Galerkin spectral element dynamical core in
 78 the Community Atmosphere Model (CAM) version 5 (Dennis et al., 2012), computational
 79 performance in CAM Evans et al. (2019), and others (Spotz et al., 2015). The Williamson
 80 cases are so frequently used that they are the canonical set of tests for new geophysical
 81 fluid dynamical cores (Walko & Avissar, 2008; T. D. Ringler et al., 2010). Our group
 82 has recently used Williamson test cases to verify local time-stepping schemes (Capodaglio
 83 & Petersen, 2022) and to measure improvements in stability and accuracy in the TRISK
 84 scheme (Calandrini et al., 2021).

85 The Aqua-Planet Experiment (APE) was first proposed by Neale and Hoskins (2000)
 86 as a benchmark for atmospheric general circulation models (AGCMs), and its aims were
 87 summarized by Blackburn and Hoskins (2013). The model setup consists of an idealised
 88 ocean-covered Earth, thereby eliminating the effect of topography and land on atmospheric
 89 flow. Surface forcing is provided by sea surface temperature varying only in latitude. Such
 90 an intermediate APE is more complex than a dry dynamical core experiment, but simpler
 91 than a full-climate simulation coupled to active land, ocean, and ice models. Therefore, the
 92 APE bridges the gap between realistic simulation and conceptual models of atmospheric
 93 phenomena in the existing modeling hierarchy. Despite these simplifications, APEs have
 94 produced realistic climate features like transient high and low pressure systems, convectively
 95 coupled equatorial waves, and tropical cyclones. Blackburn et al. (2013) compared climate
 96 simulations with 16 atmospheric general circulation models (AGCMs) on an aquaplanet,
 97 with the idealised configuration designed to expose differences in the circulation simulated by
 98 these models. APEs were performed with the variable-resolution spectral element dynamical
 99 core of CAM by Zarzycki et al. (2014), and the fundamental characteristics of the aquaplanet
 100 climate simulated by CAM5.3 are described in Medeiros et al. (2016). Chavas and Reed
 101 (2019) employed APEs under uniform thermal forcing and variable global dynamical forcing
 102 to test existing hypotheses regarding tropical cyclone genesis and size, whereas Merlis and
 103 Held (2019) provided a nice review of tropical cyclone simulations with APEs. Möbis
 104 and Stevens (2012) determined the factors controlling the position of the Intertropical
 105 Convergence Zone (ITCZ) on an aquaplanet. Although the Aquaplanet Experiment (APE)
 106 is predominantly tailored for atmospheric models, when integrated with a global ocean
 107 model, it sheds light on ocean-atmosphere dynamics without the influence of land-sea
 108 disparities and topographical intricacies. For instance, Donohoe et al. (2014) delved into the
 109 impact of the ocean mixed layer depth on climate using a series of slab ocean aquaplanet
 110 simulations.

111 The prominent test cases employed by ocean models to quantify mixing and diapycnal
 112 transport are:

- 113 (i) the lock exchange or dam break test case to measure mixing in the simplest possible
- 114 configuration (D.-P. Wang (1984), Haidvogel and Beckmann (1999), Jankowski (1999),
- 115 Ilıcak et al. (2012), Kärnä et al. (2013), Petersen et al. (2015), Gibson et al. (2017),
- 116 Kärnä et al. (2018));

- 117 (ii) the overflow test case to investigate the impact of topography on spurious mixing
118 (Haidvogel and Beckmann (1999), Ilıcak et al. (2012), Petersen et al. (2015));
- 119 (iii) the Dynamics of Overflow Mixing and Entrainment (DOME) test case to study the
120 model’s ability to simulate density-driven overflows (Ezer and Mellor (2004), Legg
121 et al. (2006), Q. Wang et al. (2008), Burchard and Rennau (2008), Reckinger et al.
122 (2015), Gibson et al. (2017), Kärnä et al. (2018));
- 123 (iv) the internal wave test case to examine spurious diapycnal mixing associated with
124 the adjustment of an internal gravity wave in a vertically stratified fluid (Ilıcak et al.
125 (2012), Petersen et al. (2015), Gibson et al. (2017));
- 126 (v) the three-dimensional mesoscale baroclinic eddies test case at eddy-permitting grid
127 resolution in the presence of rotation, to measure mixing under conditions closer to
128 a realistic high-resolution global ocean models (Ilıcak et al. (2012), Petersen et al.
129 (2015), Gibson et al. (2017), Kärnä et al. (2018)); and
- 130 (vi) the spin-down of a global ocean climate model at non-eddy and eddy permitting
131 grid resolutions (Ilıcak et al. (2012), Petersen et al. (2015)).

132 The COmmunity MODelling Ocean (COMODO) project was funded by the French
133 National Agency for Research to benchmark and improve existing ocean models and methods,
134 and guide their future evolution. It consisted of the following test cases:

- 135 (i) Stommel gyre test case of Hecht et al. (2000) for testing the conservation of tracers;
- 136 (ii) Adapted Smolarkeiwicz test case for testing the terrain-following coordinate;
- 137 (iii) Lock exchange test case for testing the tracer advection scheme and diapycnal mixing;
- 138 (iv) Barotropic vortex test case for testing the tracer and momentum advection schemes,
139 and the time-stepping method;
- 140 (v) Baroclinic vortex test case for testing the tracer and momentum advection-diffusion
141 schemes, the time-stepping method, and the vertical coordinate;
- 142 (vi) Baroclinic jet test case for testing the effective resolution, the tracer and momentum
143 advection-diffusion schemes, the time-stepping method, and the vertical coordinate;
- 144 (vii) Thacker’s bowl test case for testing the wetting and drying phenomenon, the pressure
145 gradient term, and the vertical coordinate;
- 146 (viii) Two-dimensional vertical upwelling test case for testing the time-stepping method,
147 the vertical coordinate, and the bottom boundary conditions;
- 148 (ix) Internal tide test case for testing the vertical coordinate, the tracer and momentum
149 advection-diffusion schemes, and the pressure gradient term;
- 150 (x) Sea mount test case for testing the tracer and momentum advection-diffusion schemes,
151 the lateral boundary conditions, and the current-topography interactions.

152 The COMODO project paved the way to the successful COMMODORE workshops on the
153 numerical solution techniques of PDEs that govern ocean circulation from global to coastal
154 scales.

155 Two simplified linear models of the stationary quasi-geostrophic equations, namely the
156 Stommel (Stommel, 1948) and Stommel–Munk (Munk & Carrier, 1950) models, have been
157 employed as verification tools by numerous shallow water and barotropic ocean models. The
158 Stommel model can be used to test the ability of an ocean model to reproduce the western
159 intensification phenomenon. The Stommel–Munk model, on the other hand, focuses on
160 the wind-driven gyres and the Ekman spiral, and can be used to test the representation of
161 wind-driven circulation and the response of the ocean surface layer to wind stress. Foster
162 et al. (2013) and Kim et al. (2015) presented conforming finite-element methods of the
163 streamfunction formulation of the stationary one-layer quasi-geostrophic equations for the
164 study of the large scale wind-driven ocean circulation. The finite element discretization in
165 Foster et al. (2013) employed Argyris elements, whereas Kim et al. (2015) used a B-spline
166 basis. Rotundo et al. (2016) presented the error analysis of the method in Kim et al. (2015),
167 and Jiang and Kim (2016) generalized the method to domains with arbitrary shaped coastal
168 boundaries. Myers and Weaver (1995) presented a diagnostic barotropic finite-element ocean

169 circulation model in Cartesian and spherical coordinates, and tested it against the linear
 170 Stommel and Munk models, as well as the barotropic circulation in the North Atlantic
 171 Ocean in the presence of realistic lateral boundaries and topography. Comblen et al.
 172 (2010) considered continuous, discontinuous, as well as partially discontinuous finite element
 173 formulations for the non-conservative shallow water equations, that are second-order accurate
 174 in space. In addition to the linear and non-linear versions of the Stommel and Munk gyres,
 175 the numerical solution was benchmarked against unsteady and steady wave equations, Stokes
 176 flow, and the geostrophic equilibrium. Düben et al. (2012) studied the applicability of a new
 177 finite element in atmosphere and ocean modeling that combines a second-order continuous
 178 representation for the scalar field with a first-order discontinuous representation for the
 179 velocity field. Q. Chen and Ju (2018) proposed conservative finite-volume schemes for solving
 180 the inviscid and viscous quasi-geostrophic equations on coastal-conforming unstructured
 181 primal–dual meshes. They also performed numerical experiments with a freely evolving
 182 circular flow, and the intensified western boundary current. Beel et al. (2019) introduced a
 183 novel strong form-based meshfree collocation method to directly discretize the second-order
 184 Stommel model and the fourth-order Stommel–Munk model for the large-scale wind-driven
 185 ocean circulation simulations.

186 We mention the relevant limited area, coastal, and tidal test cases in the ocean modeling
 187 literature, starting with Drago and Iovenitti (2000). They introduced a three-dimensional
 188 finite-difference model for coastal oceans and evaluated its performance against various
 189 scenarios, including a wind-driven current, a wind and Coriolis force balance, an Ekman
 190 spiral, tidal circulation, tidal flood and ebb on a beach, and a coastal jet influenced by a
 191 long-shore wind. Fringer et al. (2006) discussed the fundamental hydrodynamic kernel of the
 192 Stanford Unstructured Nonhydrostatic Terrain-following Adaptive Navier–Stokes Simulator
 193 (SUNTANS), a finite-volume, unstructured-grid, nonhydrostatic, parallel, coastal-ocean
 194 solver. They tested it against a non-hydrostatic lock exchange test case, a non-hydrostatic
 195 internal seiche test case, and the generation of internal waves in the Monterey Bay region.
 196 Santilli and Scotti (2015) presented the Stratified Ocean Model with Adaptive Refinement
 197 (SOMAR), a computational framework for the evolution of non-hydrostatic, baroclinic
 198 flows encountered in regional and coastal ocean simulations. It combines the flexibility
 199 of Adaptive Mesh Refinement with a set of numerical tools specifically developed to address
 200 the high degree of anisotropy of oceanic flows and the accompanying numerical challenges.
 201 The modeling framework was applied to (1) the lock exchange test case; (2) the beam
 202 generation test case following Jalali et al. (2014) to analyze the generation of internal
 203 waves; and (3) the Dubreil–Jacotin–Long (DJL) solution, which is an exact solution of
 204 the Euler equations. Garcia et al. (2019) validated the nonhydrostatic General Curvilinear
 205 Coastal Ocean Model (GCCOM) for stratified flows against the lock exchange test case; a
 206 three dimensional internal seiche test case; and a field-scale internal wave beams test case,
 207 following the experimental setup of Vitousek and Fringer (2014). Herzfeld et al. (2011)
 208 reviewed some realistic test cases for limited area ocean modelling, including a coastal shelf
 209 model application used for down-scaling; tidal response of a gulf with one open boundary
 210 across the mouth of the gulf; and the response of a coastal region to the passage of a tropical
 211 cyclone.

212 Many atmosphere, ocean and climate models are equipped with test suite creation and
 213 verification infrastructure, in addition to the forward time-stepping core. For example, test
 214 cases for MPAS-Ocean (T. Ringler et al., 2013) are available in the Configuration of Model
 215 for Prediction Across Scales Setups (COMPASS) repository (Asay-Davis et al., 2024) and
 216 more recently the Polaris repository (Asay-Davis & Begeman, 2024). The test cases are often
 217 contained within a separate directory of the model itself, and tutorials for a subset of the test
 218 cases are available on the online manual e.g. MITgcm (Marshall et al., 1997), MOM (Griffies
 219 et al., 2005), SUNTANS (Fringer et al., 2006), or the README file of the Github repository
 220 of the model e.g. Oceananigans (Ramadhan et al., 2020), NEMO (Madec et al., 2023), or
 221 a Wikipedia page e.g. ROMS (Shchepetkin & McWilliams, 2005). Standardized test cases
 222 provide a method to compare the solution quality and computational speed between models,

223 and even between different languages and architectures. For example, Bishnu et al. (2023)
 224 uses the coastal Kelvin wave and inertia-gravity wave cases to compare Fortran-MPI against
 225 Julia-MPI on CPUs and GPUs.

226 1.1 Contributions of this work

227 The majority of test cases mentioned in the introduction of our study are primarily used
 228 for validation, rather than verification. Verification, in simplest terms, investigates ‘if we are
 229 solving the equations right,’ contrasting with validation, which scrutinizes ‘if we are solving
 230 the right equations.’ Verification is a methodical process that quantifies simulation errors,
 231 displays the convergence of the numerical solution towards established benchmarks such
 232 as analytical and manufactured solutions with refinement in space and time, and ensures
 233 software quality. In contrast, code validation delves into whether the models themselves are
 234 representations of the right equations, aiming to assess how well a model mirrors the real
 235 world from the perspective of its intended application. The core objective of validation is
 236 to instill confidence in the model’s predictive capability by comparing it with observed and
 237 experimental data. As a best practice, verification should precede validation to facilitate
 238 precise assessments.

239 Our work with MPAS-Ocean and interactions with fellow ocean modelers has enlightened
 240 us to the dangers of overlooking essential verification steps in favor of more advanced
 241 validation exercises. For instance, bypassing proper verification can inadvertently allow
 242 subtle software bugs to slip through, that are challenging to detect later on. As an illustrative
 243 example, consider a scenario where an implementation error in the spatial discretization of
 244 the non-linear advection term in the continuity equation compromises the spatial order of
 245 accuracy of an ocean model under development. The model remains stable due to the
 246 diffusion terms in the governing equations and the inherent diffusion within the numerical
 247 scheme. It performs satisfactorily against standard validation exercises, thereby arousing no
 248 suspicion. If this ocean model’s predictive capability falls short compared to a more mature
 249 model, one might contemplate enhancing specific attributes like the discretization scheme,
 250 parametrizations, topographic representation, open boundary conditions, or coupling with
 251 other Earth system model components. While some of these modifications may still be
 252 necessary, without definitive evidence, we might completely overlook the possibility of
 253 incorrect implementation of the non-linear advection term. Its cumulative effect over long
 254 simulation times is far from negligible, and rectifying it may significantly improve the model’s
 255 predictive capability. This highlights the imperative of extensive verification exercises—the
 256 primary subject of this paper—before proceeding with model validation. Such meticulous
 257 scrutiny could have exposed the non-linear advection term’s bug early in the model’s
 258 developmental phase, thereby saving valuable time for the developers. Moreover, the creation
 259 of a verification suite, although a one-time investment, can be integrated within an automated
 260 nightly regression suite. This allows for regular examination every time a substantial
 261 modification is introduced into the model, promoting a robust and consistent development
 262 process.

263 In this paper, we present a verification suite of shallow water test cases consisting of
 264 the non-dispersive coastal Kelvin wave, the dispersive inertia-gravity wave, the dispersive
 265 planetary and topographic Rossby waves, the barotropic tide, and a non-linear manufactured
 266 solution specifically designed for the barotropic mode. Our primary motivation for selecting
 267 these shallow water test cases stems from their routine usage in evaluating the dynamical
 268 core of atmosphere and ocean models. Moreover, many of these models are equipped
 269 with a barotropic-baroclinic time-splitting operation. This technique advances the fast,
 270 two-dimensional, depth-independent external gravity waves explicitly with a small barotropic
 271 time step or implicitly with a large one. The residual three-dimensional subsystem, which
 272 models slower internal gravity waves and ocean currents, is advanced using a large baroclinic
 273 time step. This splitting approach substantially enhances the computational efficiency of
 274 the models, often by orders of magnitude, when compared to employing a small time step for

275 the full three-dimensional equations, as dictated by the CFL condition for the fastest wave.
276 Notably, within this framework, the barotropic equations adopt the form of inhomogeneous
277 rotating shallow water equations, with the source term represented by the barotropic average
278 of a subset of terms within the baroclinic momentum equation. As a result, our carefully
279 chosen shallow water test cases can also serve as verification tools for the barotropic solver
280 integrated within these models.

281 A secondary, yet substantial motivation for this research is to furnish model developers
282 with a method to critically assess their code designed to numerically solve fluid dynamics
283 problems, such as those pertaining to the shallow water equations or the hydrostatic primitive
284 equations. Our methodology initiates with a set of governing equations, upon which we
285 apply spatial and temporal discretizations. We then implement this discretized formulation
286 into the code. Our approach leverages fundamental knowledge of classical geophysical
287 phenomena such as non-dispersive and dispersive geophysical waves, which can be modeled
288 by the code. So, we devise straightforward test cases, beginning with linear ones, and then
289 progressing to non-linear ones. This ensures that we accurately capture the behaviors of
290 these geophysical phenomena. After all, correctly modeling basic problems is foundational to
291 successful oceanic modeling, not to mention the development of general circulation models
292 (GCMs). However, securing the correct answer using a fixed spatial grid and time step
293 size is insufficient. It is essential to perform refinement in spatial grid size and time step
294 to demonstrate the attainment of the appropriate convergence rate. In essence, this not
295 only verifies that the correct solution is achieved but also assures that it is achieved for the
296 correct underlying reasons. If the correct convergence rate is not obtained, the numerical
297 method or its implementation may be flawed, and any successful result could be coincidental
298 rather than systematic. Our robust set of test cases is therefore an invaluable resource
299 for anyone engaged in the development of a GCM. At some stage in the development
300 process, the accurate resolution of the shallow water equations is almost inevitably required.
301 Moreover, the present work elucidates a comprehensive process for evaluating both the
302 physical and numerical correctness of the code. Through carefully chosen examples, this
303 paper aims to demonstrate not only the methodology but also the underlying principles,
304 thereby contributing a vital tool for future developments in the field of ocean modeling.

305 Equally pivotal, and forming the third cornerstone of our paper's objectives, is its
306 pedagogical value, particularly in enriching the curriculum of geophysical fluid dynamics
307 courses. This work extends beyond theoretical concepts, providing a practical, hands-on
308 approach to learning. By integrating the physical characteristics of various geophysical
309 waves (Sections 2.5, 2.6, 2.7, and 2.8), including equatorial waves (Section A2), with their
310 numerical simulations, this work bridges the gap between theory and practice. Students can
311 visualize and appreciate the dynamic evolution of these waves, enhancing their understanding
312 of these complex geophysical phenomena. Moreover, the paper equips students with the
313 tools and knowledge to critically evaluate the accuracy of numerical ocean models, or even
314 a basic code they develop for visualizing geophysical waves. They can verify the correctness
315 of the discretized equations of motion implemented in these models, by ensuring that the
316 numerical solution convergences at the expected theoretical rate based on the spatial and
317 temporal orders of accuracy.

318 Among the cited literature, the seven cases of D. L. Williamson et al. (1992), the
319 Stommel and Stommel-Munk test cases, and the COMODO barotropic vortex test case are
320 specifically designed for shallow water equations. Only test cases (i)–(iv) of D. L. Williamson
321 et al. (1992), the Stommel, and Stommel-Munk test cases are equipped with exact solutions.
322 However, the exact solution of the fluid layer depth of test case (iii) and the exact solution
323 of all the prognostic variables of test case (iv) of D. L. Williamson et al. (1992) consists
324 of an integral which is difficult to evaluate analytically, and is computed using numerical
325 quadrature. The exact solutions of test cases (ii) and (iii) of D. L. Williamson et al. (1992)
326 as well as the Stommel and Stommel-Munk test cases are steady-state solutions. The
327 remaining test cases, meant for validation rather than verification, investigate anomalous

328 mixing, coastal processes, etc., but not the accuracy of the barotropic solver in a split
 329 baroclinic-barotropic time stepping scheme. To properly test the accuracy of the barotropic
 330 solver, the existence of analytical time-dependent solutions is crucial. They serve as a
 331 benchmark, towards which the numerical solutions are expected to converge, when refined
 332 simultaneously in both space and time. The creation of our test cases arose from these
 333 practical needs during the development and improvement of MPAS-Ocean. Although the
 334 exact solutions of some of these test cases are provided in standard geophysical fluid dynamics
 335 textbooks e.g. Cushman-Roisin and Beckers (2011), this work contributes to the development
 336 of a standard verification suite by providing specific details of the initial and boundary
 337 conditions, error plots, and rates of convergence, that will be useful for comparison with
 338 other ocean models.

339 The structure of this paper is organized as follows: Section 2 provides the essential
 340 theoretical foundation on the shallow water equations and offers a concise overview of the test
 341 cases, which encompass geophysical waves, barotropic tide, and a non-linear manufactured
 342 solution. In Section 3, we discuss the spatial and temporal discretizations applied to
 343 the prognostic equations. Our study employs two types of spatial discretizations: (1) a
 344 mimetic finite volume based on the TRiSK scheme and used in MPAS-Ocean; and (2) a
 345 high-order Discontinuous Galerkin Spectral Element Method implemented in the Spectral
 346 Element Library in Fortran (SELF). The prognostic equations are advanced using a variety
 347 of time-stepping methods. Section 6 presents the numerical results, including time evolution
 348 of the error as well as convergence plots with refinement in both space and time, only
 349 in space, and only in time. Conclusions are drawn in Section 7. Appendix A outlines
 350 an additional suite of shallow water test cases with exact solutions, consisting of a plane
 351 wave, diffusion, advection-diffusion, a moving shock, as well as non-dispersive and dispersive
 352 equatorial waves. Appendix B underscores the relevance of the shallow water test cases in the
 353 context of baroclinic-barotropic splitting in oceanic models, illustrating how the barotropic
 354 equations align with the form of inhomogeneous rotating shallow water equations. Finally,
 355 Appendix C delves into nuanced aspects of the numerical implementation, including the
 356 specification of initial and boundary conditions on hexagonal meshes, and the interpolation
 357 of the numerical solution or the error to the coarsest mesh for refinement only in space.

358 **2 A Verification Suite of Shallow Water Test Cases**

359 We have developed a verification suite for shallow water cases, starting with linear
 360 test cases before advancing to non-linear ones. With each test case, we incrementally
 361 introduce a new layer of complexity, enabling us to verify the implementation of every
 362 term in the equations governing barotropic motion and the shallow water core in ocean
 363 models. The linear test cases, consisting of the linear geophysical waves and the barotropic
 364 tide, are tailored to verify the pressure gradient, Coriolis, and linearized advection terms.
 365 Conversely, the non-linear test cases, encompassing the non-linear planetary and topographic
 366 Rossby waves, along with the manufactured solution, prove instrumental for examining the
 367 non-linear advection terms. The source term in the manufactured solutions can exemplify
 368 the barotropic average of the baroclinic terms found on the right-hand side of the barotropic
 369 equations.

370 Although lacking exact solutions, we have incorporated the Rossby waves into our
 371 verification suite for several compelling reasons. First, these comprehensive test cases, in
 372 their non-linear form, verify the implementation of each and every term in the non-linear
 373 shallow water equations. Second, they feature non-trivial variations in the meridional
 374 gradient of the Coriolis parameter and the bottom topography (Section 2.4). Third, Rossby
 375 wave test cases illustrate that exact solutions are not a prerequisite for verifying the model's
 376 spatial and temporal orders of accuracy. This can be achieved by plotting the norm of
 377 the differences between numerical solutions over successive pairs of spatial and temporal
 378 resolutions, refined at a constant ratio, instead of the actual error norm (Section 4.5).

379 Finally, these test cases significantly contribute to the educational aspect of our research
 380 (Section 1.1).

381 Building on the rationale for including Rossby waves in our verification suite, it is
 382 important to clarify that the second reason does not diminish the value of test cases with
 383 exact solutions. In fact, the actual error norm of the numerical solution, defined only
 384 for these test cases, converges under the simultaneous spatial and temporal refinement
 385 (Section 4.3). Additionally, it is worth noting that for certain test cases and specific
 386 resolution ranges, the norm of differences between numerical solutions over a pair of spatial
 387 or temporal resolution, may be minimal and susceptible to overshadowing by round-off
 388 errors. This scenario underscores the need for additional test cases, preferably those with
 389 exact solutions, to ensure comprehensive verification (Section 6.1, bullet point 10).

390 Before delving into detailed descriptions of the various test cases, we provide a brief
 391 theoretical overview of equations representing shallow water and barotropic flows.

392 2.1 The Shallow Water Equations

393 The non-linear rotating shallow water equations, representing the shallow water core
 394 of ocean models, can be expressed compactly as

$$\mathbf{u}_t + \mathbf{u} \cdot \nabla \mathbf{u} + f \mathbf{k} \times \mathbf{u} = -g \nabla(h + b) + \nu \nabla^2 \mathbf{u}, \quad (1a)$$

$$h_t + \nabla \cdot (h \mathbf{u}) = 0, \quad (1b)$$

395 where $\mathbf{u}(x, y, t) = u(x, y, t)\mathbf{i} + v(x, y, t)\mathbf{j}$ is the velocity vector, $h(x, y, t)$ is the shallow water
 396 layer thickness above the bottom topography $b(x, y)$ originating at $z = 0$, $\eta(x, y, t)$ is the
 397 surface elevation, f is the Coriolis parameter, g is the acceleration due to gravity, and ν is
 398 the horizontal viscosity. The subscripts denote partial differentiation, and \mathbf{i} , \mathbf{j} , and \mathbf{k} are
 399 the unit vectors in the x , y and z directions. If H represents the mean depth of the fluid at
 400 rest, then the surface elevation $\eta(x, y, t)$ at any point in time satisfies

$$\eta(x, y, t) = h(x, y, t) + b(x, y) - H, \quad (2)$$

401 Using (2) and replacing the non-linear advection term in (1a) with the right-hand side of
 402 the vector identity

$$\mathbf{u} \cdot \nabla \mathbf{u} = (\nabla \times \mathbf{u}) \times \mathbf{u} + \nabla \frac{|\mathbf{u}|^2}{2} = \{\mathbf{k} \cdot (\nabla \times \mathbf{u})\} \mathbf{k} \times \mathbf{u} + \nabla \frac{|\mathbf{u}|^2}{2}, \quad (3)$$

403 we obtain the vector-invariant form of the momentum equation

$$\mathbf{u}_t + \nabla K + (\zeta + f) \mathbf{u}^\perp = -g \nabla \eta + \nu \nabla^2 \mathbf{u}. \quad (4)$$

404 Here $\mathbf{u}^\perp = \mathbf{k} \times \mathbf{u}$, $K = |\mathbf{u}|^2/2$ is the kinetic energy, and $\zeta = \mathbf{k} \cdot (\nabla \times \mathbf{u})$ is the relative
 405 vorticity.

406 2.2 The Barotropic Equations

407 The barotropic equations of an ocean model can be expressed in vector-invariant form

$$\bar{\mathbf{u}}_t + f \bar{\mathbf{u}}^\perp = -g \nabla \eta + \nu \nabla^2 \bar{\mathbf{u}} + \bar{\mathbf{G}}, \quad (5a)$$

$$\eta_t + \nabla \cdot (h_{\text{total}} \bar{\mathbf{u}}) = 0, \quad (5b)$$

408 where $h_{\text{total}} = \sum_{k=1}^N h_k$ is the total depth equivalent to the sum of individual layer thicknesses
 409 h_k , $\bar{\mathbf{u}} = \left(\sum_{k=1}^N h_k \mathbf{u} \right) / h_{\text{total}}$ is the barotropic velocity, and $\bar{\mathbf{G}}$ is the barotropic average
 410 of specific baroclinic terms. Typically, the diffusion term $\nu \nabla^2 \bar{\mathbf{u}}$ is encapsulated within
 411 $\bar{\mathbf{G}}$, and it does not explicitly feature in the barotropic momentum equation (5a), except
 412 in some variants such as Blumberg and Mellor (1987). A comprehensive demonstration

of the barotropic-baroclinic splitting procedure, alongside a derivation of the barotropic equations of motion using MPAS-Ocean as a case study, can be found in Appendix B. In an analytical comparison against the shallow water equations (1), it becomes evident that the barotropic equations (5) essentially mirror the form of (1), albeit with some key differences: the exclusion of the non-linear advection term and the introduction of the source term $\overline{\mathbf{G}}$ in the momentum equation, and the substitution of the shallow water velocity and layer thickness by the barotropic velocity $\overline{\mathbf{u}}$ and the total depth h_{total} respectively.

The shallow water and barotropic equations can be succinctly expressed as the following set of equations:

$$u_t + \underbrace{\nabla K}_{(1)} + \underbrace{\zeta \mathbf{u}^\perp}_{(2)} + \underbrace{f_0 \mathbf{u}^\perp}_{(3)} + \underbrace{\beta_0 y \mathbf{u}^\perp}_{(4)} = - \underbrace{g \nabla \eta}_{(5)} + \underbrace{\nu \nabla^2 \mathbf{u}}_{(6)} + \underbrace{\overline{\mathbf{G}}}_{(7)}, \quad (6a)$$

$$\eta_t + \underbrace{\nabla \cdot (H \mathbf{u})}_{(8)} + \underbrace{\nabla \cdot (\eta \mathbf{u})}_{(9)} - \underbrace{\nabla \cdot (b \mathbf{u})}_{(10)} = 0, \quad (6b)$$

where the Coriolis parameter f has been decomposed into its leading-order components: f_0 , the base Coriolis parameter at a reference latitude, and $\beta_0 y$, where β_0 is the meridional gradient of f . The non-linear advection term in the continuity equation has been split into three parts using (2). Each term in (6), excluding the temporal derivatives, is labeled for convenient referencing in test cases that verify its numerical implementation.

2.3 Shallow Water Equations in Cartesian Coordinates

The inviscid rotating shallow water equations in Cartesian coordinates are

$$u_t + uu_x + vu_y - fv = -g(h+b)_x, \quad (7a)$$

$$v_t + uv_x + vv_y + fu = -g(h+b)_y, \quad (7b)$$

$$h_t + (hu)_x + (hv)_y = 0. \quad (7c)$$

Inserting (2) into (7), we obtain

$$u_t + uu_x + vu_y - fv = -g\eta_x, \quad (8a)$$

$$v_t + uv_x + vv_y + fu = -g\eta_y, \quad (8b)$$

$$\eta_t + (hu)_x + (hv)_y = 0. \quad (8c)$$

The geophysical waves consisting of the coastal Kelvin wave, the inertia-gravity wave, and the planetary and topographic Rossby waves are solutions to the linearized rotating inviscid shallow water equations, obtained by dropping the non-linear terms in (8) as

$$u_t - fv = -g\eta_x, \quad (9a)$$

$$v_t + fu = -g\eta_y, \quad (9b)$$

$$\eta_t + \{(H-b)u\}_x + \{(H-b)v\}_y = 0. \quad (9c)$$

In the case of a flat bottom, $b(x, y) = 0$, $h(x, y, t) = H + \eta(x, y, t)$, and (9) reduces to

$$u_t - fv = -g\eta_x, \quad (10a)$$

$$v_t + fu = -g\eta_y, \quad (10b)$$

$$\eta_t + H(u_x + v_y) = 0. \quad (10c)$$

In the subsequent subsections, we review the exact solutions associated with the various test cases, which we have numbered 1–6 for convenient reference. The derivations of these exact solutions, particularly for some of the geophysical wave test cases, can be found in standard textbooks on geophysical fluid dynamics (GFD), such as those by Vallis (2017), Cushman-Roisin and Beckers (2011), Pedlosky (1987), and Gill (2016).

439

2.4 Summary of Shallow Water Test Cases

440

441

442

443

444

445

446

447

448

449

450

451

452

453

454

455

456

457

458

459

460

461

The test cases presented in the following sections, summarized in Table 1, assess the numerical implementation of various terms within the rotating shallow water equations. Each of them incorporates the Coriolis force, which imparts rotation to the shallow water. The Coriolis term is constant, rendering the domain of motion to be an *f-plane* for all but the planetary Rossby wave test case, where the Coriolis term is a linear function of y and the domain of wave motion is a *beta-plane*. The topographic Rossby wave test case uniquely features a sloping bottom as a linear function of y , while others possess a flat bottom. With the meridional gradient of the Coriolis parameter and the bottom topography being non-trivial for the planetary and the topographic Rossby waves respectively, the shallow water systems for these solutions are variable-coefficient. In contrast, the systems for other test cases remain constant-coefficient. The non-linear planetary and topographic Rossby waves, along with the manufactured solution test case verify the implementation of the non-linear advection terms. In fact, the non-linear Rossby wave test cases check every term in the non-linear homogeneous shallow water equations. On the other hand, the coastal Kelvin wave, inertia-gravity wave, linear Rossby waves, and the barotropic tide are solutions to the linearized form of these equations, thus their governing PDEs are stripped of non-linear terms. Table 1 concisely captures the assumptions underpinning the geophysical waves, the barotropic tide, and the non-linear manufactured solution. This table details the nature of the simplified PDEs for the shallow water equations, applied boundary conditions, and the specific terms from (6) that are tested. In the context of convergence studies, where extensive simulation times are unnecessary, the diffusion terms for the non-linear Rossby wave test cases are discretionary and are denoted with an asterisk.

Table 1. Summary of assumptions for the geophysical waves, barotropic tide, and non-linear manufactured solution, detailing the nature of the corresponding simplified PDEs for the shallow water equations, their applied boundary conditions, and the specific terms tested from (6), with optional ones indicated by an asterisk.

	Coriolis Parameter	Bottom Topography	Numerical PDE	Boundary Conditions	Terms Verified in Equation (6)
1. Coastal Kelvin Wave	Constant (<i>f-plane</i>)	Flat Bottom	Linear, Homogeneous, Constant-Coefficient	Non-Periodic in x Periodic in y	(3), (5), (8)
2. Inertia-Gravity Wave	Constant (<i>f-plane</i>)	Flat Bottom	Linear, Homogeneous, Constant-Coefficient	Periodic in x Periodic in y	(3), (5), (8)
3a. Planetary Rossby Wave	Linear in y (<i>beta-plane</i>)	Flat Bottom	Linear, Homogeneous, Variable-Coefficient	Radiation or No-Normal Flow	(3), (4), (5), (8)
3b. Planetary Rossby Wave (NL)	Linear in y (<i>beta-plane</i>)	Flat Bottom	Non-Linear , Homogeneous, Variable-Coefficient	Radiation or No-Normal Flow	(1), (2), (3), (4), (5), (6)*, (8), (9)
4a. Topographic Rossby Wave	Constant (<i>f-plane</i>)	Linear in y , Sloping Bottom	Linear, Homogeneous, Variable-Coefficient	Radiation or No-Normal Flow	(3), (5), (8), (10)
4b. Topographic Rossby Wave (NL)	Constant (<i>f-plane</i>)	Linear in y , Sloping Bottom	Non-Linear , Homogeneous, Variable-Coefficient	Radiation or No-Normal Flow	(1), (2), (3), (5), (6)*, (8), (9), (10)
5. Barotropic Tide	Constant (<i>f-plane</i>)	Flat Bottom	Linear, Homogeneous, Constant-Coefficient	Non-Periodic in x , Non-Periodic in y	(3), (5) (8)
6. Manufactured Solution	Constant (<i>f-plane</i>)	Flat Bottom	Non-Linear, Inhomogeneous, Constant-Coefficient	Periodic in x , Periodic in y	(1), (2), (3), (5), (7), (8), (9)

462

2.5 Test Case 1: Coastal Kelvin Wave

463

464

465

A Kelvin wave is a lateral disturbance that requires the presence of a topographic boundary e.g. the oceanic coast or a waveguide e.g. the equator. As the name implies, the coastal Kelvin wave belongs to the topographic boundary category and is therefore a

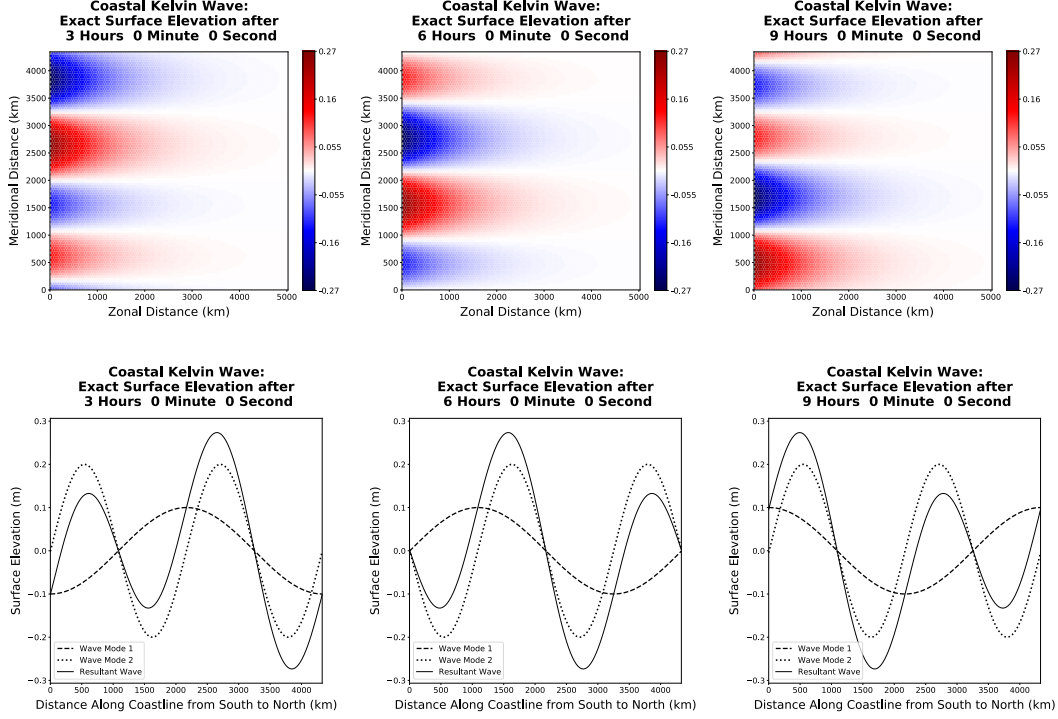


Figure 1. Time evolution of the exact surface elevation of TC1, the non-dispersive coastal Kelvin wave, in the entire domain (first row), and along the coastline (second row), with dashed and dotted lines representing component wave modes, and the solid line representing the resultant wave.

466 common phenomenon along coastlines. It travels with the coast on its right in the Northern
 467 Hemisphere and with the coast on its left in the Southern Hemisphere. Its amplitude
 468 decreases exponentially away from the coast with a decay scale equal to the barotropic
 469 Rossby radius of deformation. This is why the coastal Kelvin wave appears to be ‘trapped’
 470 near the coast. It is non-dispersive which causes the coastal Kelvin wave to preserve its
 471 initial profile as it propagates in the alongshore direction over time.

472 Following the derivation in Cushman-Roisin and Beckers (2011), if the coastline is
 473 aligned along the y -axis ($x = 0$) and we specify $u = 0$ throughout the domain, we arrive at
 474 the physically feasible general solution

$$u = 0, \quad (11)$$

$$v = \sqrt{g\overline{H}F}(y + ct)e^{-x/R}, \quad (12)$$

$$\eta = -HF(y + ct)e^{-x/R}. \quad (13)$$

475 Here $R = c/f = \sqrt{g\overline{H}}/f$ is the barotropic Rossby radius of deformation, a length scale where
 476 rotational effects are considered important. From (12) and (13), we observe that R is also a
 477 measure of the trapping distance of the Kelvin wave from the coast. The dispersion relation
 478 of a coastal Kelvin wave mode with angular frequency ω and meridional wavenumber k_y
 479 is $\omega = ck_y$, where the wave speed $c = \sqrt{g\overline{H}}$ is independent of k_y , a characteristic of
 480 non-dispersive waves.

481 In our numerical simulations, we choose a sinusoidal meridional profile defined by
 482 $F(y) = \hat{\eta} \sin(k_y y)$. In addition, we designate the exact solution to be a superposition
 483 of two wave modes, with the second mode having twice the amplitude and wavenumber
 484 components compared to the first, i.e., $\hat{\eta}^{(2)} = 2\hat{\eta}^{(1)}$ and $k_y^{(2)} = 2k_y^{(1)}$. Here, $\hat{\eta}^{(1)} = 10^{-4}$

485 m, $k_y^{(1)} = 2\pi/L_y$, and L_y denotes the meridional extent of the domain. For this test case
 486 and subsequent ones, we set $f_0 = 10^{-4} \text{ s}^{-1}$, $g = 10 \text{ m s}^{-2}$ and $H = 10^3 \text{ m}$, yielding
 487 $c = \sqrt{gH} = 100 \text{ m s}^{-1}$ and $R = c/f_0 = 10^6 \text{ m}$. As elaborated in Section 2.7, f_0 is identical
 488 to the Coriolis parameter f on an f -plane, but corresponds to its leading-order component
 489 on a β -plane. The zonal extent is specified as $L_x = 5R = 5 \times 10^6 \text{ m}$, ensuring the wave
 490 amplitude diminishes to virtually zero just west of the open eastern boundary. For all test
 491 cases, the meridional extent is set as $L_y = \sqrt{3}/2L_x$ when modeled with the TRiSK-based
 492 finite volume method, and as $L_y = L_x$ when discretized with the discontinuous Galerkin
 493 spectral element method (DGSEM). Figure 1 presents the temporal evolution of the exact
 494 surface elevation of the coastal Kelvin wave. The first row illustrates the surface elevation
 495 throughout the entire domain, while the second row depicts the surface elevation along the
 496 coastline. Here, dashed and dotted lines denote the component wave modes, with the solid
 497 line indicating the resultant wave. Both component wave modes propagate at identical
 498 phase speeds, a fact that can be confirmed by tracking the crest or trough of the first wave
 499 mode and one crest or trough of the second wave mode, and observing that their relative
 500 positions do not vary over time. This phenomenon leads to the maintenance of the original
 501 resultant profile without distortion, a characteristic anticipated for a non-dispersive wave.

502 2.6 Test Case 2: Inertia-Gravity Wave

503 As discussed in Cushman-Roisin and Beckers (2011), by eliminating the requirement of
 504 a lateral boundary and the constraint $u = 0$, we can assume a Fourier series solution to (10)
 505 of the form

$$\begin{bmatrix} \eta \\ u \\ v \end{bmatrix} = \text{Re} \left\{ \begin{bmatrix} \hat{\eta} \\ \hat{u} \\ \hat{v} \end{bmatrix} e^{i(k_x x + k_y y - \omega t)} \right\}, \quad (14)$$

506 and arrive at the dispersion relation

$$\omega \{ \omega^2 - (c^2 k^2 + f^2) \} = 0, \quad (15)$$

507 where $k = \sqrt{k_x^2 + k_y^2}$. The root $\omega = 0$ corresponds to the steady geostrophic state and the
 508 remaining two roots $\omega = \pm \hat{\omega}$, where $\hat{\omega} = \sqrt{c^2 k^2 + f^2}$, correspond to oppositely-travelling
 509 inertia-gravity waves with super-inertial frequency ($\omega > f$). Since the zonal and meridional
 510 phase speeds, given by $c_x = \omega/k_x$ and $c_y = \omega/k_y$, are functions of the wavenumber
 511 components k_x and k_y , the inertia-gravity wave is dispersive. To arrive at a particular
 512 solution consisting of only the inertia-gravity wave mode $\hat{\omega}$, we replace ω by $\hat{\omega}$ and insert
 513 (14) in (10), which results in

$$-i\hat{\omega}\hat{u} - f\hat{v} = -ik_x g\hat{\eta}, \quad (16a)$$

$$-i\hat{\omega}\hat{v} + f\hat{u} = -ik_y g\hat{\eta}, \quad (16b)$$

$$-i\hat{\omega}\hat{\eta} + iH(k_x\hat{u} + k_y\hat{v}) = 0. \quad (16c)$$

514 We can now solve any two equations of (16) to obtain

$$\hat{u} = \frac{g\hat{\eta}}{\hat{\omega}^2 - f^2} (\hat{\omega}k_x + ifk_y), \quad (17)$$

$$\hat{v} = \frac{g\hat{\eta}}{\hat{\omega}^2 - f^2} (\hat{\omega}k_y - ifk_x), \quad (18)$$

515 and demonstrate that these values of \hat{u} and \hat{v} satisfy the third equation as well. Therefore,
 516 the particular solution consisting of only the inertia-gravity wave mode $\hat{\omega}$ is

$$\eta = \text{Re} \left\{ \hat{\eta} e^{i(k_x x + k_y y - \hat{\omega} t)} \right\}, \quad (19)$$

$$u = \text{Re} \left\{ \frac{g\hat{\eta}}{\hat{\omega}^2 - f^2} (\hat{\omega}k_x + ifk_y) e^{i(k_x x + k_y y - \hat{\omega} t)} \right\}, \quad (20)$$

$$v = \text{Re} \left\{ \frac{g\hat{\eta}}{\hat{\omega}^2 - f^2} (\hat{\omega}k_y - ifk_x) e^{i(k_x x + k_y y - \hat{\omega} t)} \right\}, \quad (21)$$

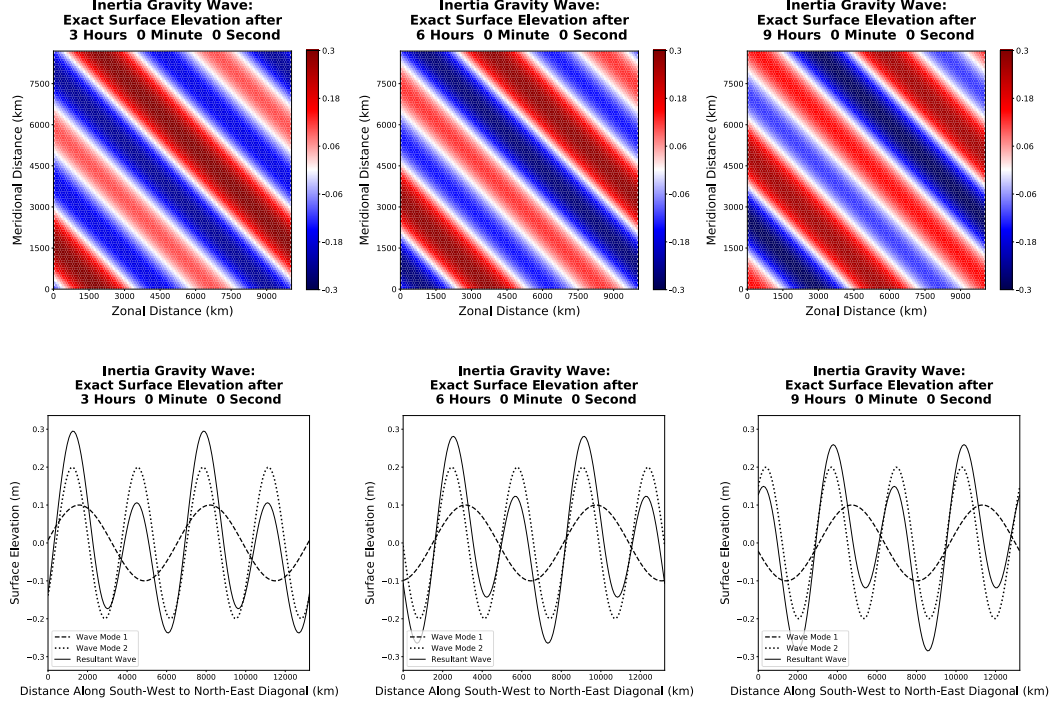


Figure 2. Same as Figure 1, but for TC2, the high-frequency dispersive inertia-gravity wave, with the second row depicting the time evolution of the exact surface elevation and its component wave modes (represented by solid, dashed, and dotted lines respectively) along the south-west to north-east diagonal of the domain.

517 which simplifies to

$$\eta = \hat{\eta} \cos(k_x x + k_y y - \hat{\omega} t), \quad (22)$$

$$u = \frac{g\hat{\eta}}{\hat{\omega}^2 - f^2} \{ \hat{\omega} k_x \cos(k_x x + k_y y - \hat{\omega} t) - f k_y \sin(k_x x + k_y y - \hat{\omega} t) \}, \quad (23)$$

$$v = \frac{g\hat{\eta}}{\hat{\omega}^2 - f^2} \{ \hat{\omega} k_y \cos(k_x x + k_y y - \hat{\omega} t) + f k_x \sin(k_x x + k_y y - \hat{\omega} t) \}. \quad (24)$$

518 We once again specify the exact solution in our numerical simulations to be the sum
 519 of two wave modes, whose amplitudes and wavenumbers satisfy $\hat{\eta}^{(2)} = 2\hat{\eta}^{(1)}$, $k_x^{(2)} = 2k_x^{(1)}$,
 520 and $k_y^{(2)} = 2k_y^{(1)}$, where $\hat{\eta}^{(1)} = 0.1$ m, $L_x = 10^7$ m, $k_x^{(1)} = 2\pi/L_x$, and $k_y^{(1)} = 2\pi/L_y$. The
 521 domain extents L_x and L_y are chosen carefully to ensure that the ratio f/ck ranges between
 522 0.5 and 1.0 for these wave modes, so that both the gravity and the rotational forces play
 523 important roles in their generation. The first row of Figure 2 exhibits the surface elevation
 524 in the entire domain, and the second row depicts the surface elevation along the south-west
 525 to north-east diagonal. With the phase speed now being a function of the wavenumber,
 526 the component wave modes represented by dashed and dotted lines propagate at different
 527 phase speeds (as manifested by the temporal variation in the relative position of the crest or
 528 trough of the first wave mode with respect to a crest or trough of the second wave mode).
 529 This leads to modification of the resultant wave profile (represented by a solid line) with
 530 time, a characteristic that aligns with the behavior of a dispersive wave.

531

2.7 Test Case 3: Planetary Rossby Wave

532

533

534

535

536

537

538

539

540

541

Planetary Rossby waves are low-frequency dispersive waves that feel the rotation of the Earth. They owe their existence to the variation of the Coriolis parameter $f = 2\Omega \sin \theta$ with the latitude θ , where Ω denotes Earth's rotational rate. A Taylor expansion of f around a reference latitude θ_0 , limited to the first two terms, results in $f = f_0 + \beta_0 y$. Here, $f_0 = 2\Omega \sin \theta_0$, $\beta_0 = 2(\Omega/a) \cos \theta_0$, and a represents Earth's radius. A geophysical wave motion's domain is termed a *beta-plane* if the β term is included, and an *f-plane* if not. The *beta-plane* approximation is applicable when $\beta_0 y \ll f_0$ across the domain, implying $\beta = \beta_0 L \ll f_0$, where L indicates the meridional extent of the domain and β is a dimensionless planetary number. For Earth's mid-latitudes, typical values are $f_0 \approx 10^{-4} \text{ s}^{-1}$ and $\beta_0 \approx 2 \times 10^{-11} \text{ m}^{-1} \text{ s}^{-1}$, which we adopt in our numerical simulations as well.

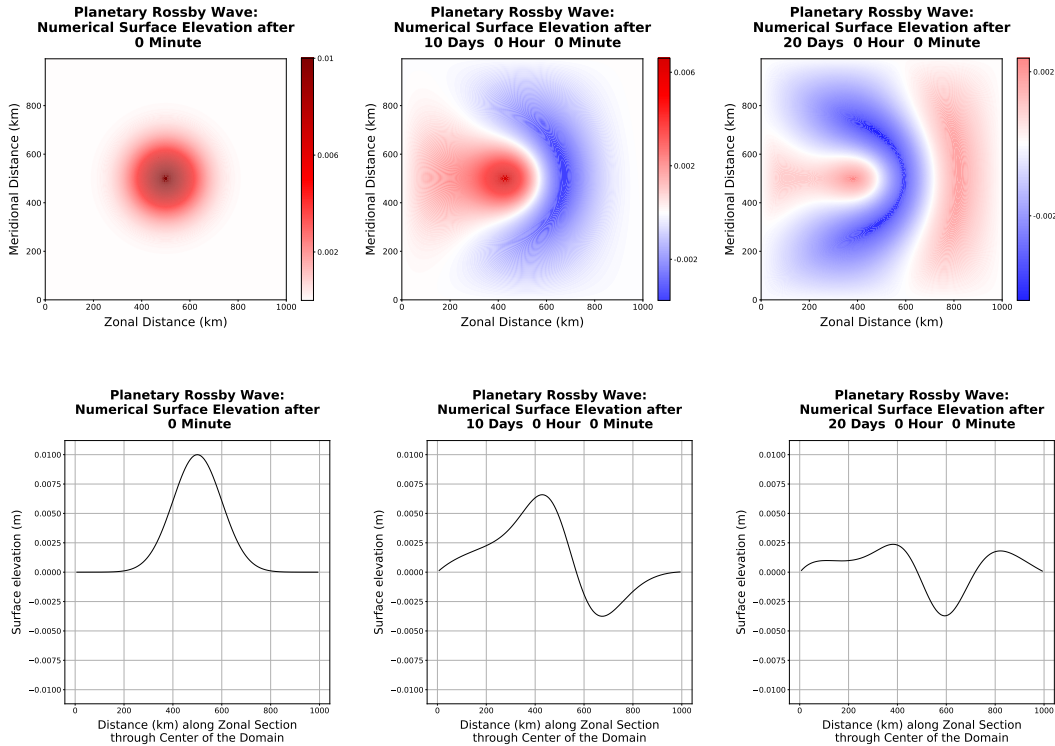


Figure 3. Time evolution of the numerical surface elevation of TC3, the low-frequency dispersive planetary Rossby wave, in the entire domain (first row) and along the zonal section through the domain center (second row), advanced with Williamson's low-storage third-order Runge-Kutta time-stepping method, and spatially discretized with DGSEM using 10 elements and polynomial basis functions of order 7 in each horizontal direction.

542

543

544

545

546

547

548

Planetary Rossby waves represent a slow evolution of steady geostrophic flows, with the velocity field consisting of a leading-order geostrophic term and an ageostrophic perturbation term. Following the derivation in Cushman-Roisin and Beckers (2011), if the velocities are approximated solely by the geostrophic terms and inserted into the momentum equations, a first-order velocity approximation is obtained. Applying these velocities to the continuity equation (10c) yields a constant-coefficient equation, the Fourier series solution of which results in the dispersion relation

$$\omega = -\frac{\beta_0 R^2 k_x}{1 + R^2 (k_x^2 + k_y^2)}. \quad (25)$$

549 For shorter waves, where the length scale $L(\sim 1/k_x \sim 1/k_y) \lesssim R$, we find $\omega \sim \beta_0 L$.
 550 Longer waves, with $L(\sim 1/k_x \sim 1/k_y) \gtrsim R$, yield $\omega \sim \beta_0 R^2/L \lesssim \beta_0 L$. In both cases,
 551 under the assumption $\beta_0 L \ll f_0$, we obtain $\omega \ll f_0$, affirming the subinertial nature of the
 552 planetary Rossby wave. The zonal and meridional phase speeds, represented by $c_x = \omega/k_x$
 553 and $c_y = \omega/k_y$, are clearly functions of the wavenumber components k_x and k_y , thereby
 554 attributing to the wave's dispersive nature. Moreover, the zonal phase speed is invariably
 555 negative, with higher potential vorticity on the right of the propagation direction, resulting
 556 in a phase propagation in westward, northwestward, or southwestward directions.

557 Our attempt to simulate the planetary Rossby wave using the shallow water equations
 558 presents a unique challenge. Since the shallow water equations admit a spectrum of wave
 559 solutions, it is impossible to only extract the low-frequency planetary Rossby waves as a
 560 numerical solution. To simulate the low-frequency planetary Rossby waves, we numerically
 561 solve the linear but variable-coefficient shallow water equations on a *beta-plane*. We specify
 562 the initial surface elevation as a Gaussian blob at the center of the domain, and obtain the
 563 initial velocities using the pressure gradient force and geostrophic balance:

$$\eta(x, y, t = 0) = \hat{\eta} e^{-\{(x-x_0)^2/(2R_x^2) + (y-y_0)^2/(2R_y^2)\}}, \quad (26)$$

$$u(x, y, t = 0) = \frac{g}{f_0 R_y^2} (y - y_0) \hat{\eta} e^{-\{(x-x_0)^2/(2R_x^2) + (y-y_0)^2/(2R_y^2)\}}, \quad (27)$$

$$v(x, y, t = 0) = -\frac{g}{f_0 R_x^2} (x - x_0) \hat{\eta} e^{-\{(x-x_0)^2/(2R_x^2) + (y-y_0)^2/(2R_y^2)\}}. \quad (28)$$

564 Here $\hat{\eta} = 0.01$ m represents the surface elevation amplitude, (x_0, y_0) represents the center
 565 of the domain with zonal extent $L_x = 10^6$ m, and the decay scales R_x and R_y amount to
 566 10% of the zonal and meridional extents of the domain. Time integration results in the
 567 evolution of this ‘geostrophic’ monopole on the *beta-plane*. Since we are not equipped with
 568 the time-dependent exact solutions, we demonstrate high-resolution numerical solutions in
 569 Figure 3 obtained using (a) a high-order discontinuous Galerkin spectral element method
 570 (DGSEM) in space with 10 elements and polynomial basis functions of order 7 in each
 571 horizontal direction, resulting in seventh-order spatial accuracy, and (b) the low-storage
 572 third-order Runge-Kutta method of J. Williamson (1980) in time. The first row illustrates
 573 the time evolution of the numerical surface elevation in the entire domain, and the second
 574 row depicts the same along the zonal section through the domain center. Right after
 575 initialization, some gravity waves radiate out of the monopole towards the domain boundaries.
 576 We impose radiation boundary conditions by setting the external state to a motionless
 577 fluid with no free surface height variation ($u = v = 0, \eta = 0$), leading to the eventual
 578 propagation of the gravity waves out of the domain. Alternatively, if solid wall or no-normal
 579 flow boundary conditions were applied, these gravity waves would continue propagating
 580 along the domain boundaries as coastal Kelvin waves. On a much slower time scale on
 581 the order of the diurnal motion of the Earth, we observe the monopole itself propagating
 582 in the direction of the planetary Rossby waves, with increasing potential vorticity to the
 583 right of the propagation direction. The monopole can be considered to be a superposition
 584 of infinite wave modes with different wavelengths, each of which propagates according to
 585 the dispersion relation (25). Due to the dispersive nature of the planetary Rossby wave, the
 586 wave modes with different wavelengths propagate with different phase speeds, resulting in
 587 a distortion of the initial Gaussian profile of the monopole with time (as observed in the
 588 plots of Figure 3).

589 The non-linear advection terms can also be turned on, along with appropriate diffusion
 590 terms to ensure a stable solution over prolonged simulation times. It is worth mentioning
 591 that the inclusion of non-linear and diffusion terms verifies the implementation of every term
 592 in the non-linear homogeneous shallow water equations. While we present the numerical
 593 solution for the linear version of the planetary Rossby wave test case, the non-linear solutions
 594 have also been thoroughly examined. In our convergence analyses, aimed at verifying the
 595 spatial and temporal orders of accuracy, both the linear and non-linear versions of the

596 planetary Rossby wave were solved. As extensive simulation times are not required for
 597 these convergence studies, the activation of diffusion terms is optional for this purpose.

598 **2.8 Test Case 4: Topographic Rossby Wave**

599 The topographic Rossby wave arises because of variations of the bottom topography.
 600 Following the derivation in Cushman-Roisin and Beckers (2011), we only consider a bottom
 601 topography with a small slope of constant magnitude in the meridional direction. If α_0
 602 denotes the bottom slope, the topography is $b(x, y) = -\alpha_0 y$. Using (2), the thickness of the
 603 shallow water layer at any point in time is

$$h(x, y, t) = H + \eta(x, y, t) - b(x, y) = H + \alpha_0 y + \eta(x, y, t). \quad (29)$$

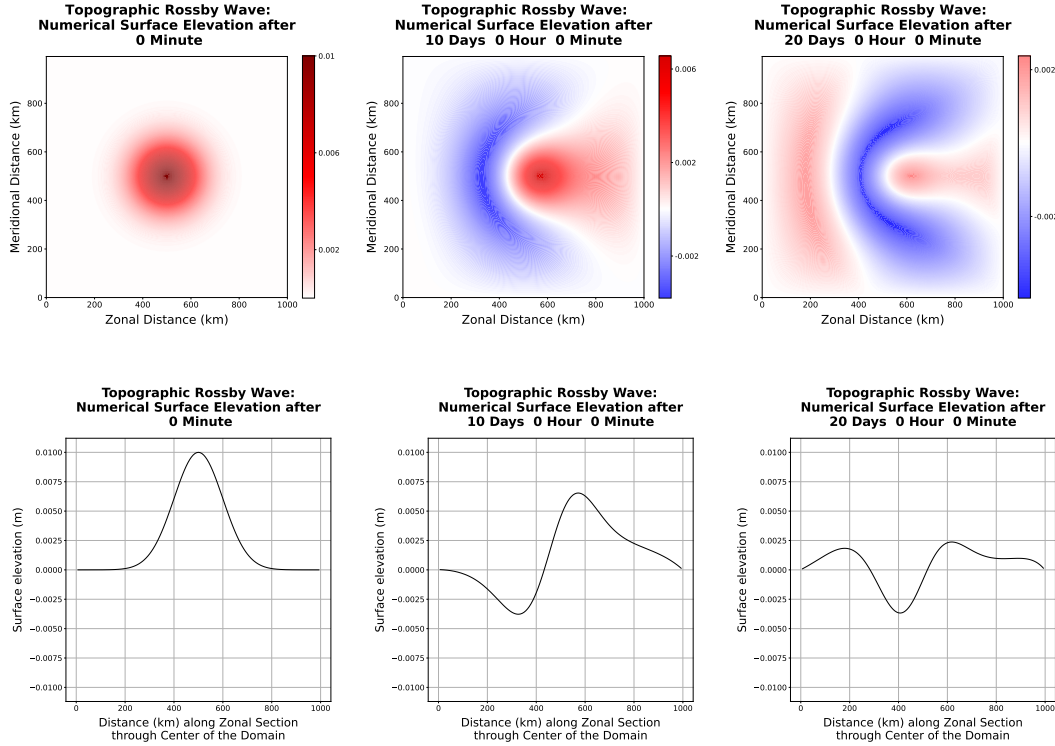


Figure 4. Same as Figure 3, but for TC4, the topographic Rossby wave.

604 The requirement of a gentle bottom slope implies $\alpha = \alpha_0 L/H \ll 1$, where α is a
 605 dimensionless parameter similar to the planetary number, and L is the horizontal length
 606 scale of motion. Just like the planetary Rossby waves, the velocity field of their topographic
 607 analogues consist of a leading-order geostrophic term, and a much smaller ageostrophic
 608 correction term. The ageostrophic terms, driving the motion of these waves, are $\mathcal{O}(\alpha)$
 609 relative to the geostrophic ones, resulting in subinertial wave frequencies $\omega \sim \alpha f \ll f$.

610 Again, assuming the velocities to consist entirely of the geostrophic terms and inserting
 611 them into the momentum equations, we arrive at a first-order approximation of the velocities,
 612 which upon insertion into the continuity equation results in a constant-coefficient equation,
 613 the Fourier series solution of which results in the dispersion relation

$$\omega = \frac{\alpha_0 g k_x}{f \{1 + R^2 (k_x^2 + k_y^2)\}}. \quad (30)$$

614 The zonal and meridional phase speeds, given by $c_x = \omega/k_x$ and $c_y = \omega/k_y$, depend on the
 615 wavenumber, rendering the topographic Rossby waves dispersive. Since c_x has the same sign
 616 as $\alpha_0 f$, in the northern hemisphere (where $f > 0$), the topographic Rossby waves propagate
 617 with the shallower side on their right. Similar to planetary Rossby waves, the potential
 618 vorticity increases towards the right of the direction of the zonal phase propagation.

619 Figure 4 illustrates high-resolution numerical solutions for the topographic Rossby wave,
 620 modeled using DGSEM and RK3. The horizontal domain extents, the spatial and temporal
 621 resolutions, as well as the initial and boundary conditions have been configured to match
 622 their counterparts for the planetary Rossby wave test case (Section 2.7). The bottom slope
 623 is chosen to be $\alpha_0 = \beta_0 H_0 / f_0$, with $\beta_0 = 2 \times 10^{-11} \text{ m}^{-1} \text{ s}^{-1}$, $f_0 = 10^{-4} \text{ s}^{-1}$ and $H_0 = 1000$
 624 m. As a result, the depth increases northward, and the different modes of the dispersive
 625 topographic Rossby wave, each associated with a unique wavenumber, exhibit the same
 626 phase speeds as their planetary analogues, though they travel in the opposite direction, i.e.,
 627 eastward. Due to the variation of phase speed with wavenumber, the initial profile is no
 628 longer maintained, as evidenced by the plots in Figure 4. Just like the planetary Rossby wave
 629 test case, our presentation focuses on the linear solution. However, we have also explored
 630 the non-linear solution, which effectively tests every term in the homogeneous non-linear
 631 shallow water equations. During our convergence studies, we address both variants of the
 632 topographic Rossby wave.

633 2.9 Test Case 5: Barotropic Tide

634 Following the analysis of barotropic tides in Clarke and Battisti (1981) and Clarke
 635 (1991), we consider a simple model of the continental shelf, with constant depth h from the
 636 coast at $x = 0$ to the edge of the shelf at $x = L$, where the depth abruptly increases to H
 637 and remains so in the deep sea. By combining equations (10a), (10b) and (10c), we arrive
 638 at the single equation

$$\nabla^2 \eta_t - \frac{1}{c^2} (\eta_{ttt} + f^2 \eta_t) = 0, \quad (31)$$

639 for modeling sinusoidal barotropic tides with $c^2 = gh$ on the continental shelf and $c^2 = gH$
 640 on the coast. Assuming the continental shelf is long and straight, and applying scaling
 641 analysis and no-normal flow boundary condition at the coast, we arrive at the complete
 642 solution

$$\eta = \hat{\eta} \cos(kx) \cos(\omega t), \quad (32)$$

$$u = \frac{\hat{\eta} g \omega k}{\omega^2 - f_0^2} \sin(kx) \sin(\omega t), \quad (33)$$

$$v = \frac{\hat{\eta} g f_0 k}{\omega^2 - f_0^2} \sin(kx) \cos(\omega t), \quad (34)$$

643 where $\omega = \sqrt{ghk^2 + f_0^2}$. Rewriting (32) as

$$\eta = \frac{1}{2} \hat{\eta} \cos(kx - \omega t) + \frac{1}{2} \hat{\eta} \cos(kx + \omega t), \quad (35)$$

644 we can interpret the surface elevation as the sum of two waves perpendicular to the coast
 645 but travelling in opposite directions. Tidal resonance occurs when the ratio of coastal to
 646 deep sea level is infinite, i.e. when

$$\frac{\eta(0)}{\eta(L)} = \frac{1}{\cos(kL)} = \pm\infty, \quad (36)$$

647 which occurs when

$$L = \left(m + \frac{1}{2}\right) \frac{\pi}{k} = \left(m + \frac{1}{2}\right) \pi \sqrt{\frac{gh}{\omega^2 - f^2}}, \quad (37)$$

648 for a non-negative integer m .

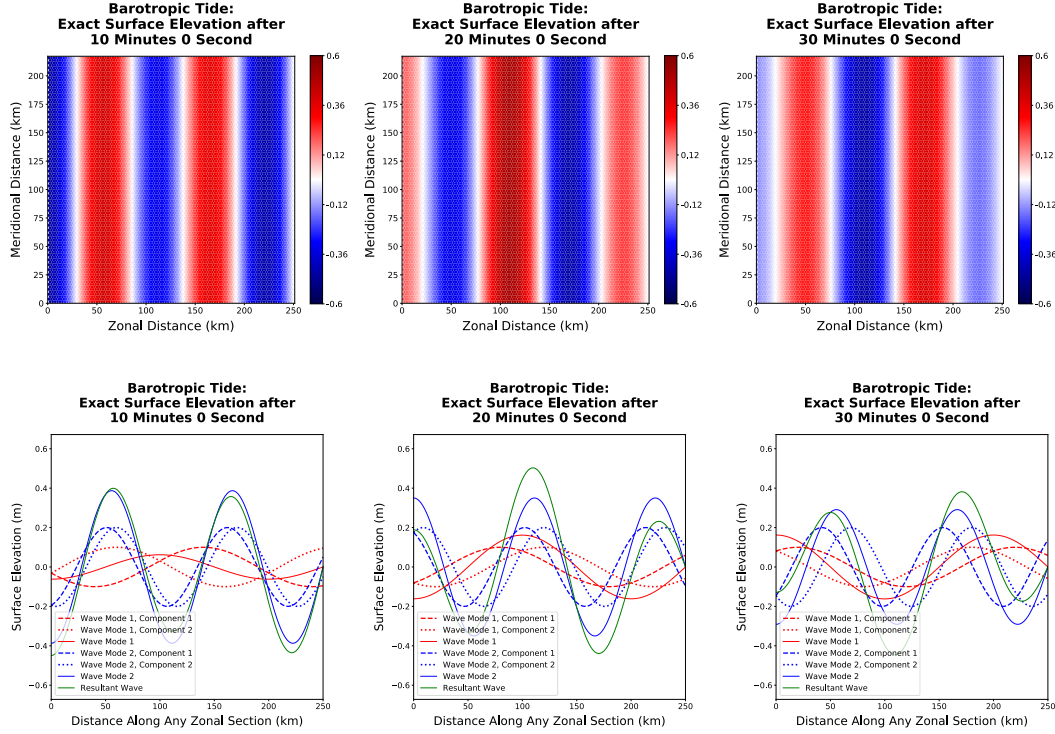


Figure 5. Time evolution of the exact surface elevation of TC5, the barotropic tide, in the entire domain (first row), and along any zonal section (second row).

649 Figure 5 depicts the time evolution of the barotropic tide in the entire domain (first
 650 row) with zonal extent $L_x = 2.5 \times 10^5$ m, and along any zonal section (second row). The
 651 exact surface elevation is chosen to be a superposition of two standing wave modes, each of
 652 which is the sum of two wave modes of equal amplitude and phase speed but traveling in
 653 opposite directions. Each of these component modes is uniform in the meridional direction.
 654 Their wavelengths, $\lambda^{(1)} = 2\pi/k^{(1)}$ and $\lambda^{(2)} = 2\pi/k^{(2)}$, amount to 4/5-th and 4/9-th of the
 655 zonal extents of the domain, which satisfy the conditions for tidal resonance. The surface
 656 elevation amplitudes are designated as $\hat{\eta}^{(1)} = 0.2$ m and $\hat{\eta}^{(2)} = 2\hat{\eta}^{(1)}$. The second row
 657 of Figure 5 shows the resultant barotropic tide as a solid green line, while its underlying
 658 standing wave modes are indicated by solid red and blue lines. The individual components
 659 of each standing wave mode are represented by dashed and dotted lines of the same color.

660 2.10 Test Case 6: Non-linear Manufactured Solution

661 The method of manufactured solutions (MMS) has been applied to a wide variety of
 662 scientific and engineering codes involving the numerical solution of linear and non-linear
 663 PDEs. MMS can be used to generate PDEs with exact solutions so that the order of
 664 accuracy of numerical methods can be investigated. The basic idea of MMS is to choose
 665 such an exact solution, $u = u_e$, and insert it in the left-hand side of the governing PDE
 666 $\mathcal{L}(u) = 0$, where u represents the dependent variable. This gives rise to a source term
 667 $f = \mathcal{L}(u_e)$, which is only a function of space and time, and the coefficients appearing in
 668 the PDE. The modified PDE $\mathcal{L}(u) = f$ is then discretized as $\mathcal{L}_\Delta(u_\Delta) = f_\Delta$, and solved to
 669 obtain the numerical solution u_Δ , where the subscript Δ represents the set of discretization
 670 parameters.

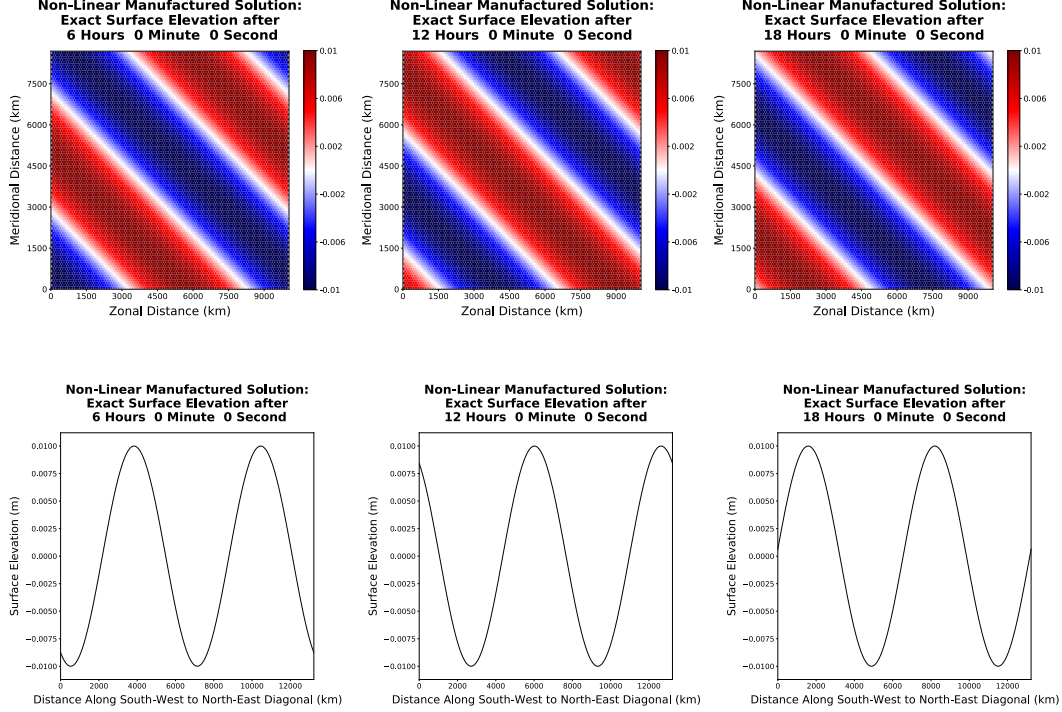


Figure 6. Same as Figure 5, but for TC6, the non-linear manufactured solution, with the second row depicting the time evolution of the exact surface elevation along the south-west to north-east diagonal of the domain.

671 Detailed investigations of MMS against benchmark solutions with sufficiently complex
 672 structure were conducted by Salari and Knupp (2000) and Roache (2002). Within the
 673 geophysical literature, test case (iv) of D. L. Williamson et al. (1992) belongs to the
 674 category of MMS. More recently, Kärnä et al. (2018) presented a steady-state baroclinic
 675 manufactured solution in one vertical and one horizontal dimension. In contrast, we propose
 676 a time-dependent barotropic manufactured solution in the horizontal plane,

$$u = \hat{\eta} \cos(k_x x + k_y y - \omega t), \quad (38a)$$

$$v = 0, \quad (38b)$$

$$\eta = \hat{\eta} \sin(k_x x + k_y y - \omega t), \quad (38c)$$

677 which solves the non-linear rotating inviscid shallow water equations

$$u_t + uu_x + vu_y - fv = -g\eta_x + s^u, \quad (39a)$$

$$v_t + uv_x + vv_y + fu = -g\eta_y + s^v, \quad (39b)$$

$$\eta_t + \{(H + \eta)u\}_x + \{(H + \eta)v\}_y = s^\eta. \quad (39c)$$

678 Inserting the exact solution (38) into the left-hand side of (39), we obtain the source terms

$$s^u = \hat{\eta} \{(-f + gk_x) \cos \phi + \omega \sin \phi - \hat{\eta}(k_x + k_y) \sin(2\phi)/2\}, \quad (40a)$$

$$s^v = \hat{\eta} \{(f + gk_y) \cos \phi + \omega \sin \phi - \hat{\eta}(k_x + k_y) \sin(2\phi)/2\}, \quad (40b)$$

$$s^\eta = \hat{\eta} \{-H(k_x + k_y) \sin \phi - \omega \cos \phi + \hat{\eta}(k_x + k_y) \cos(2\phi)\}, \quad (40c)$$

679 where the phase $\phi = k_x x + k_y y - \omega t$. As expected, the source terms undergo modification if
 680 the governing equations being discretized assume a different form. For instance, if we employ

681 the discontinuous Galerkin Spectral Element Method (DGSEM), outlined in Section 3.2, for
 682 spatial discretization, one option is to start out with the conservative form of the non-linear
 683 rotating shallow water equations. The conservative form can be obtained by adding the
 684 depth-multiplied momentum equations (7a) and (7b) to the continuity equation (7c). The
 685 resulting equations are

$$(hu)_t + (hu^2 + gh^2/2)_x + (huv)_y - fhv = -ghb_x, \quad (41a)$$

$$(hv)_t + (huv)_x + (hv^2 + gh^2/2)_y + fhu = -ghb_y, \quad (41b)$$

$$h_t + (hu)_x + (hv)_y = 0. \quad (41c)$$

686 The source terms transition to

$$\begin{aligned} s^{hu} = & \hat{\eta}H \{ (gk_x - f) \cos \phi + \omega \sin \phi \} \\ & + \hat{\eta}^2 [\sin(2\phi) \{ -H(k_x + k_y) + (gk_x - f)/2 \} - \omega \cos(2\phi)] \\ & + \hat{\eta}^3 (k_x + k_y) \{ -\sin(2\phi) \sin \phi + \cos^3 \phi \}, \end{aligned} \quad (42a)$$

$$\begin{aligned} s^{hv} = & \hat{\eta}H \{ (gk_y + f) \cos \phi + \omega \sin \phi \} \\ & + \hat{\eta}^2 [\sin(2\phi) \{ -H(k_x + k_y) + (gk_y + f)/2 \} - \omega \cos(2\phi)] \\ & + \hat{\eta}^3 (k_x + k_y) \{ -\sin(2\phi) \sin \phi + \cos^3 \phi \}, \end{aligned} \quad (42b)$$

$$s^h = \hat{\eta} \{ -H(k_x + k_y) \sin \phi - \omega \cos \phi + \hat{\eta}(k_x + k_y) \cos(2\phi) \}, \quad (42c)$$

687 where the water depth is simplified to $h(x, y, t) = H + \eta(x, y)$, and the right-hand side of
 688 (41a) and (41b) is reduced to zero due to the presence of a flat bottom ($b = 0$). Figure 6
 689 depicts the time evolution of the manufactured solution across the entire domain (first row)
 690 and along the south-west to north-east diagonal (second row). The relevant parameters are
 691 $L_x = 10^7$ m and $\hat{\eta} = 0.01$ m. The wavenumbers are defined by $k_x = 2\pi/L_x$ and $k_y = 2\pi/L_y$.
 692 The angular frequency is $\omega = c\sqrt{k_x^2 + k_y^2}$, with $c = \sqrt{gH} = 100$ m s⁻¹ representing the speed
 693 of shallow water gravity waves.

694 While we have utilized (38) to ‘manufacture’ our solution for this non-linear test case,
 695 any smooth solution in space and time can serve the purpose, provided that the source
 696 terms are accurately defined. For instance, the exact solutions of the coastal Kelvin wave,
 697 inertia-gravity wave, and the barotropic tide, which solve the linearized homogeneous form
 698 of (39), can be employed to ‘manufacture’ our solution and verify the implementation of
 699 non-linear terms. In these cases, the source terms are essentially the non-linear terms of (39)
 700 computed with the exact solutions, and can be expressed as:

$$s^u = [uu_x + vu_y]_{\text{exact}}, \quad (43a)$$

$$s^v = [uv_x + vv_y]_{\text{exact}}, \quad (43b)$$

$$s^\eta = [(\eta u)_x + (\eta v)_y]_{\text{exact}}. \quad (43c)$$

701 3 Spatial and Temporal Discretizations

702 To generate the numerical solutions, we have developed a rotating shallow water solver
 703 in an object-oriented Python environment (Bishnu, 2024a). This tool employs two forms of
 704 spatial discretizations: first, a mimetic finite volume method based on the TRiSK framework
 705 (Thuburn et al., 2009; T. D. Ringler et al., 2010), and second, a high-order discontinuous
 706 Galerkin spectral element method (DGSEM). The primary motivation for selecting these two
 707 spatial discretization methods originates from their widespread application in operational
 708 ocean models. These models generally adopt

- 709 (a) finite volume methods (LeVeque, 2002; Eymard et al., 2003; Versteeg & Malalasekera,
 710 2007; Patankar, 2018); or
- 711 (b) finite element (Zienkiewicz et al., 2005; Bathe, 2006; Hughes, 2012; D. L. Logan, 2022)
 712 or spectral element (Patera, 1984; Maday & Patera, 1989; Karniadakis & Sherwin,
 713 2005; D. A. Kopriva, 2009) methods.

714 Finite volume methods (FVMs) serve as a highly efficient method for solving PDEs.
 715 By partitioning the computational domain into a finite set of control volumes, FVMs
 716 approximate the integral form of the governing equations over these volumes. This method’s
 717 distinct advantage lies in its conservation of quantities of interest, making it a preferred
 718 choice for problems bound by conservation laws, typical in fields such as fluid dynamics and
 719 heat transfer. Many ocean models like Oceananigans (Ramadhan et al., 2020), MITgcm
 720 (Marshall et al., 1997), MOM (Griffies et al., 2005), ROMS (Shchepetkin & McWilliams,
 721 2005), NEMO (Madec et al., 2023), FVCOM (C. Chen et al., 2006), and MPAS-Ocean
 722 (T. Ringler et al., 2013) utilize FVMs for spatial discretization.

723 The finite element method (FEM), on the other hand, offers a versatile solution to tackle
 724 complex problems, often formulated as PDEs in engineering and mathematical physics.
 725 The computational domain, divided into a mesh of simpler elements (like 2D triangles
 726 or 3D tetrahedra), forms the foundation of FEM. The methodology hinges on computing
 727 approximate solutions at the element nodes, thereby minimizing an associated error function.
 728 This results in highly accurate solutions within the approximations’ constraints, making
 729 FEM particularly useful for problems involving structural analysis, heat transfer, fluid flow,
 730 mass transport, and electromagnetic fields.

731 A specialized class of the FEMs is the spectral element method (SEM), discussed in
 732 detail in Section 3.2. In contrast to the classical FEMs that predominantly use low, fixed
 733 order polynomials (typically linear or quadratic) as basis functions, SEMs leverage the
 734 flexibility of adjustable polynomial order, enabling exponential convergence rates in smooth
 735 problems. SEMs, typically using quadrilateral (2D) or hexahedral (3D) elements, are adept
 736 at managing complex geometries. The numerical solution derived using SEM parallels those
 737 produced by FEM, facilitating comparable methods for conducting convergence studies and
 738 interpreting the resulting plots. This is especially true if the underpinning method is a
 739 discontinuous Galerkin (DG) method (Hesthaven & Warburton, 2007). The DG method
 740 allows for the solution to be discontinuous between elements, thereby making it particularly
 741 effective for problems characterized by sharp gradients or shocks, as encountered in fluid
 742 dynamics or electromagnetism. Software based on SEM showcases excellent compatibility
 743 with GPU-accelerated hardware, a technology that is now dominant in the world’s fastest
 744 supercomputers (Strohmaier & Dongarra, 2023). Therefore, we anticipate a surge in the
 745 development of high-order methods like SEMs in research software in the years to come.
 746 Currently, among functional ocean models, FESOM (Danilov et al., 2004; Q. Wang et al.,
 747 2014) and NUMO (Kopera et al., 2018, 2023) employ FEM and SEM respectively for spatial
 748 discretization.

749 We discuss in subsequent sections a few key considerations depending on the spatial
 750 discretization technique in use. For instance, in Section 6, we explore the significance of
 751 conducting self-refinement convergence tests only in space and only in time, the underlying
 752 reasons for which may vary between FVMs and SEMs. Moreover, we delve into numerical
 753 implementation details in Appendix C, some of which are pertinent to FVMs and some
 754 to SEMs. Regardless of these disparities, we demonstrate the robustness of our numerical
 755 recipe in verifying the spatial and temporal orders of accuracy across both types of spatial
 756 discretization.

757 We now provide a brief description of the TRiSK-based FVM and DGSEM used in our
 758 numerical experiments.

759 3.1 TRiSK-Based Mimetic Finite Volume Method

760 The mimetic finite volume spatial discretization based on the TRiSK scheme was first
 761 proposed by Thuburn et al. (2009) to ensure that geostrophic modes remain stationary and
 762 Coriolis terms remain energy conserving on arbitrarily structured C-grids. It was then
 763 generalized by T. D. Ringler et al. (2010) to model the non-linear rotating shallow water
 764 equations while guaranteeing the evolution of mass, velocity, and potential vorticity in a

765 consistent and compatible manner, and the conservation of total energy within the time
 766 truncation error. This mimetic finite volume method was chosen to horizontally discretize
 767 the primitive equations of MPAS-Ocean while invoking the hydrostatic, incompressible,
 768 and Boussinesq approximations on a staggered C-grid. Even though the grid cells of
 769 MPAS-Ocean are near hexagons consisting of five or more sides, the MPAS framework
 770 supports cells with any number of sides with the algorithm and code remaining identical for
 771 cells of all shapes and sizes. Since this horizontal discretization guarantees conservation of
 772 mass, potential vorticity, and energy, it makes MPAS-Ocean a suitable candidate to simulate
 773 mesoscale eddies.

774 The spatial domain is assumed to be tessellated by two meshes, a primal mesh and a
 775 dual mesh. Each corner of a primary mesh cell is uniquely associated with a center of a dual
 776 mesh cell and vice versa. For a regular hexagonal mesh, each corner of a primary mesh cell
 777 coincides with a vertex of a dual mesh cell and vice versa. A line segment connecting two
 778 primal mesh cell centers is uniquely associated with a line segment connecting two dual mesh
 779 cell centers. In case of a regular hexagonal mesh, these two line segments are perpendicular
 780 bisectors of each other. In case of an irregular hexagonal mesh, these two line segments can
 781 still intersect orthogonally, but not necessarily at their midpoints. As mentioned before, the
 782 two prognostic variables for the rotating shallow water equations are the surface elevation,
 783 η , defined at the primal cell centers, and the normal velocity \mathbf{u}_e defined at the primal cell
 784 edges. The divergence of a two-dimensional vector quantity is defined at the position of
 785 η , while the two-dimensional gradient of a scalar quantity is defined at the position of \mathbf{u}_e
 786 and oriented along its direction. The curl of a vector quantity is defined at the vertices of
 787 the primal cells. Finally, the tangential velocity \mathbf{u}_e^\perp along a primal cell edge is computed
 788 diagnostically using a flux mapping operator from primal to dual mesh, which essentially
 789 takes a weighted average of the normal velocities on the edges of the cells sharing that edge.
 790 Interested readers may refer to Thuburn et al. (2009) and T. D. Ringler et al. (2010) for an
 791 extensive discussion on the mesh specifications, the elements of the discrete system along
 792 with their positioning and their connectivities, and the formulation of the discrete spatial
 793 and flux-mapping operators.

794 3.2 Discontinuous Galerkin Spectral Element Method

795 Spectral element methods belong to the category of multidomain spectral methods.
 796 In spectral element methods, the physical domain is divided into smaller, non-overlapping
 797 elements, as illustrated in Figure 7. Within each element, functions are approximated by
 798 Lagrange interpolating polynomials. The interpolation knots are Gauss-type Quadrature,
 799 often Legendre-Gauss or Legendre-Gauss-Lobatto (D. A. Kopriva, 2009; D. Kopriva &
 800 Gassner, 2010; Gassner et al., 2016). Each element is mapped to a reference element,
 801 and the mapping and metric terms are also approximated by Lagrange interpolation.

802 With Discontinuous Galerkin Spectral Element Methods, the weak form of the equations
 803 are solved within each element. As explained in standard finite and spectral element
 804 textbooks like Donea and Huerta (2003), Hughes (2012), Zienkiewicz et al. (2005), Bathe
 805 (2006), Reddy (2019), D. L. Logan (2022), Karniadakis and Sherwin (2005), Canuto et al.
 806 (2007b), and D. A. Kopriva (2009), the weak form is obtained by multiplying the original
 807 “strong form” of the PDE by a test function and then integrating over the domain. In this
 808 context, a test function is a mathematical tool that facilitates the derivation of the weak
 809 form of the PDE. This weak form requires the solution to be differentiable to a lower order
 810 compared to the strong form, and is generally easier to solve numerically. The test function
 811 is chosen to have certain properties, such as being zero on the boundaries of the domain
 812 or being part of a certain function space. Integration by parts is subsequently applied to
 813 the product of the PDE and the test function to reduce the order of the derivatives. This
 814 process transitions the problem into an integral representation wherein the solution satisfies
 815 the PDE in an averaged “weak” sense rather than at every single point, as mandated by
 816 the strong form. In case of DGSEM, the test functions are specified as each of the Lagrange

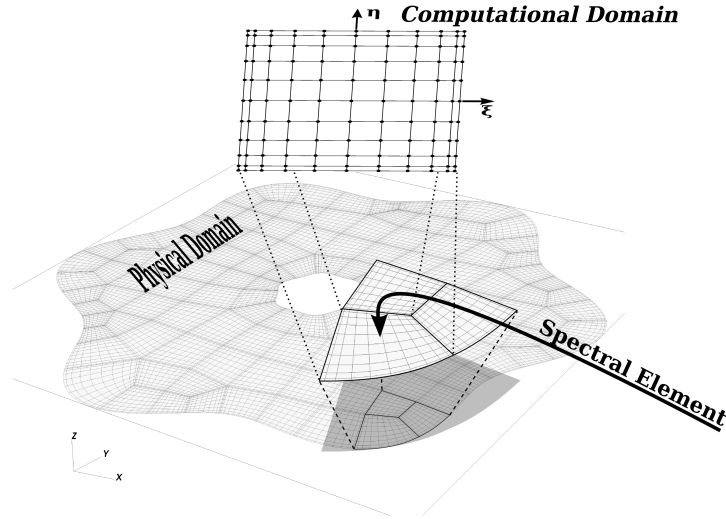


Figure 7. Depiction of a physical domain divided into elements that are then each mapped to a reference computational element. Within each element, solution variables and the coordinate mapping are approximated by Lagrange interpolating polynomials.

817 interpolating polynomials. Additionally, continuous integrals in the weak formulation are
 818 replaced by discrete quadrature. For computational efficiency, the quadrature points are
 819 chosen to match the interpolation points which also provides spectral accuracy. To couple
 820 neighboring elements, approximate Riemann solvers are used to exchange properties, such
 821 as mass and momentum. For hyperbolic systems, like the shallow water equations, the
 822 Riemann solver is chosen to be consistent with the underlying equations while also providing
 823 dissipation to stabilize the numerical method (Gassner et al., 2016; Ranocha, 2016). To
 824 exchange momentum and mass fluxes between neighboring elements and approximate the
 825 numerical flux at the element boundaries, we employ the upwind local Lax-Friedrichs Riemann
 826 solver of Rusanov (1961).

827 DGSEM allows for spatial refinement through two distinct approaches: increasing the
 828 polynomial order while keeping the number of elements constant, known as p -refinement, or
 829 alternatively, increasing the number of elements with a constant polynomial order, termed
 830 h -refinement. In Section 6.2, the leading order error terms of DGSEM are employed to
 831 illustrate how p -refinement achieves exponential convergence, while h -refinement effectively
 832 captures the spatial order of accuracy.

833 For the linear test cases, the weak form of the linear constant- or variable-coefficient
 834 shallow water equations (9c) is solved in Cartesian coordinates. However, for non-linear test
 835 cases, including the manufactured solution, and the non-linear planetary and topographic
 836 Rossby waves, we start with the conservative form (41) of the non-linear shallow water
 837 equations (7), and then solve the weak form of these equations.

838 3.3 Time-Stepping Methods

839 We advance the numerical solution using the following set of time-stepping methods:

840 **List 1.** *Standard predictor-corrector and multistep time-stepping methods*

841 RK2: explicit midpoint method, belonging to the second-order Runge-Kutta family

842 RK3: low-storage third-order Runge-Kutta method of J. Williamson (1980)

843 RK4: low-storage fourth-order Runge-Kutta method of Carpenter and Kennedy (1994)

844 AB2: second-order Adams-Bashforth method
 845 AB3: third-order Adams-Bashforth method
 846 AB4: fourth-order Adams-Bashforth method

847 **List 2.** *Time-stepping methods popular in ocean modeling*

848 FB: forward-backward or Implicit Euler method
 849 LF_TR: leapfrog trapezoidal method
 850 LF_AM3: leapfrog Adams-Moulton method
 851 FB_RK2: forward-backward method with RK2 feedback
 852 GenFB_AB2-AM3: generalized forward-backward method with AB2-AM3 step
 853 GenFB_AB3-AM4: generalized forward-backward method with AB3-AM4 step

854 Shchepetkin and McWilliams (2005) perform a detailed stability analysis of each of the
 855 time-stepping methods of List 2. The parameters of all of these methods can be optimized to
 856 attain a specific order of accuracy, maximize the stability range, and minimize the magnitude
 857 of the local truncation error. By considering all variations of these parameters discussed in
 858 Shchepetkin and McWilliams (2005), the total number of time-stepping methods of List 2
 859 exceeds 20. Even though we have tested the numerical solution against all of these methods,
 860 we present the convergence plots for only the methods of List 1.

861 **4 A Primer on Truncation Error and Order of Accuracy**

862 We furnish the necessary background on truncation error and how it is related to the
 863 numerical solution's spatial and temporal orders of accuracy. We consider situations where
 864 the orders of accuracy of the local truncation error and the global error agree, as encountered
 865 in a wide variety of computational physics domains including atmosphere and ocean models.

866 When solving PDEs, especially in the context of physics and engineering, it is often
 867 impossible or highly impractical to obtain an analytical solution. Instead, numerical methods
 868 are employed, and this involves discretizing the domain of the problem, i.e., breaking it down
 869 into small discrete segments or elements. The process of discretization inherently introduces
 870 approximations, primarily due to the omission of higher-order derivative terms, culminating
 871 in truncation errors. For time-dependent PDEs that model transient phenomena, like the
 872 unsteady heat conduction or fluid flow, both spatial and temporal discretizations are used,
 873 resulting in truncation errors associated with both space and time approximations. As
 874 the simulation progresses, these errors accumulate, leading to an increasingly pronounced
 875 divergence between the numerical and exact solutions.

876 The order of accuracy of the truncation error corresponds to the rate at which this error
 877 diminishes relative to the size of the discretization. A higher order signifies a more rapid
 878 shrinkage of error with finer discretization. For example, a second-order accurate method
 879 in space anticipates an error reduction by n^2 for every refinement of the spatial grid by a
 880 factor of n .

881 Truncation errors play a pivotal role in determining the accuracy of a numerical solution.
 882 Striking the right balance is essential: one must pick a method or grid resolution that offers
 883 adequate accuracy without overburdening computational resources. While refining the grid
 884 often curtails truncation errors, it simultaneously escalates the computational demands and
 885 may exacerbate other anomalies, such as round-off errors. In the world of numerical PDE
 886 solutions, a deep comprehension of truncation errors, their origins, and their ramifications
 887 is indispensable. This knowledge guides the choice of optimal methods, grid scales, and
 888 bolsters confidence in the accuracy of derived solutions.

4.1 Truncation Error, Consistency, Stability, and Convergence

The local truncation error, τ , is the residual after substituting the exact solution into the difference equation, obtained by discretizing the original differential equation. For time-marching or initial value problems involving ordinary differential equations (ODEs), hyperbolic and parabolic PDEs, some textbooks define the local truncation error as the error incurred in a single time step Δt starting with the exact solution at the beginning of the time step. If $\hat{\tau}$ represents the local truncation error based on this definition, it is straightforward to demonstrate that $\tau = \hat{\tau}/\Delta t$ (Bishnu, 2021).

A numerical method is called consistent if the local truncation error, τ , over a single time step, reduces to zero with the refinement of the spatial and temporal grids, sometimes under additional constraints. Mathematically,

$$\lim_{\Delta \rightarrow 0} \tau = \lim_{\Delta \rightarrow 0} \frac{\hat{\tau}}{\Delta t} = 0, \quad (44)$$

where Δ represents the set of discretization parameters for the spatial and temporal grids.

Numerical stability in the context of solving time-marching ODEs and PDEs involves analyzing how various types of errors—those from initial conditions, boundary conditions, round-off errors, and notably discretization or truncation errors—propagate in space and time as the numerical method is employed. In the realm of ODEs, the stability of a method largely depends on the chosen time step size, with the objective being to prevent errors from growing exponentially or becoming unbounded as time progresses. This concept extends to PDEs as well, but with an added layer of complexity. Here, stability is influenced not just by the time step size, but also by its relationship with spatial step sizes. This relationship is often scrutinized using the Courant-Friedrichs-Lewy (CFL) condition, a crucial criterion in the stability analysis of numerical methods for hyperbolic PDEs. The Von Neumann stability analysis emerges as another pivotal technique, particularly adept at determining the stability of numerical schemes applied to linear PDEs. By assessing the growth of Fourier modes in the numerical solution, this method provides a deeper understanding of how errors might amplify over iterations. The stability of a numerical method is crucial to ensure that the computed solution remains reliable and bounded over time. An unstable method can lead to solutions that diverge dramatically from the exact solution, even if the method is consistent, rendering the numerical approach ineffective for practical applications.

The numerical solution is said to converge to the exact solution if the global truncation error, or simply the global error, $\hat{\tau}_G$, defined as the difference between the exact and numerical solutions at a time horizon, reduces to zero with the refinement of the spatial and temporal grids. If the time horizon is specified as $T = n\Delta t$, $\hat{\tau}_G$ encapsulates the cumulative effect of $\hat{\tau}$ over n time steps. For a broad spectrum of numerically stable methods, barring exceptions like superconvergent and subconvergent ones (Levine, 1985; Ferreira & Grigorieff, 1998; Barbeiro et al., 2005), $\hat{\tau}_G$ is typically one order of Δt smaller than $\hat{\tau}$ and of the same order of accuracy as τ . So, if (44) holds for a stable numerical scheme, it is indicative of convergence. This concept aligns with the first half of the Lax Equivalence Theorem (Lax & Richtmyer, 1956), asserting that a consistent finite difference method for a linear initial value problem converges if and only if it is stable. For numerical methods such as finite volume, finite and spectral element methods, the Lax Equivalence Theorem does not directly apply in its classical form, as these methods have different formulations compared to finite difference methods. However, the underlying principles of consistency, stability, and convergence are still crucial in these methods.

4.2 Truncation Error of Hyperbolic and Parabolic PDEs

In Bishnu (2021), we determined the full expression for the local truncation error of numerical solutions of hyperbolic and parabolic PDEs advanced with Method of Lines time integrators. These integrators are characterized by their separate treatment of space and

937 time discretizations: they initially discretize the spatial variables to reduce the PDE to
 938 a system of ODEs, which are then solved using standard ODE integration techniques.
 939 By employing theoretical analysis and symbolic algebra computations, we obtained exact
 940 expressions for the coefficients of the generic local truncation error

$$\tau = \mathcal{O}(\Delta x^\alpha) + \Delta t \mathcal{O}(\Delta x^\alpha) + \Delta t^2 \mathcal{O}(\Delta x^\alpha) + \dots + \Delta t^{\beta-1} \mathcal{O}(\Delta x^\alpha) + \mathcal{O}(\Delta t^\beta), \quad (45)$$

941 where Δx and Δt denote the cell width and time step size, and α and β represent the
 942 spatial and temporal orders of accuracy. The right-hand side of (45) is applicable not
 943 only to the numerical solution of hyperbolic and parabolic PDEs in one spatial dimension,
 944 but also extends to higher-dimensional cases, provided a uniform grid is employed. This
 945 is exemplified in Section 6.2, where, in the context of a two-dimensional hexagonal mesh,
 946 the two primary grid scales are identified: the distance Δx between adjacent cell centers,
 947 and the side length Δy of a hexagonal cell. In a uniform hexagonal mesh, Δx and Δy
 948 remain constant, and exhibit a proportional relationship, which paves the way for the local
 949 truncation error to assume the form (45).

950 The derivation of (45) is replete with mathematical complexities. While we forgo
 951 a detailed breakdown here, interested readers can refer to Bishnu (2021) which provides
 952 thorough explanations and numerous illustrative examples. Nevertheless, we will touch
 953 upon the core rationale behind this specific form of the local truncation error. Delving
 954 into the steps of any Method of Lines time integrator, we note that time derivatives or
 955 tendency terms are evaluated either at fractional time steps in the case of predictor-corrector
 956 methods or at prior time levels for multistep methods. For an ODE (or a PDE with no
 957 spatial discretization error), these tendencies are exact. However, for a general PDE, these
 958 tendencies accrue spatial discretization errors of $\mathcal{O}(\Delta x^\alpha)$, which manifest as coefficients of
 959 the various powers of Δt .

960 The coefficients of Δx^α in the terms $\Delta t \mathcal{O}(\Delta x^\alpha)$, $\Delta t^2 \mathcal{O}(\Delta x^\alpha)$, \dots , $\Delta t^{\beta-1} \mathcal{O}(\Delta x^\alpha)$ of
 961 (45) contain higher order spatial derivatives of the solution, coefficients of the PDE and
 962 source terms (Bishnu, 2021). Consequently, the terms $\Delta t^k \mathcal{O}(\Delta x^\alpha)$ for $k = 1, 2, \dots, \beta - 1$
 963 are typically much smaller in magnitude compared to the first and last terms of (45),
 964 assuming forms $\mathcal{O}(\Delta x^\alpha)$ and $\mathcal{O}(\Delta t^\beta)$, and representing the leading-order spatial and
 965 temporal discretization errors. This disparity enables us to succinctly approximate (45)
 966 as

$$\tau = \mathcal{O}(\Delta x^\alpha) + \mathcal{O}(\Delta t^\beta). \quad (46)$$

967 It is worth emphasizing that (45) and (46) hold true for a broad spectrum of hyperbolic
 968 or parabolic PDEs, irrespective of whether they are linear or non-linear. This applicability
 969 spans various spatial discretizations and time-stepping techniques within the Method of
 970 Lines framework. To bring these theoretical assertions to life, we undertook convergence
 971 studies on both linear and non-linear advection equations, as well as diffusion equations,
 972 detailed in Bishnu (2021). These studies employed finite difference and finite volume spatial
 973 discretizations, coupled with predictor-corrector and multistep time-stepping methods. In
 974 the present paper, we solidify our findings, showcasing convergence plots for linear and
 975 non-linear shallow water test cases using the TRiSK-based mimetic finite volume and
 976 high-order discontinuous Galerkin spectral element methods.

977 4.3 Convergence at Constant Ratio of Time Step to Cell Width

978 Assume that our numerical scheme is stable, and the global error, $\hat{\tau}_G$, is of the same
 979 order of accuracy as the local truncation error, τ , conforming to the form (46). Then a
 980 simultaneous refinement in space and time, maintaining a constant ratio of $\gamma = \Delta t/\Delta x$,
 981 simplifies the global error to

$$\hat{\tau}_G = \mathcal{O}(\Delta x^\alpha) + \mathcal{O}(\gamma^\beta \Delta x^\beta) = \mathcal{O}(\Delta x^\alpha) + \mathcal{O}(\Delta x^\beta) \approx \mathcal{O}(\Delta x^{\min(\alpha, \beta)}), \quad (47)$$

982 in the asymptotic regime, where the error is dominated by the larger of Δx^α and Δt^β , rather
 983 than their coefficients. Given a spatial discretization of order α , the asymptotic convergence
 984 rate clearly cannot exceed α . To attain this convergence rate, we need a time-stepping
 985 method of order β such that $\beta \geq \alpha$. For optimal computational efficiency within a given
 986 family of time-stepping methods, the preferred choice would be $\beta = \alpha$.

987 4.4 Refinement Only in Space or Only in Time

988 If refinement is performed only in space while employing a stable numerical scheme,
 989 convergence of the global error cannot be guaranteed due to the presence of the $\mathcal{O}(\Delta t^\beta)$
 990 term. A similar situation arises with refinement only in time, where the $\mathcal{O}(\Delta x^\alpha)$ term acts
 991 as an impediment to the convergence of the global error. In other words, under only spatial
 992 or temporal refinement, the local truncation error does not necessarily reduce to zero. As
 993 a result, our numerical solution may not even be consistent. In such situations, in light of
 994 the Lax Equivalence Theorem (Lax & Richtmyer, 1956), convergence becomes impossible.

995 4.5 Verification of the Spatial or Temporal Order of Accuracy

996 While asymptotic convergence may not be achievable with only spatial or temporal
 997 refinement, we can still verify the spatial and temporal orders of accuracy. For refinement
 998 only in space at constant Δt , the global error at a specific time horizon and a spatial location
 999 x_j can be expressed as

$$(\hat{\tau}_G)_j = \mathcal{O}(\Delta x^\alpha) + \mathcal{O}(\Delta t^\beta) = \zeta \Delta x^\alpha + \zeta_{\beta+1} \Delta t^\beta, \quad (48)$$

1000 where the coefficients ζ and $\zeta_{\beta+1}$ are independent of Δx . If $\zeta \Delta x^\alpha \gg \zeta_{\beta+1} \Delta t^\beta$, we can
 1001 calculate the spatial order of convergence by refining Δx with Δt held constant. For a
 1002 general setting, however, we need to use an alternate method. This is achieved by comparing
 1003 two uniform meshes with cell widths Δx_i and Δx_{i+1} , with $\Delta x_{i+1} < \Delta x_i$. Then we can write

$$(\hat{\tau}_{G_i^x})_j \approx \zeta \Delta x_i^\alpha + \zeta_{\beta+1} \Delta t^\beta, \quad (49a)$$

$$(\hat{\tau}_{G_{i+1}^x})_j \approx \zeta \Delta x_{i+1}^\alpha + \zeta_{\beta+1} \Delta t^\beta. \quad (49b)$$

1004 Assuming $(\hat{\tau}_{G_{i+1}^x})_j < (\hat{\tau}_{G_i^x})_j$, we define

$$\begin{aligned} (\Delta \hat{\tau}_{G_{i,i+1}^x})_j &\equiv (\hat{\tau}_{G_i^x})_j - (\hat{\tau}_{G_{i+1}^x})_j = \zeta (\Delta x_i^\alpha - \Delta x_{i+1}^\alpha) \\ &= \zeta \Delta x_{i+1}^\alpha \left\{ \left(\frac{\Delta x_i}{\Delta x_{i+1}} \right)^\alpha - 1 \right\} > 0. \end{aligned} \quad (50)$$

1005 Defining $p = \Delta x_{i+1}/\Delta x_i < 1$ to be the ratio between the two mesh sizes, we can write

$$(\Delta \hat{\tau}_{G_{i,i+1}^x})_j = \zeta \Delta x_{i+1}^\alpha (p^{-\alpha} - 1). \quad (51)$$

1006 Upon taking the logarithm of both sides, we obtain

$$\log \left((\Delta \hat{\tau}_{G_{i,i+1}^x})_j \right) = \theta + \alpha \log (\Delta x_{i+1}), \quad (52)$$

1007 where $\theta = \log \{ \zeta (p^{-\alpha} - 1) \}$ is constant. To compute the spatial order of accuracy, we first
 1008 choose a sequence of M grids with $\Delta x_{i+1}/\Delta x_i = p$ for $i = 1, 2, \dots, M-1$, and all satisfying
 1009 a CFL condition. After interpolating the error to the coarsest mesh with spacing Δx_1 , we
 1010 plot the norm of the difference between successive global errors $(\Delta \hat{\tau}_{G_{i,i+1}^x})_{\text{norm}}$ against the
 1011 cell width Δx_{i+1} on a log-log scale, for $i = 1, 2, \dots, M-1$. The slope of the best-fit line
 1012 gives us the spatial order of accuracy.

1013 Proceeding in a similar fashion, we can ascertain the temporal order of accuracy.
 1014 Specifically, we refine the time step while preserving the spatial resolution and plot the
 1015 norm of the difference between successive global errors. Since the spatial resolution remains
 1016 unchanged, there is no need for the interpolation step.

1017 It is worth noting that the exact solution is independent of both the spatial resolution
 1018 and the time step. So, for refinement only in time, if u_j^{n+1} represents the solutions at time
 1019 level t^{n+1} , and $(\hat{u}_i)_j^{n+1}$ represents its numerical counterpart obtained with time step Δt_i ,
 1020 we can write

$$\begin{aligned} \left(\Delta \hat{\tau}_{G_{i,i+1}^t}\right)_j^{n+1} &\equiv \left(\hat{\tau}_{G_i^t}\right)_j^{n+1} - \left(\hat{\tau}_{G_{i+1}^t}\right)_j^{n+1} = \left\{u_j^{n+1} - (\hat{u}_i)_j^{n+1}\right\} - \left\{u_j^{n+1} - (\hat{u}_{i+1})_j^{n+1}\right\} \\ &= (\hat{u}_{i+1})_j^{n+1} - (\hat{u}_i)_j^{n+1} \equiv (\Delta \hat{u}_{i,i+1})_j^{n+1}. \end{aligned} \quad (53)$$

1021 Therefore, if we calculate the difference $(\Delta \hat{u}_{i,i+1})_j^{n+1}$ between numerical solutions $(\hat{u}_i)_j^{n+1}$
 1022 and $(\hat{u}_{i+1})_j^{n+1}$ obtained with time steps Δt_i and Δt_{i+1} for $i = 1, 2, \dots, M-1$, at every mesh
 1023 point x_j and time level t^{n+1} , and then compute its norm $(\Delta \hat{u}_{i,i+1})_{\text{norm}}^{n+1}$ and plot it against
 1024 Δt_{i+1} , we can achieve convergence at a rate matching the temporal order of accuracy. In the
 1025 event of performing only a spatial refinement, it is necessary to first interpolate the numerical
 1026 solution to the coarsest mesh. Subsequently, the same steps can be followed to achieve
 1027 convergence aligned with the spatial order of accuracy. This methodology offers a practical
 1028 advantage by eliminating the need to engage with exact or manufactured solutions, thereby
 1029 streamlining the process and enhancing its applicability. In our own numerical experiments,
 1030 we adopt this approach for verifying the spatial and temporal orders of accuracy for the
 1031 planetary and topographic Rossby wave test cases, which are not equipped with exact
 1032 solutions.

1033 One should recognize that these unconventional convergence exercises primarily aim
 1034 to verify the correct implementation of the spatial and temporal discretizations. The error
 1035 norm of the numerical solution under only spatial or temporal refinement is not expected to
 1036 converge in the asymptotic regime. It is only when the time step and the cell width undergo
 1037 simultaneous refinement, while maintaining their ratio, that we can expect convergence of
 1038 the global error norm.

1039 4.6 Beyond Method of Lines Time Integrators

1040 We reiterate that the full expression (45) for the local truncation error was specifically
 1041 derived for Method of Lines time integrators in Bishnu (2021). This formulation does
 1042 not universally apply to time integrators that concurrently handle spatial and temporal
 1043 discretizations, and are applicable exclusively to PDEs. Notable exceptions, such as the
 1044 Lax-Wendroff method, do exist. Nevertheless, if the specific form of the local truncation
 1045 error is known beforehand, the principles, methodologies, and anticipated outcomes for
 1046 performing space-time, space-only, or time-only convergence studies, as discussed in Sections
 1047 4.3 to 4.5, may be extended to time integrators beyond Method of Lines, with appropriate
 1048 adjustments.

1049 5 Numerical Dispersion, Numerical Dissipation, and Spurious Oscillations

1050 Numerical dispersion and numerical dissipation are intrinsic challenges that arise when
 1051 approximating PDEs using numerical methods. These phenomena are particularly impactful
 1052 in wave-propagation problems, with dispersion errors influencing the propagation speed of
 1053 disturbances and dissipation errors impacting the strength.

1054 Numerical dispersion commonly manifest in conservation laws when the dominant
 1055 truncation error stems from odd-order derivatives, causing a misrepresentation of the wave's
 1056 phase speed. Dispersion errors are observed not only in finite difference and finite volume

1057 methods, but also in high-order methods like single- and multi-domain SEMs. It is crucial
 1058 to underscore that even though high-order methods like DGSEM boast increased accuracy,
 1059 they are not immune to dispersion, especially at element boundaries with discontinuous
 1060 solutions. Here, the choice of basis functions and the employed Riemann solver play pivotal
 1061 roles. Even with high-order polynomial approximations, phase errors may arise as waves
 1062 cross multiple elements.

1063 Numerical dissipation or diffusion, usually linked with even-order derivatives in the
 1064 truncation error, signifies the artificial attenuation of the solution introduced by numerical
 1065 methods. For example, first-order upwind schemes inherently dampen waves. So, while
 1066 physically a wave might maintain its amplitude, numerically it could wane over time due
 1067 to this effect. In the context of DGSEM, the primary source of artificial damping is the
 1068 Riemann solvers at element boundaries. While the polynomial representation within an
 1069 element may be non-dissipative, the Riemann solvers, which facilitate information exchange
 1070 between elements, can introduce dissipation. This can lead to a slight reduction in amplitude
 1071 over extended simulation times. As detailed in Section 5.1 with the local Lax-Friedrichs
 1072 Riemann solver as an example, such damping effects, although vital for maintaining numerical
 1073 stability, do not necessarily compromise the spatial order of accuracy. The terms “numerical
 1074 dissipation” and “numerical diffusion” are often used interchangeably to address this damping
 1075 effect, especially when dealing with sharp gradients or discontinuities. However, “numerical
 1076 dissipation” typically emphasizes the removal of high-frequency components, especially in
 1077 the context of stabilizing a numerical solution. In contrast, “numerical diffusion” underscores
 1078 the artificial smoothing of particular features in the solution.

1079 Spurious oscillations represent another significant challenge in the numerical simulation
 1080 of physical phenomena, particularly when the mathematical models involve discontinuities
 1081 or steep gradients. These non-physical oscillations are most noticeable as “wiggles” or
 1082 “overshoots” in the vicinity of abrupt changes, such as shock waves or material interfaces,
 1083 and are indicative of the numerical method struggling to reconcile the sharp variations
 1084 in the solution’s profile. High-order numerical methods like SEMs, while offering enhanced
 1085 accuracy over smoother parts of the solution, are particularly susceptible to this phenomenon,
 1086 a manifestation of the well-documented “Gibbs phenomenon”. Spurious oscillations are
 1087 especially troublesome as they do not dissipate over time. Instead, they may intensify if
 1088 the numerical scheme lacks the necessary stability features, potentially compromising the
 1089 entire solution. However, the numerical community has developed several strategies to
 1090 suppress these oscillations, thus enhancing the fidelity of simulations. The introduction of
 1091 numerical dissipation, for example, can help to damp out these oscillations by smoothing the
 1092 solution in a controlled manner. Artificial viscosity is another effective tool, subtly altering
 1093 the equations to increase the physical diffusion, which helps to eliminate non-physical
 1094 fluctuations. Moreover, the implementation of carefully designed limiters can specifically
 1095 target and neutralize spurious oscillations without significantly distorting the true solution.

1096 **5.1 The Dissipative Local Lax-Friedrichs Riemann Solver and the Spatial** 1097 **Order of Accuracy of DGSEM**

1098 The numerical flux obtained using the local Lax-Friedrichs (LLF) Riemann solver can
 1099 be expressed as

$$F_{LLF} = \frac{1}{2} \{f(U_L) + f(U_R)\} - \frac{|\lambda|}{2} (U_L - U_R). \quad (54)$$

1100 Here, U_L and U_R represent the left and right states, respectively. The parameter $|\lambda|$ signifies
 1101 the maximum characteristic speed of the Riemann problem, commonly estimated as the
 1102 magnitude of the maximum eigenvalue or wave speed across U_L and U_R . The central flux
 1103 $\frac{1}{2} \{f(U_L) + f(U_R)\}$ is essentially the average of the fluxes from the left and right. On its
 1104 own, it is a second-order central scheme, prone to spurious oscillations near discontinuities.
 1105 The dissipative term $\frac{|\lambda|}{2} (U_L - U_R)$ acts to dampen those oscillations. It is proportional to

1106 the jump in the solution, so it is stronger (more dissipative) where the solution has steep
1107 gradients or discontinuities.

1108 In spectral element methods including DGSEM, the solution within each element is
1109 approximated by high-order polynomials. Hence, flux computation at boundaries does not
1110 solely rely on boundary values, as seen in many lower-order finite volume methods. Instead,
1111 the polynomial approximation of the internal solution is interpolated to the boundaries,
1112 ensuring high-order accuracy right up to the edge. Fluxes are then computed using these
1113 interpolated values from neighboring elements, with the LLF Riemann solver subsequently
1114 applied. It is crucial to note that the LLF solver’s primary role in this context is not flux
1115 computation but determining the upwind direction based on eigenvalues and introducing the
1116 necessary dissipation for numerical stability. The high-order accuracy of the spectral element
1117 method stems from its polynomial representation, not the Riemann solver. In simpler terms,
1118 the LLF Riemann solver does not cause first-order accuracy in finite volume methods. It is
1119 the low-order approximations of the left and right states, U_L and U_R , used as inputs. With
1120 DGSEM, both U_L and U_R are spectrally accurate, resulting in much smaller jumps. As
1121 such, while the Lax-Friedrichs method is intrinsically first order, the LLF Riemann solver
1122 does not degrade the DGSEM’s overall accuracy.

1123 Numerous works, such as Hussaini and Zang (1987), Boyd (1988), Cockburn and Shu
1124 (1989), Cockburn and Shu (1998), Hesthaven and Warburton (2007), Canuto et al. (2007b),
1125 Canuto et al. (2007a), and D. A. Kopriva et al. (2017) extensively explore spectral methods
1126 and their synergy with Riemann solvers. These studies imply that various Riemann solvers
1127 can integrate with spectral methods without compromising their inherent accuracy. Our
1128 convergence plots demonstrate that even with the LLF Riemann solver, we achieve the
1129 anticipated high-order accuracy typical of spectral element methods. Nonetheless, while the
1130 LLF Riemann solver might not diminish the accuracy order, it is known to introduce more
1131 dissipation than other Riemann solvers, potentially impacting the quality of the solution in
1132 terms of sharpness of features or the preservation of certain scales.

1133 6 Numerical Experiments

1134 We first outline the experimental procedure used to conduct these numerical experiments
1135 and verify the spatial and temporal orders of accuracy of the barotropic solver or the
1136 dynamical core of ocean models. We believe that this recipe will serve as a valuable resource
1137 to ocean modelers by ensuring that their respective ocean models actually converge at the
1138 expected order of accuracy. We proceed by plotting the time evolution of numerical errors,
1139 studying their nature, and creating convergence plots for each test case, with refinement in
1140 both space and time, only in space, and only in time.

1141 This comprehensive approach, involving three flavors of convergence tests, may seem
1142 overly detailed at first glance. However, it is chosen for a number of reasons. Consider
1143 an ocean model employing a low-order finite volume method for spatial discretization.
1144 The standard practice in ocean modeling is to conduct convergence studies by refining
1145 in both space and time, i.e., by simultaneously reducing the time step and cell width while
1146 maintaining their ratio (and the Courant number) constant. However, if a time-stepping
1147 method of order higher than the spatial discretization is used, a convergence plot with
1148 refinement in both space and time will always converge at the spatial order of accuracy in
1149 the asymptotic regime, thereby hindering the verification of the temporal order of accuracy.
1150 This is further compounded by the fact that the leading-order spatial error term’s coefficient
1151 is typically a few orders of magnitude larger than that of the leading-order temporal error
1152 term, a phenomenon we will refer to as leading-order coefficient discrepancy from here
1153 onward. Consequently, order reduction is seldom observed before reaching the asymptotic
1154 regime, and the convergence rate invariably mirrors the (low) spatial order of accuracy.
1155 Moreover, ocean models being typically characterized by their spatial discretization, may
1156 allow users to choose from multiple time-stepping methods. During the integration of a

1157 novel time-stepping method into a fully functional ocean model, a developer might want to
 1158 verify solely its order of accuracy, underscoring the necessity for self-refinement tests only
 1159 in time.

1160 In contrast, consider an ocean model where the spatial order of accuracy far surpasses
 1161 its temporal counterpart. With refinement in both space and time, order reduction may
 1162 be observed as the numerical solution error is expected to progress through three distinct
 1163 regimes: spatial discretization error dominance (first regime), temporal discretization error
 1164 dominance (second regime which overlaps with the beginning of the asymptotic regime
 1165 where Δx^α and Δt^β in (46) exert dominance over their respective coefficients), and finally,
 1166 round-off error dominance (third regime). However, in practice, for the selected sets of
 1167 discretization parameters Δx and Δt , the error might not traverse all three regimes. If
 1168 the round-off error takes over before the time integration error, verification of the temporal
 1169 accuracy order becomes impossible. Similarly, if the leading-order coefficient discrepancy is
 1170 insufficient, the first regime may be bypassed in favor of the second and third regimes even
 1171 at relatively low resolutions, preventing the verification of the spatial order of accuracy. This
 1172 demonstrates the necessity for self-refinement tests in both space and time. To mitigate the
 1173 impact of round-off errors in spectral element discretizations, it is crucial to avoid excessively
 1174 high polynomial orders during convergence studies. Last but not the least, self-refinement
 1175 tests in space can ensure that code modifications, such as incorporating a new time-stepping
 1176 method, do not inadvertently introduce bugs that detrimentally affect the spatial order of
 1177 accuracy.

1178 We now outline the experimental procedure for numerical experiments and convergence
 1179 studies below. After addressing the initial steps for spatial operators and their convergence,
 1180 which are common to all test cases, the procedure for individual test cases remains consistent.

1181 6.1 Experimental Procedure

- 1182 1. Construct the mesh for discretizing the numerical solution. This mesh will also be
 1183 used for visualization of the exact and numerical solutions, and the associated error.
 1184 Create a set of meshes with different spatial resolutions for conducting convergence
 1185 studies in both space and time, and only in space. For convergence studies only in
 1186 time, a single spatial mesh suffices.
- 1187 2. Specify a smooth function in space, which can be selected from the initial condition of
 1188 a test case. Evaluate both the exact and numerical spatial operators of this function
 1189 on the mesh, then plot these operators alongside their error. Ensure that the error
 1190 norm is considerably smaller than the operator norm, by at least several orders of
 1191 magnitude for high-order spectral element methods and a few orders for low-order
 1192 finite volume methods. Conduct convergence tests of these spatial operators with
 1193 spatial refinement to confirm that their convergence slopes align with the expected
 1194 spatial order of accuracy.
- 1195 3. Identify an exact or manufactured solution if applicable, keeping in mind that for finite
 1196 volume methods, the exact solutions pertain to cell- and edge-averaged quantities
 1197 rather than cell- or edge-centered ones. Consult Section C1 in Appendix C for
 1198 an insightful explanation on initializing these quantities on non-rectilinear meshes,
 1199 utilizing the hexagonal meshes of MPAS-Ocean as an illustrative example.
- 1200 4. Given a characteristic wave speed, choose an appropriate Courant number that is
 1201 consistent with the CFL condition for both the spatial and temporal discretizations.
 1202 Regarding the specification of the characteristic wave speed, consider the following
 1203 examples. For the coastal Kelvin and inertia-gravity wave test cases, define the
 1204 characteristic wave speed as the phase speed of the faster wave mode. For the
 1205 Rossby wave test cases, set the characteristic wave speed as the phase speed of the
 1206 fastest gravity waves emitted by the initially Gaussian monopole. For explicit time
 1207 integration methods, the CFL condition mandates that the Courant number must be
 1208 less than one to ensure stability. This requirement becomes even more stringent with

1209 explicit multistep time-integration methods, such as Adams-Bashforth, where the
 1210 region of absolute stability narrows with higher orders, necessitating an even smaller
 1211 Courant number. Based on this choice, determine the time step. Initialize the model
 1212 using the exact solution at $t = 0$. Implement boundary conditions that mirror the
 1213 exact solution over time. Likewise, define space- and time-dependent source terms
 1214 for manufactured solutions. For detailed guidelines on setting boundary conditions
 1215 and source terms on non-rectilinear meshes, refer to Sections C1 and C2 in Appendix
 1216 C, again using the hexagonal meshes of MPAS-Ocean as a reference. Run the model
 1217 forward in time to obtain the numerical solution. At intervals equivalent to integral
 1218 multiples of the time step, print and plot both the exact and numerical solutions,
 1219 along with the associated error, to study their temporal evolution.

- 1220 5. Employ visual inspection (sometimes humorously referred to as the ‘eyeball norm’)
 1221 to assess the numerical solution for approximate physical and numerical accuracy,
 1222 examining, for instance, whether geophysical waves propagate at their theoretically
 1223 expected phase speeds. If errors significantly amplify along the boundaries compared
 1224 to the domain’s interior, reevaluate the implementation of boundary conditions or the
 1225 plotting of boundary values. As with the spatial operators, the error norm should
 1226 be substantially smaller than the solution norm, with the difference being more
 1227 pronounced for high-order spectral element methods than low-order finite volume
 1228 methods.
- 1229 6. After achieving satisfactory preliminary results, initiate comprehensive convergence
 1230 studies, with refinements in both space and time, only in space, and only in time.
 1231 Revisit the beginning of this section for the underlying reasoning behind these different
 1232 flavors of convergence tests and specific strategies tailored for low- and high-order
 1233 spatial discretizations. For refinement in both space and time, adjust the time step in
 1234 direct proportion to the cell width, ensuring that their ratio and the Courant number
 1235 remain constant. When refining only in space, determine the time step for the finest
 1236 mesh using the Courant number. Employ this stringent time step across all spatial
 1237 resolutions. For convergence tests with refinement only in time, calculate the largest
 1238 time step based on the Courant number for the singular spatial mesh in use.
- 1239 7. The refinement ratio between successive pairs of spatial or temporal resolutions does
 1240 not necessarily need to be an integer. This flexibility is particularly advantageous for
 1241 convergence tests only in space, the most computationally intensive type. Following
 1242 that in computational demand is the convergence test in both space and time, and
 1243 finally the convergence test only in time. The error norm in a convergence test is
 1244 calculated at a specific time horizon. This horizon is always reached if:
 - 1245 (a) refinement is performed only in space, implying a constant time step value;
 - 1246 (b) the time horizon equates to an integral number of the largest time step, and the
 1247 refinement ratio is integral e.g doubling each time.

1248 This may not hold true for convergence tests with refinement in both space and time
 1249 or only in time when the refinement ratio is not an integer. Nonetheless, a clever
 1250 approach can circumvent this issue. By selecting a rational refinement ratio, $r = p/q$
 1251 for $p > q$ and $p, q \in \mathbb{Z}^+$, and denoting s as the number of different resolution sets, we
 1252 can define the time horizon as $T = N\Delta t_{\text{largest}}$, with $N = q^t$, $t \in \mathbb{Z}^+$ and $t \geq s$. As
 1253 lengthy simulation times are generally unnecessary for convergence tests, t does not
 1254 need to greatly exceed s . For example, with $r = 3/2$ and $s = 5$, we can choose N to
 1255 be powers of 2 equal to or greater than 32. This ensures that the time horizon aligns
 1256 with integral multiples of every time step used in the study, obviating the need for
 1257 adjustments that could lead to errors.

- 1258 8. For refinement in both space and time, employ a test case with either an exact or a
 1259 manufactured solution, and plot the actual error norm at a designated time horizon
 1260 against either the cell width or the total number of cells. For refinement only in space
 1261 or only in time, plot the norm of the difference between
 - 1262 (a) the numerical solutions; or
 - 1263 (b) the error (for test cases equipped with exact solutions);

1264 against the cell width (or number of cells) or the time step (or number of time steps)
 1265 for successive pairs of spatial and temporal resolutions.

1266 9. Analyze whether the convergence slope:

- 1267 (a) aligns with the spatial or temporal order of accuracy when refining only in space
 1268 or only in time;
- 1269 (b) corresponds to the lesser of the spatial and temporal orders of accuracy when
 1270 refining in both space and time.

1271 If the above observations hold true, our results are satisfactory. However, deviations
 1272 from these patterns may point to issues such as:

- 1273 (a) a bug within the numerical implementation of spatial or temporal discretizations;
- 1274 (b) the asymptotic regime not yet reached by the spatial and temporal resolutions,
 1275 suggesting a need for broader resolution sets in convergence studies.
- 1276 (c) the dominance of round-off errors, a common issue in high-order spectral element
 1277 methods, which can be remedied by reducing the polynomial order.

1278 10. In scenarios where machine precision constraints may preclude reaching the asymptotic
 1279 regime, separate spatial and temporal convergence tests are crucial. It is also vital to
 1280 diversify test cases, given that error magnitudes can vary based on the exact solution
 1281 and its gradients.

1282 The above procedure sets the stage for a rigorous numerical study that can adapt to different
 1283 scenarios, accounting for the particularities and complexities inherent to both finite volume
 1284 and spectral element methods, and offering flexibility in convergence testing and verification.

1285 6.2 Numerical Solutions and Convergence Plots

1286 Based on our experimental procedure, we begin by testing the convergence of the various
 1287 spatial operators. For the TRiSK-based mimetic finite volume method, these encompass the
 1288 gradient, divergence, curl, kinetic energy, and Laplacian operators as well as the interpolation
 1289 or flux-mapping operator. This last operator is used to obtain the tangential velocity on
 1290 an edge from the normal velocities on the edges of the cells sharing that edge. In contrast,
 1291 for DGSEM, the only pertinent spatial operators are the zonal and meridional gradient
 1292 operators.

1293 We opt for a smooth spatial test function, which, along with its gradient and Laplacian,
 1294 is expressed as:

$$\eta = \hat{\eta} \sin\left(\frac{2\pi x}{L_x}\right) \sin\left(\frac{2\pi y}{L_y}\right), \quad (55a)$$

$$\begin{aligned} \nabla\eta &= \eta_x \mathbf{i} + \eta_y \mathbf{j} \\ &= 2\pi\hat{\eta} \left\{ \frac{1}{L_x} \cos\left(\frac{2\pi x}{L_x}\right) \sin\left(\frac{2\pi y}{L_y}\right) \mathbf{i} + \frac{1}{L_y} \sin\left(\frac{2\pi x}{L_x}\right) \cos\left(\frac{2\pi y}{L_y}\right) \mathbf{j} \right\}, \end{aligned} \quad (55b)$$

$$\nabla^2\eta = \nabla \cdot \nabla\eta = - \left\{ \left(\frac{2\pi}{L_x}\right)^2 + \left(\frac{2\pi}{L_y}\right)^2 \right\} \eta. \quad (55c)$$

1295 By defining the surface elevation via (55a), the components of the geostrophic velocity field
 1296 emerge as $u = -g/f\eta_y$ and $v = g/f\eta_x$, where $g = 10 \text{ m s}^{-2}$ and $f = 10^{-4} \text{ s}^{-1}$. If an
 1297 edge's normal forms an angle θ with the positive direction of the zonal axis, the velocity
 1298 field components in the normal (\mathbf{n}) and tangential ($\mathbf{t} = \mathbf{k} \times \mathbf{n}$) directions are represented
 1299 as $\mathbf{u}^n = \mathcal{N}\mathbf{u} = u \cos\theta + v \sin\theta$ and $\mathbf{u}^t = \mathcal{T}\mathbf{u} = v \cos\theta - u \sin\theta$. The vertical component of
 1300 the curl of the velocity field, the kinetic energy, and the Laplacian of the normal velocity at

1301 the edges are defined as

$$\zeta = \mathbf{k} \cdot \nabla \times \mathbf{u} = \mathbf{k} \cdot \nabla \times (u\mathbf{i} + v\mathbf{j}) = v_x - u_y = \frac{g}{f} \nabla^2 \eta, \quad (56a)$$

$$K = \frac{1}{2} |\mathbf{u}|^2 = \frac{1}{2} (u^2 + v^2) = \frac{g^2}{2f^2} (\eta_x^2 + \eta_y^2), \quad (56b)$$

$$\nabla^2 \mathbf{u}^n = \frac{g}{f} \nabla^2 (-\eta_y \cos \theta + \eta_x \sin \theta) = -\frac{g}{f} \nabla^2 \mathcal{T} \nabla \eta = \frac{g}{f} \left\{ \left(\frac{2\pi}{L_x} \right)^2 + \left(\frac{2\pi}{L_y} \right)^2 \right\} \mathcal{T} \nabla \eta. \quad (56c)$$

1302 It is worth noting that although our test function was defined by (55), any function exhibiting
 1303 smooth spatial variation in both zonal and meridional directions, such as the initial conditions
 1304 for the geophysical waves or the manufactured solution, would have served the purpose.

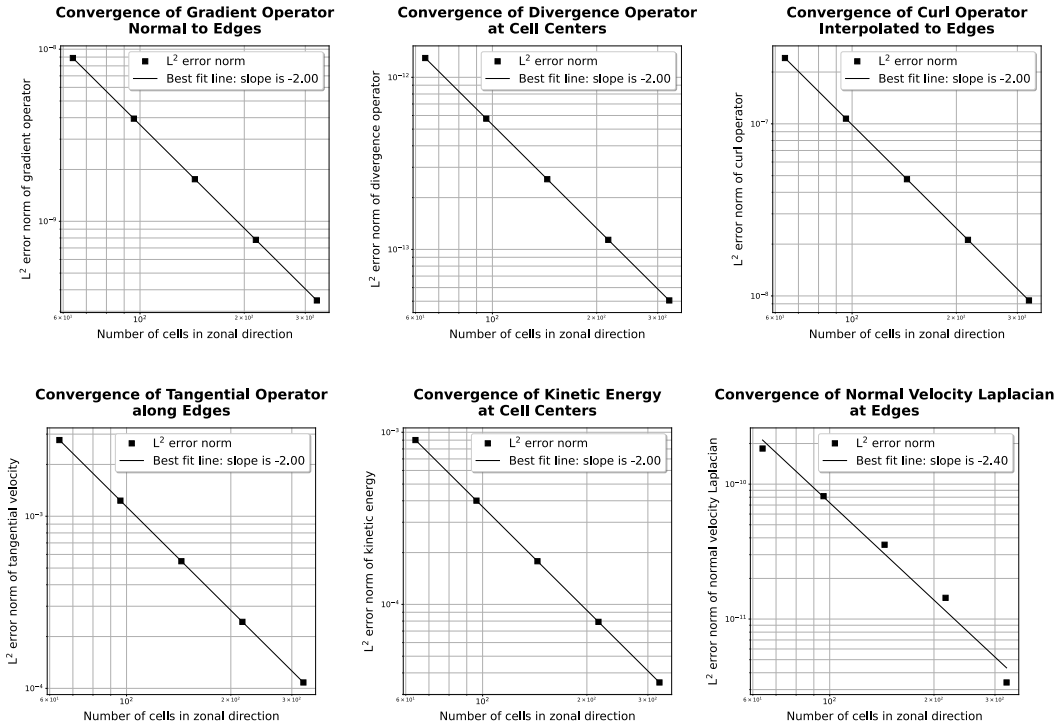


Figure 8. Convergence of TRiSK-based spatial and flux-mapping operators applied to the test function (55) on a uniform MPAS-Ocean mesh.

1305 Figure 8 displays the convergence plots for the TRiSK-based spatial operators, which
 1306 are all second-order accurate as expected. These studies were carried out on uniform planar
 1307 hexagonal MPAS-Ocean meshes. These meshes have an equal number of cells, say N , in
 1308 both zonal and meridional directions. Each row is offset by half a cell width, and the
 1309 configuration ensures that the regular hexagons' parallel sides align with the meridional
 1310 direction. Given that Δx denotes the distance between cell centers, the side length of these
 1311 hexagonal cells is $1/\sqrt{3}\Delta x$. Consequently, the leading-order spatial discretization error term
 1312 for the second-order TRiSK scheme can be represented as $\mathcal{O}(\Delta x^2)$. With the zonal domain
 1313 extent set to $L_x = N\Delta x$, maintaining a constant L_x while increasing N means a log-log
 1314 plot of the error norm against N will display a slope identical in magnitude to that against
 1315 Δx . Hence, in our plots, we designate the x -axis as the cell count N , a choice enhancing
 1316 visualization as refinement progresses in the positive x -direction.

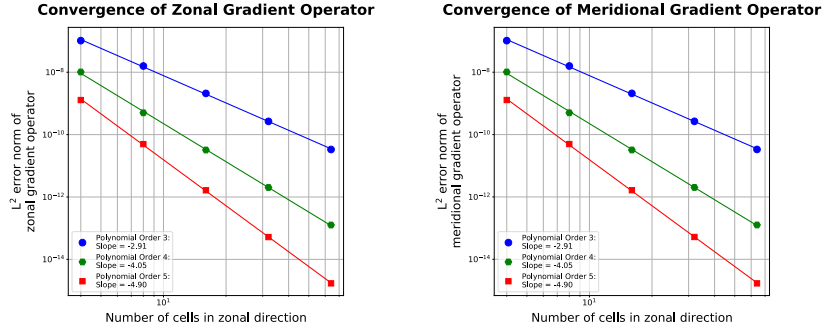


Figure 9. Convergence of weak forms of the zonal and meridional gradient operators of DGSEM applied to the test function (55) for polynomial orders 3, 4, and 5.

1317 Figure 9 displays the convergence plots for the weak forms of DGSEM’s zonal and
 1318 meridional gradient operators, utilizing the Bassi-Rebay method (Bassi & Rebay, 1997) to
 1319 approximate functions at the element boundaries. Notably, the convergence slopes align
 1320 with the orders of the polynomial basis functions. Although not depicted here, additional
 1321 convergence tests were performed on the strong form of these gradient operators, yielding
 1322 identical results. In our spectral element meshes, we specified the number of elements N ,
 1323 the length of each element Δx , and the order of the polynomial basis functions p to be the
 1324 same in both the zonal and meridional directions. For complete functions, the leading-order
 1325 spatial error term for our DGSEM solution takes the form

$$\varepsilon = k_1 \exp(-k_2 p) \Delta x^p, \quad (57)$$

1326 where k_1 and k_2 are constants. Equation (57) follows from the in-depth error analysis of
 1327 DGSEMs in spectral element textbooks by Karniadakis and Sherwin (2005), Hesthaven and
 1328 Warburton (2007), and Canuto et al. (2007b). Taking the logarithm of both sides of (57)
 1329 gives

$$\ln \varepsilon = \ln k_1 - k_2 p + p \ln \Delta x = k_3 - p(k_2 - \ln \Delta x). \quad (58)$$

1330 We recall from Section 3.2 that a spatial refinement in DGSEM can be performed in
 1331 two ways: by increasing p while maintaining a constant N (p -refinement), or vice versa
 1332 (h -refinement, where h denotes the cell width Δx). Equation (58) shows that p -refinement
 1333 is expected to yield a straight line with negative slope of magnitude $k_2 - \ln \Delta x$ on a log-log
 1334 graph, demonstrating exponential convergence. In contrast, an h -refinement should render
 1335 a straight line with a slope of magnitude p , akin to finite difference or finite volume methods.
 1336 Moreover, p -refinement is not applicable in the context of the TRiSK-based finite volume
 1337 method, for which the effective polynomial order remains fixed at second order. To ensure
 1338 a consistent and clear presentation, we have chosen to display the spatial convergence plots,
 1339 employing h -refinement, for both DGSEM and TRiSK in a sequential and organized manner.

1340 The Courant number, critical for the stability of numerical simulations, can be defined
 1341 for two-dimensional advective problems as

$$C = \Delta t \left(\frac{c_x}{\Delta x} + \frac{c_y}{\Delta y} \right), \quad (59)$$

1342 where c_x and c_y are wave speeds, while Δx and Δy denote grid scales in the zonal and
 1343 meridional directions respectively. For DGSEM, employing rectangular elements with side
 1344 lengths Δx and Δy , the Courant number modifies to

$$C = \Delta t \left(\frac{c_x}{\frac{\Delta x}{P_x^2}} + \frac{c_y}{\frac{\Delta y}{P_y^2}} \right) = \Delta t \left(P_x^2 \frac{c_x}{\Delta x} + P_y^2 \frac{c_y}{\Delta y} \right), \quad (60)$$

1345 where P_x and P_y represent the orders of the polynomial basis function in the zonal and
 1346 meridional directions respectively. Given that the internal grid of each spectral element has
 1347 higher density towards the edges, the measures $\Delta x/P_x^2$ and $\Delta y/P_y^2$ offer close estimates for
 1348 the smallest internal grid spacings adjacent to these edges. In uniform planar hexagonal
 1349 MPAS-Ocean meshes, where Δx indicates the distance between neighboring cell centers,
 1350 and in DGSEM meshes using spectral elements with side lengths Δx and polynomial order
 1351 P in both horizontal directions, the CFL condition can be concisely represented as

$$C = \lambda \Delta t / \Delta x, \text{ where } \lambda = \begin{cases} c_x + \frac{2}{\sqrt{3}} c_y & \text{for TRiSK,} \\ c_x + c_y & \text{for DGSEM.} \end{cases} \quad (61)$$

1352 In our simulations, we specify c_x and c_y to be the zonal and meridional components of the
 1353 phase speed for the manufactured wave solution; the phase speed of the faster wave mode
 1354 for the coastal Kelvin and inertia-gravity waves; and the phase speed of the component
 1355 waves of the standing wave mode with faster components for the barotropic tide.

1356 In each horizontal direction, let N represent the number of hexagonal cells for TRiSK
 1357 and the count of spectral elements for DGSEM. Additionally, let P symbolize the polynomial
 1358 order in each direction for DGSEM. For the TRiSK-based approach, we utilize a structured
 1359 planar hexagonal MPAS-Ocean mesh with $N = 100$. The spectral element mesh for DGSEM
 1360 is defined by $N = 5$ and $P = 10$ in all test cases except for the Rossby waves, resulting in
 1361 10^{th} order spatial accuracy. For the Rossby wave test cases, we specify $N = 10$ and $P = 7$,
 1362 yielding a 7^{th} order spatial accuracy. The zonal domain extent, L_x is specified as 5×10^6 m,
 1363 10^7 m, 10^6 m, 2.5×10^5 m, and 10^7 m for the coastal Kelvin wave, the inertia-gravity wave,
 1364 the Rossby waves, the barotropic tide and the manufactured solution test cases respectively.
 1365 The distance between the adjacent hexagonal cell centers for TRiSK, as well as the side
 1366 lengths of the spectral elements for DGSEM are given by $\Delta x = L_x/N$. For DGSEM, the
 1367 smallest grid spacings near element boundaries are approximately $\Delta x/P^2$. The meridional
 1368 domain extent L_y is set to $\sqrt{3}/2L_x$ for TRiSK, resulting in a “measure” for the meridional
 1369 grid scale $\Delta y = L_y/N = \sqrt{3}/2\Delta x$. For DGSEM, L_y , Δy , and the meridional grid spacings
 1370 mirror their zonal counterparts. By leveraging (61) to maintain the Courant number, C ,
 1371 near 0.5, we specify the time step, Δt , in the coastal Kelvin wave, inertia-gravity wave,
 1372 barotropic tide, and manufactured solution test cases to be 200 s, 100 s, 10 s, and 180
 1373 s respectively for TRiSK, and 50 s, 25 s, 2.5 s, and 30 s respectively for DGSEM. For
 1374 the Rossby wave test cases, a particularly small $\Delta t = 0.5$ s is selected for both TRiSK
 1375 and DGSEM to meet the CFL condition for the fastest gravity waves, ensuring numerical
 1376 stability.

1377 The numerical solutions being visually indistinguishable from their exact counterparts,
 1378 we limit our presentation to the time evolution of surface elevation errors for the coastal
 1379 Kelvin wave, inertia-gravity wave, barotropic tide, and the non-linear manufactured solution,
 1380 as shown in Figures 10, 11, 12, and 13. These solutions are advanced with Williamson’s
 1381 low-storage third-order Runge-Kutta time-stepping method, and spatially discretized with
 1382 TRiSK and DGSEM. The error stemming from these two types of spatial discretizations is
 1383 depicted in the first and second rows of Figures 10–13. At first glance, we notice that the
 1384 TRiSK error is three orders of magnitude less than the solution magnitude for the linear
 1385 coastal Kelvin wave, inertia-gravity wave, and barotropic tide test cases. It is two orders of
 1386 magnitude less for the non-linear manufactured solution test case. Conversely, the DGSEM
 1387 error is six orders of magnitude less than the solution error for the coastal Kelvin wave and
 1388 barotropic tide test cases, and eight orders of magnitude less for the inertia-gravity wave
 1389 and manufactured solution test cases.

1390 In our analysis of the temporal evolution of the coastal Kelvin wave error for both
 1391 TRiSK and DGSEM (Figure 10), it is evident that the error modes propagate not only
 1392 meridionally from north to south in line with the wave direction, but also zonally from west
 1393 to east. Even though the exact tendency of the zonal velocity in the linear rotating shallow
 1394 water equations (10) is zero, due to a balance between the exact Coriolis and pressure

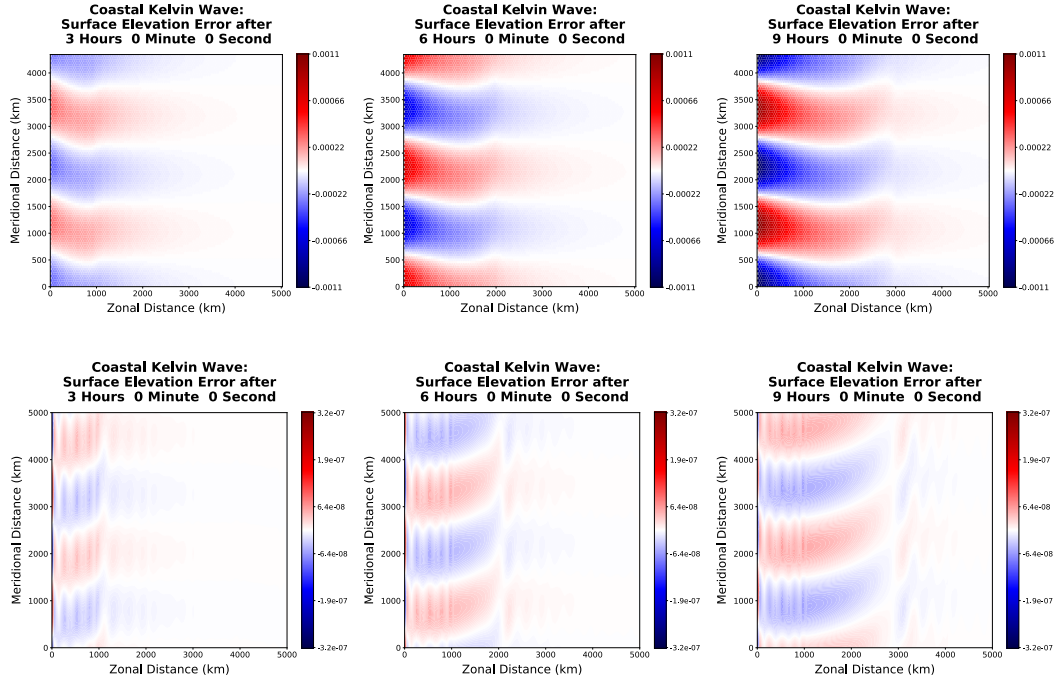


Figure 10. Time evolution of the surface elevation error of TC1, the coastal Kelvin wave, spatially discretized with the TRiSK-based mimetic finite volume method (first row), and DGSEM using 5 elements and polynomial basis functions of order 10 in each horizontal direction (second row).

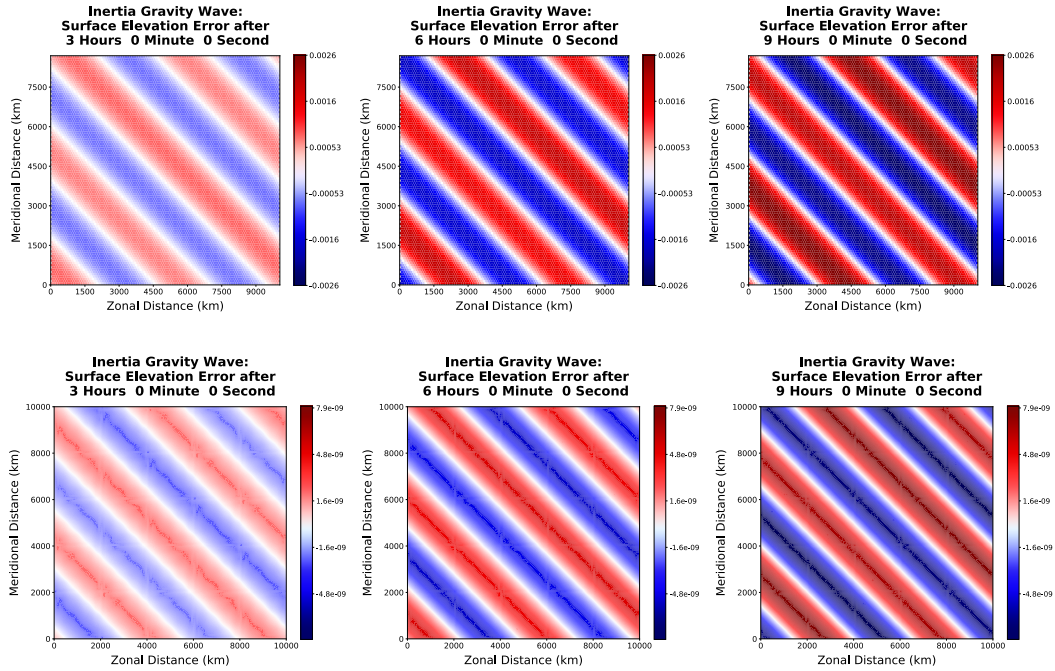


Figure 11. Same as Figure 10, but for TC2, the high-frequency dispersive inertia-gravity wave, showing error for TRiSK (first row), and DGSEM (second row).

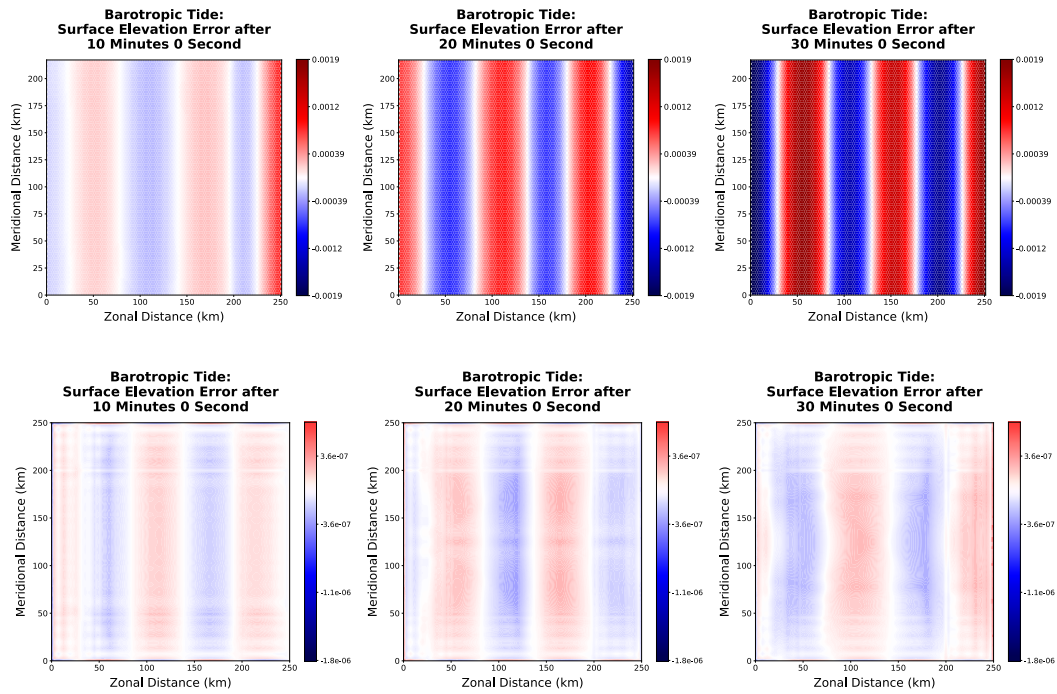


Figure 12. Same as Figure 10, but for TC5, the barotropic tide test case, showing error for TRiSK (first row), and DGSEM (second row).

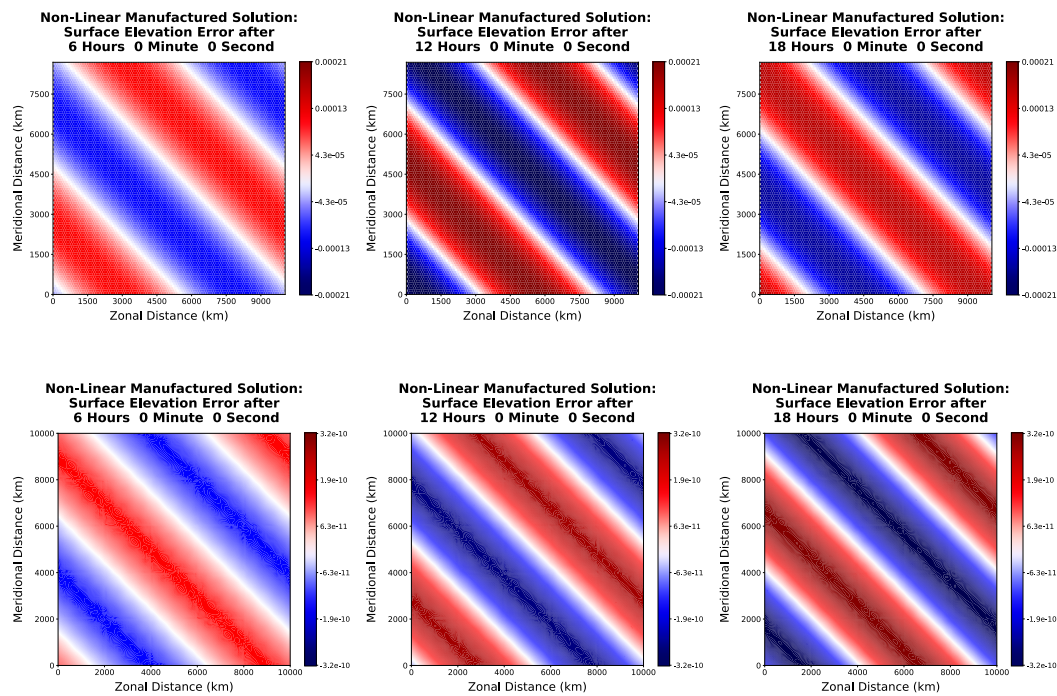


Figure 13. Same as Figure 10, but for TC6, the non-linear manufactured solution test case, showing error for TRiSK (first row), and DGSEM (second row).

1395 gradient terms in (10a), its numerical counterpart is not. Referring to our discussion in
 1396 Section 4.2, the spatial discretization error in the pressure gradient term of (10a) is of order
 1397 $\mathcal{O}(\Delta x^\alpha)$. This non-zero error gives rise to a discernible numerical zonal velocity, serving
 1398 as a catalyst for the error modes to propagate in both zonal and meridional directions.
 1399 Moreover, the western boundary, characterized by high gradients and the imposition of a
 1400 no-normal flow condition, act as an incubator for error. As the simulation progresses, the
 1401 errors originating from this boundary permeate the interior domain. Notably, these error
 1402 modes propagate at speeds identical to the shallow water gravity wave speed, a reflection
 1403 of the system’s inherent physics. Interested readers may consult Figure A1 in Appendix A,
 1404 which depicts the exact solution plots for a plane wave test case traveling at the gravity wave
 1405 speed. They will observe a notable similarity between these plots and the aforementioned
 1406 error modes. Such behavior underscores the principle that errors in numerical simulations
 1407 tend to mirror the dynamics of the governing equations. This, in conjunction with the zonal
 1408 error propagation, may account for the prominent west-to-east movement of errors observed.
 1409 A distinctive front-like feature is observed migrating from west to east. Our interpretation
 1410 suggests that this front represents the initial “boundary layer” of error, emanating from the
 1411 western boundary. As this layer advances eastward, it collides with the pre-existing errors,
 1412 predominantly moving southward. This intricate dance between the boundary-induced and
 1413 interior error modes gives birth to the observed “front”.

1414 We recall that the prescribed exact solutions for both the coastal and inertia-gravity
 1415 waves are constructed as a superposition of two wave modes. The second mode possesses
 1416 twice the amplitude and wavenumber relative to the first. Owing to the inherently dispersive
 1417 nature of the inertia-gravity wave, these modes propagate with different phase speeds. This
 1418 disparity in propagation speeds is manifested by the temporal variation of the solution’s
 1419 amplitude and the width of its positive and negative “bands” (Figure 2). Intriguingly,
 1420 the error exhibits analogous behavior. Given the absence of physical boundaries combined
 1421 with the imposition of periodic boundary conditions, the error advances coherently in the
 1422 direction of the solution (Figure 11). This observation again underscores that the system’s
 1423 underlying physics significantly shapes the error’s dynamics, mirroring the solutions of the
 1424 governing equations.

1425 The barotropic tide test case serves as a benchmark for evaluating an ocean model’s
 1426 proficiency in simulating standing waves, a critical feature for coastal applications. While
 1427 an initial assessment based on error magnitude (Figure 12) and convergence rate (Figure 18)
 1428 suggests promising results for both TRiSK and DGSEM, a closer examination of the DGSEM
 1429 error plots uncovers patterns that could be attributed to either spurious oscillations or
 1430 numerical dispersion. On the other hand, the inherent dissipation of TRiSK damp out
 1431 potential oscillations and dispersive errors that the more accurate DGSEM tends to pick
 1432 up. It is worth noting that despite these subtle numerical artifacts observed in DGSEM,
 1433 which were discernible only upon meticulous examination, the error magnitude for DGSEM
 1434 remains significantly lower than that of TRiSK at equivalent or even lower spatial resolution.

1435 Finally, interpreting the error dynamics of the non-linear manufactured solution test
 1436 case (Figure 13) can be notably challenging. Nonlinearities inherently introduce a range of
 1437 complex interactions and dependencies between different solution features. While in linear
 1438 settings numerical artifacts like dispersion and oscillations may have predictable patterns, in
 1439 non-linear contexts these patterns can be distorted, merged, or even amplified in unexpected
 1440 ways. The intricacies of non-linear interactions can often cloak or overshadow the typical
 1441 behaviors we associate with numerical errors. As a result, even when we observe smooth
 1442 error fields as in Figure 13, these might be the consequence of numerous intertwined effects
 1443 which, in isolation, would appear differently. This complexity not only complicates our
 1444 ability to decipher the source or nature of errors but also underscores the importance
 1445 of supplementing visual error assessments with quantitative tools like convergence plots
 1446 (Figure 19) in non-linear scenarios.

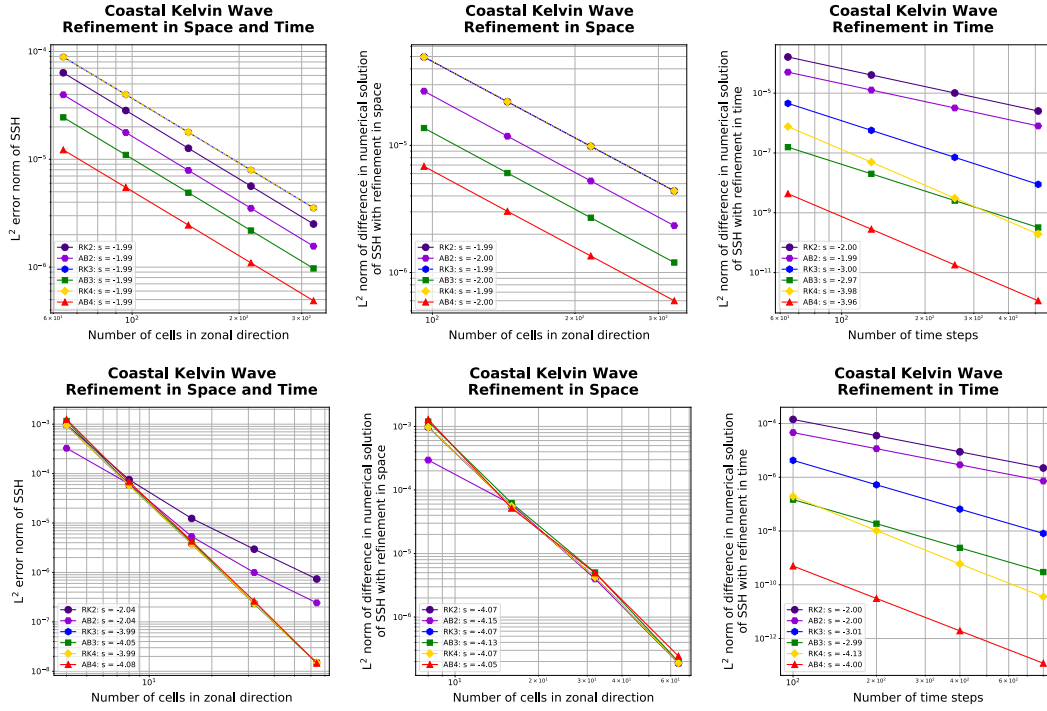


Figure 14. Convergence plots of TC1, the non-dispersive coastal Kelvin wave, discretized with TRiSK (first row) and DGSEM (second row), for refinement in space and time (first column), refinement in space (second column), and refinement in time (third column). The slope of the best-fit line, s , is shown in each legend.

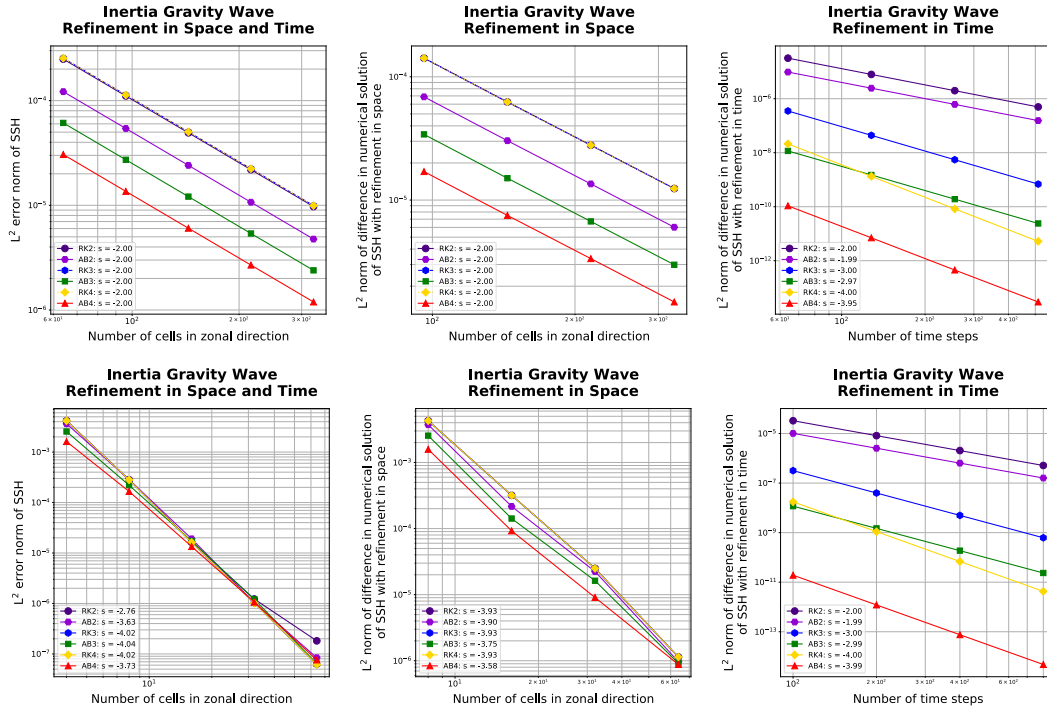


Figure 15. Same as Figure 14, but for TC2, the dispersive inertia-gravity wave.

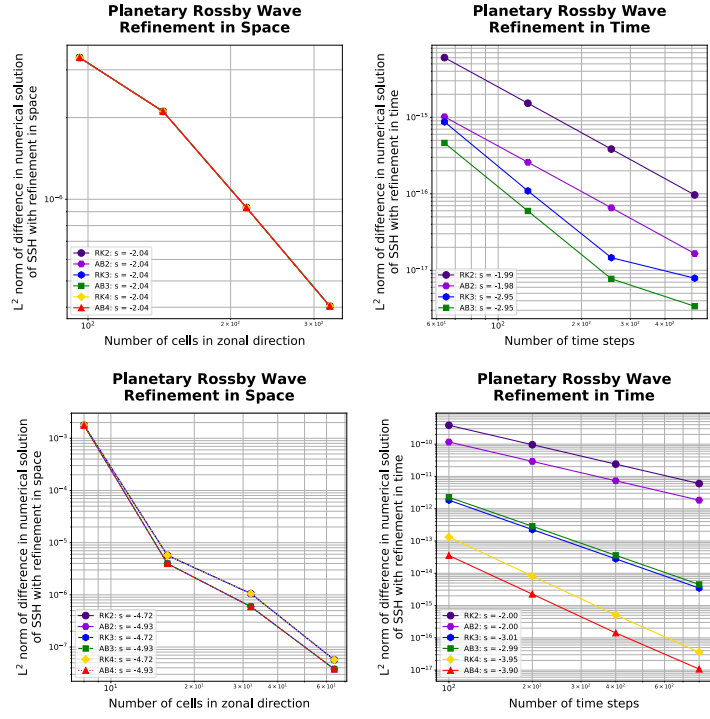


Figure 16. Convergence plots of the solution difference norm of TC3a, the linear dispersive planetary Rossby wave, discretized with TRiSK (first row) and DGSEM (second row), for refinement in space (first column), and refinement in time (second column). The slope of the best-fit line, s , is shown in each legend.

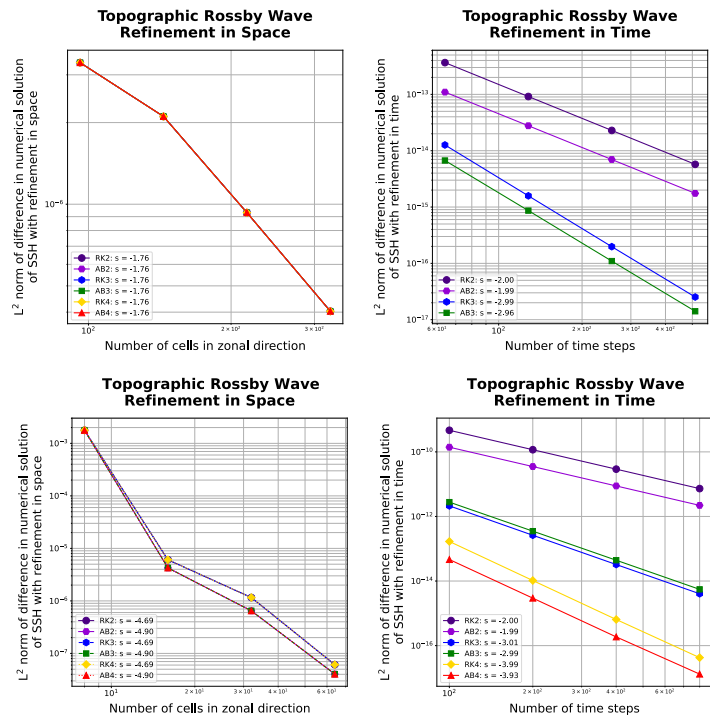


Figure 17. Same as Figure 16, but for TC4a, the linear dispersive topographic Rossby wave.

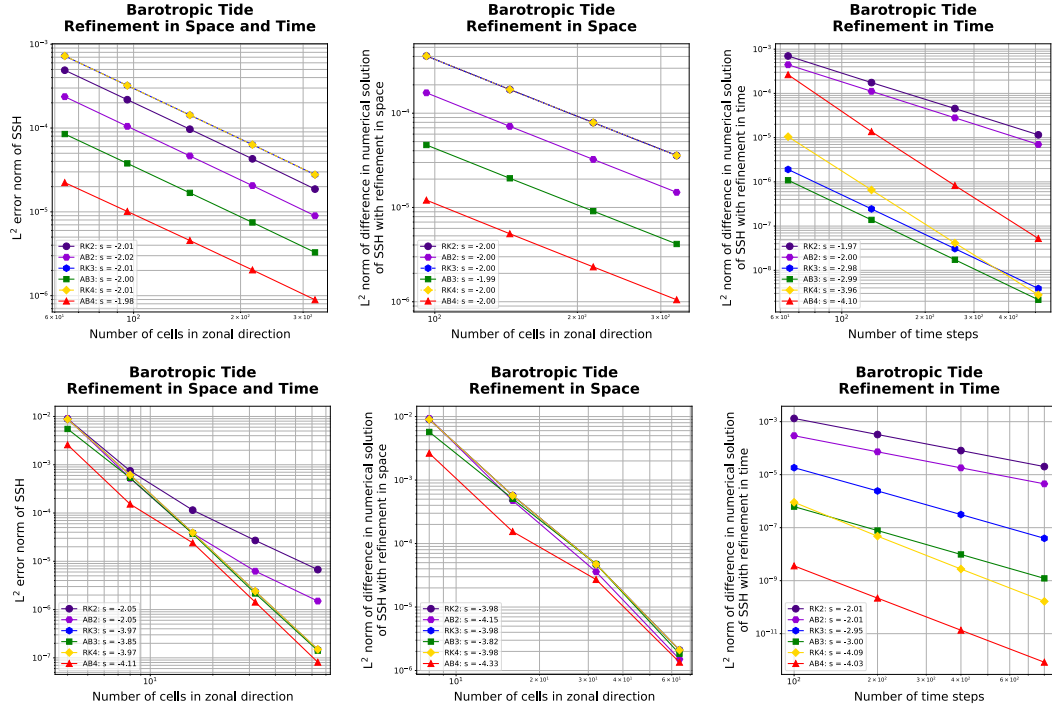


Figure 18. Convergence plots of TC5, the barotropic tide, discretized with TRiSK (first row) and DGSEM (second row), for refinement in space and time (first column), refinement in space (second column), and refinement in time (third column).

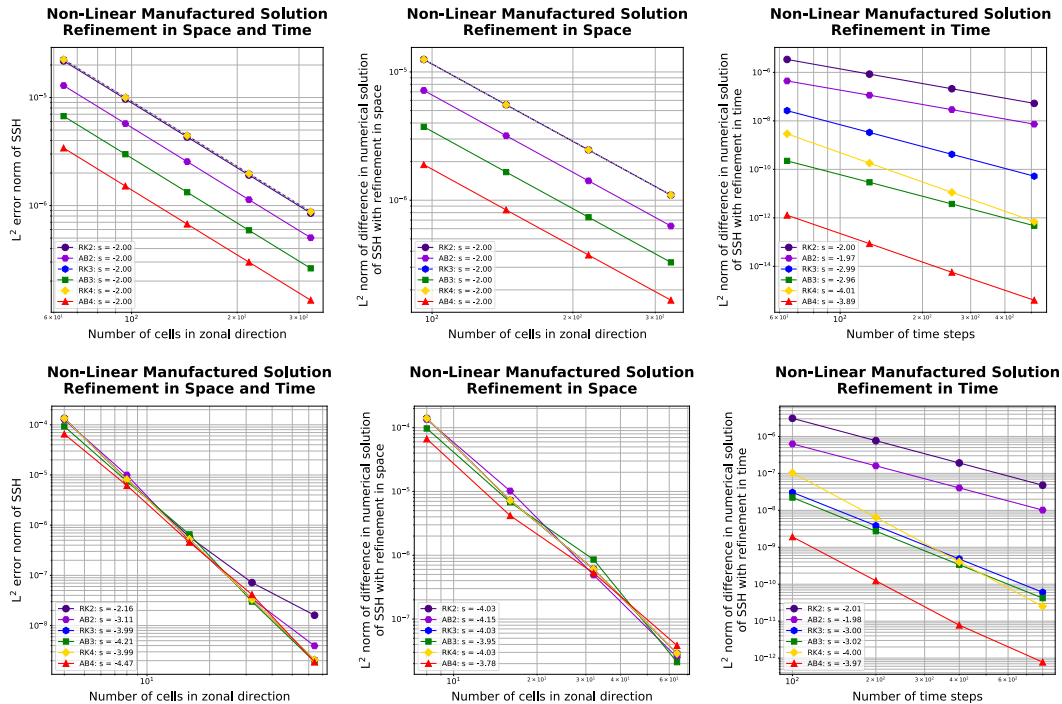


Figure 19. Same as Figure 18, but for TC6, the non-linear manufactured solution.

1447 We have examined the plots produced by DGSEM on low-resolution spectral element
 1448 meshes. Coarsening was executed by diminishing the polynomial order (p -coarsening) as
 1449 well as the number of elements (h -coarsening). To maintain brevity, we have opted not to
 1450 include these results in this paper. However, interested readers can download the output
 1451 files for each test case detailed in the main paper and in Appendix A from Bishnu (2024a),
 1452 and review the low p - and h -resolution plots in the designated subdirectories of the DGSEM
 1453 output directory. These subdirectories exist for all test cases equipped with exact solutions,
 1454 and contain the numerical solution and error plots. The spectral element mesh used in the
 1455 low p -resolution simulations was configured with 5 elements and polynomial basis functions
 1456 of order 4 in each horizontal direction. In contrast, the mesh for the low h -resolution
 1457 simulations was designed with 2 elements and polynomial basis functions of order 10 in each
 1458 direction. The low-resolution plots reveal an increase in numerical dispersion and dissipation
 1459 effects (Section 5). Notably, numerical dispersion often becomes more pronounced in coarser
 1460 meshes, where the fidelity of the physical phenomena’s representation is compromised due
 1461 to the lower resolution. This manifests as significant alterations in wave speeds and wave
 1462 shapes, leading to attenuation of the signal in some parts of the domain and amplification
 1463 in others. While these dispersive effects are imperceptible in the high-resolution DGSEM
 1464 solution of the physically non-dispersive Kelvin wave, they become conspicuous in the low
 1465 resolution solution, particularly with lower than three elements and third-order polynomial
 1466 basis functions in each direction. It alters the phase speed of the component waves of
 1467 different wavelengths, thereby distorting the resultant wave’s initial profile as the simulation
 1468 progresses. Concurrently, the utilization of the LLF Riemann solver—implemented to
 1469 dampen spurious oscillations at the spectral elements’ boundaries—introduces its own brand
 1470 of error, that of a dissipative nature. A coarser mesh exacerbates this error, as there are
 1471 fewer elements to absorb the impact of these dissipative effects. It is manifested by the
 1472 errors assuming predominantly higher magnitudes along the element boundaries.

1473 Figures 14, 15, 18, and 19 show the convergence plots of the surface elevation error for
 1474 the coastal Kelvin wave, the inertia-gravity wave, the barotropic tide, and the non-linear
 1475 manufactured solution, respectively. The refinement is performed by keeping $\Delta t \propto \Delta x$
 1476 (first column), only refining in space (second column), and only refining in time (third
 1477 column). The numerical solutions in the first rows of these figures have been discretized
 1478 with the TRiSK-based mimetic finite volume method, while the ones in the second row
 1479 have been discretized with DGSEM. Given the absence of exact solutions for the planetary
 1480 and topographic Rossby wave test cases, we cannot ascertain their error, which is essential
 1481 for convergence studies with both spatial and temporal refinement. Consequently, we plot
 1482 the norm of the differences between numerical solutions over successive pairs of spatial and
 1483 temporal resolutions, refined at a constant ratio, to verify the spatial and temporal orders of
 1484 accuracy (Section 4.5). Figures 16 and 17 showcase these convergence plots for the planetary
 1485 and topographic Rossby waves respectively, discretized with TRiSK (first row) and DGSEM
 1486 (second row), for refinement only in space (first column) and only in time (second column).
 1487 For refinement in both space and time, we utilize the Courant number formulation in (61)
 1488 to first determine the time step Δt on the coarsest mesh, and then reduce this maximum Δt
 1489 proportional to Δx for the remaining meshes. Similarly, by leveraging (61), we determine
 1490 (a) the largest Δt at a fixed spatial resolution for refinement only in time, and (b) the Δt
 1491 on the finest mesh for refinement only in space, ensuring it meets the CFL condition for
 1492 the remaining meshes where it is also implemented. The time horizon is specified using
 1493 the largest Δt as stipulated in point 7 of the experimental procedure of Section 6.1. The
 1494 actual time-stepping methods corresponding to their abbreviated notations in the legends
 1495 of the convergence plots can be obtained from List 1. The slope of the best fit line for each
 1496 time-stepping method is denoted by s .

1497 The convergence slopes agree with the theoretical predictions in Bishnu (2021). As
 1498 highlighted in point 9(c) of the experimental procedure outlined in Section 6.1, employing
 1499 an exceedingly high-order DGSEM for convergence studies may not be optimal. This is
 1500 attributed to the prevalence of round-off errors during spatial refinement, which manifest

1501 before the resolutions attain the asymptotic regime. To mitigate this, we only utilize
 1502 fourth-order polynomial basis functions. The observed convergence slopes of approximately
 1503 four in the spatial-only refinement plots for DGSEM confirm their fourth-order spatial
 1504 accuracy. When refining in both space and time, we note that the asymptotic order of
 1505 convergence matches the minimum of the spatial and temporal orders of accuracy. Since
 1506 asymptotic convergence is observed with the second-order TRiSK scheme for refinement
 1507 in both space and time, third- and fourth-order Runge-Kutta and Adams-Bashforth time
 1508 integrators do not result in higher than second-order convergence rates. For this reason,
 1509 it is imperative to perform convergence studies only in space and only in time, and plot
 1510 the differences in the numerical solution or the error between successive pairs of spatial
 1511 and temporal resolutions to capture the true spatial and temporal orders of accuracy. The
 1512 second and third columns of Figures 14, 15, 18, and 19 can attest to this statement. The
 1513 slope s is reported at resolutions where asymptotic convergence is observed. For example,
 1514 for the coastal Kelvin wave test case discretized in space with a fourth-order DGSEM
 1515 and advanced with the second-order accurate time stepping methods RK2 and AB2, only
 1516 second-order accuracy is observed in the asymptotic regime. Similarly, as errors approach
 1517 machine precision, which often happens with high-order methods, these errors near machine
 1518 epsilon are excluded from the slope calculations. Finally, we note that when refining in
 1519 both space and time, the convergence often appears faster than the theoretical asymptotic
 1520 convergence rate—this occurs, for example, with the coastal Kelvin wave test. In these
 1521 examples, even though the time stepping methods RK3 and AB3 are third-order accurate,
 1522 the fourth-order accuracy is observed because the resolutions do not reach the asymptotic
 1523 regime, and the spatial error dominates at the chosen time step sizes. This underscores yet
 1524 another important reason for conducting the self-refinement convergence tests only in space
 1525 and only in time to verify the spatial and temporal orders of accuracy. It is worth noting that
 1526 for temporal refinement using TRiSK and fourth-order Runge-Kutta and Adams-Bashforth
 1527 methods, round-off errors overshadow the norm of the solution difference. As such, we
 1528 have excluded these particular convergence plots from our presentation. Finally, we obtain
 1529 expected convergence rates with the non-linear planetary and topographic Rossby waves
 1530 (test cases 3b and 4b), so we do not present these results here.

1531 7 Conclusion and Future Work

1532 We have designed a verification suite of shallow water test cases for ocean model
 1533 development. Each of these test cases verifies the implementation of a subset of terms
 1534 in the prognostic momentum and continuity equations e.g. the linear pressure gradient
 1535 term, the linear constant- or variable-coefficient Coriolis and bathymetry terms, and the
 1536 non-linear advection terms. The test cases constitute standard geophysical waves including
 1537 the non-dispersive coastal Kelvin wave, the high-frequency dispersive inertia-gravity wave,
 1538 the low-frequency dispersive planetary and topographic Rossby waves, the barotropic tide,
 1539 and a non-linear manufactured solution. Appendix A includes the non-dispersive equatorial
 1540 Kelvin wave and the dispersive equatorial Yanai, Rossby and inertia-gravity waves, as well
 1541 as four non-geophysical test cases: the plane Gaussian wave, the diffusion equation, the
 1542 advection-diffusion equation, and the viscous Burgers' equation.

1543 We have developed a shallow water solver in object-oriented Python (Bishnu, 2024a),
 1544 employing two types of spatial discretizations—TRiSK representing low-order mimetic finite
 1545 volume methods (FVMs), and DGSEM epitomizing high-order finite or spectral element
 1546 methods (SEMs)—and numerous time-stepping methods. It was used as a platform to
 1547 run the shallow water test cases, and conduct convergence studies for each test case with
 1548 refinement in both space and time, only in space, and only in time. The observed convergence
 1549 rates align with the theoretical predictions in Bishnu (2021).

1550 We utilized TRiSK and DGSEM, representing the finite volume and high-order spectral
 1551 element methods, based on their prevalence in operational ocean models. In our discussion,
 1552 we highlight key considerations associated with each spatial discretization technique. For

1553 example, we investigate the importance of conducting self-refinement convergence tests only
 1554 in space and only in time, noting that the rationale might differ between FVMs and SEMs.
 1555 We further delve into the nuances of numerical implementation, with certain details specific
 1556 to either FVMs or SEMs. Despite the differences between TRiSK and DGSEM, our study
 1557 underscores the robustness of our numerical approach in verifying the spatial and temporal
 1558 orders of accuracy across both discretization methods.

1559 In our analysis of numerical solutions, we discerned that the temporal evolution of
 1560 errors in both TRiSK and DGSEM closely mirrors the intrinsic physics of the system being
 1561 modeled. The DGSEM approach, characterized by its use of high-order polynomial basis
 1562 functions, is more prone to spurious oscillations near steep gradients or discontinuities, a
 1563 trait commonly dubbed as the “Gibbs phenomenon”. Employing Legendre-Gauss nodes in
 1564 conjunction with the local Lax Friedrichs (LLF) Riemann solver significantly alleviates these
 1565 oscillations. However, the LLF solver is not without its trade-offs, as it introduces its own
 1566 flavor of dissipative error. In coarser meshes with fewer elements to absorb these errors,
 1567 their impact becomes more pronounced, especially at element boundaries. Additionally,
 1568 DGSEM’s susceptibility to numerical dispersion errors is heightened in these coarser meshes
 1569 due to the physical phenomena being represented with less fidelity. In contrast, the TRiSK
 1570 scheme, with its inherent dissipation properties, effectively dampens both spurious oscillations
 1571 and dispersion errors. However, this comes at the expense of overall solution accuracy. In
 1572 fact, TRiSK’s error turns out to be several orders of magnitude larger than DGSEM’s at
 1573 comparable spatial resolution. This is despite the presence of the aforementioned numerical
 1574 artifacts in DGSEM, which become evident only upon close scrutiny.

1575 It is our hope that the exact solutions and numerical results presented here will be useful
 1576 to other developers of atmosphere and ocean dynamical cores. Shallow water equation
 1577 test cases may be applied to ocean layered primitive equation models with the vertical
 1578 advection and diffusion terms turned off, as well as the barotropic mode in split time-stepping
 1579 schemes. The suite was designed to include a progressive sequence of added complexity in the
 1580 terms tested, topography, and boundary conditions. Test cases with exact or manufactured
 1581 solutions can verify model functionality without resorting to high resolutions and a large
 1582 number time steps common in global simulations. Moreover, for convergence studies aimed
 1583 at verifying the spatial and temporal orders of accuracy, the simulation time can be further
 1584 reduced, leading to an even smaller number of time steps. Such attributes render these
 1585 test cases ideal for automated nightly regression testing and as a prerequisite for code pull
 1586 requests. Verification suites with thorough coverage of code functionality have proven to be
 1587 indispensable in our own development work. In E3SM, we have developed an automated
 1588 test harness called Polaris that creates the initial conditions, runs the ocean model, and then
 1589 reports the error and order of convergence for verification test cases (Asay-Davis & Begeman,
 1590 2024). Our ongoing and future work include designing further verification exercises with
 1591 complexity in between the barotropic equations and the primitive equations; stratification
 1592 and complex bathymetry; the ability to test both the barotropic and baroclinic components
 1593 separately, and the coupling between these modes.

1594 **Appendix A An Additional Suite of Test Cases**

1595 We present an additional suite of test cases with exact solutions, summarized in Table
 1596 A1. Test cases 1–6 in the main text encompass the largest variety of configurations—from
 1597 linear to non-linear, solid and periodic boundaries, flat and sloping bathymetries, and f - and
 1598 β -plane domains. Though test cases 7–14 expand the suite, they exhibit more repetition
 1599 in their configurations. The plane wave test case examines the most basic form of the linear
 1600 shallow water equations, excluding the Coriolis terms. The diffusion, advection-diffusion,
 1601 and viscous Burgers test cases do not offer solutions to the shallow water equations used
 1602 to simulate geophysical fluid dynamics. However, the advection-diffusion test case verifies
 1603 the implementation of the linear advection term, and in conjunction with the diffusion test
 1604 case, it verifies the implementation of the diffusion term ensuring the numerical stability

1605 of the non-linear shallow water equations. The viscous Burgers test case not only verifies
 1606 the implementations of the non-linear advection and diffusion terms, it also assesses the
 1607 resilience of numerical methods against problems with low regularity. Lastly, the equatorial
 1608 wave test cases (TC 10–13) may appear repetitive in their testing scope, but they hold merit
 1609 for pedagogical purposes, elucidating the dynamics and visualization of equatorial waves in
 1610 simplified configurations.

Table A1. Summary of test cases in Appendix A, continuing the case numbering from Table 1 in the main text. The last column refers to terms in the shallow water equations (6).

	Coriolis Parameter	Bottom Topography	Numerical PDE	Boundary Conditions	Terms Verified in Equation (6)
7. Plane Gaussian Wave	Zero (no Coriolis)	Flat Bottom	Linear, Homogeneous, Constant-Coefficient	Non-Periodic in x Non-Periodic in y	(5), (8)
8. Diffusion Eqn	Zero (no Coriolis)	Flat Bottom	Linear, Homogeneous, Constant-Coefficient	Periodic in x Periodic in y	(6)
9. Advection Diffusion Eqn	Zero (no Coriolis)	Flat Bottom	Linear, Homogeneous, Constant-Coefficient	Non-Periodic in x Non-Periodic in y	(6), (8)
10. Viscous Burgers Equation	Zero (no Coriolis)	Flat Bottom	Non-Linear, Homogeneous, Constant-Coefficient	Non-Periodic in x Non-Periodic in y	(1), (2), (6)
11. Equatorial Kelvin Wave	Linear in y (<i>beta-plane</i>)	Flat Bottom	Linear, Homogeneous, Variable-Coefficient	Periodic in x Non-Periodic in y	(4), (5), (8)
12. Equatorial Yanai Wave	Linear in y (<i>beta-plane</i>)	Flat Bottom	Linear, Homogeneous, Variable-Coefficient	Periodic in x Non-Periodic in y	(4), (5), (8)
13. Equatorial Rossby Wave	Linear in y (<i>beta-plane</i>)	Flat Bottom	Linear, Homogeneous, Variable-Coefficient	Periodic in x Non-Periodic in y	(4), (5), (8)
14. Equatorial Inertia Gravity Wave	Linear in y (<i>beta-plane</i>)	Flat Bottom	Linear, Homogeneous, Variable-Coefficient	Periodic in x Non-Periodic in y	(4), (5), (8)

1611 **A1 Plane Wave, Diffusion, Advection-Diffusion and Viscous Burgers Test**
 1612 **Cases**

1613 We offer a concise overview of the plane wave, diffusion, advection-diffusion, and viscous
 1614 Burgers test cases, accompanied by visual representations of the exact solutions' temporal
 1615 evolution.

1616 **A11 Test Case 7: Plane Wave**

1617 The plane wave is a solution of the linear homogeneous non-rotating shallow water
 1618 equations, obtained by specifying $f = 0$ in (10). It only tests the implementation of the
 1619 linear pressure gradient term in the momentum equations and the linear advection term in
 1620 the continuity equation. This is the first test case against which the linear shallow water
 1621 equations should be verified. In a domain with zonal and meridional extents denoted by L_x
 1622 and L_y , the exact solution for the plane wave can be characterized as a Gaussian, given by

$$\begin{bmatrix} u \\ v \\ \eta \end{bmatrix} = \begin{bmatrix} 1/k_x \\ 1/k_y \\ 1/g \end{bmatrix} \exp \left[- \left\{ \frac{k_x(x - x_0) + k_y(y - y_0) - ct}{\sqrt{2}R_0} \right\}^2 \right], \quad (\text{A1})$$

1623 where (x_0, y_0) are the initial coordinates of the Gaussian peak, (k_x, k_y) are the wavenumber
 1624 components, R_0 is the RMS width of the Gaussian peak, and $c = \sqrt{gH}$ is the propagation
 1625 speed of this plane Gaussian wave, equivalent to the shallow water gravity wave speed. For
 1626 the parameters, we have chosen $L_x = 10^6$ m, $x_0 = 0.25L_x$, $k_x = k_y = 1/\sqrt{2}$ m⁻¹, $g = 10$

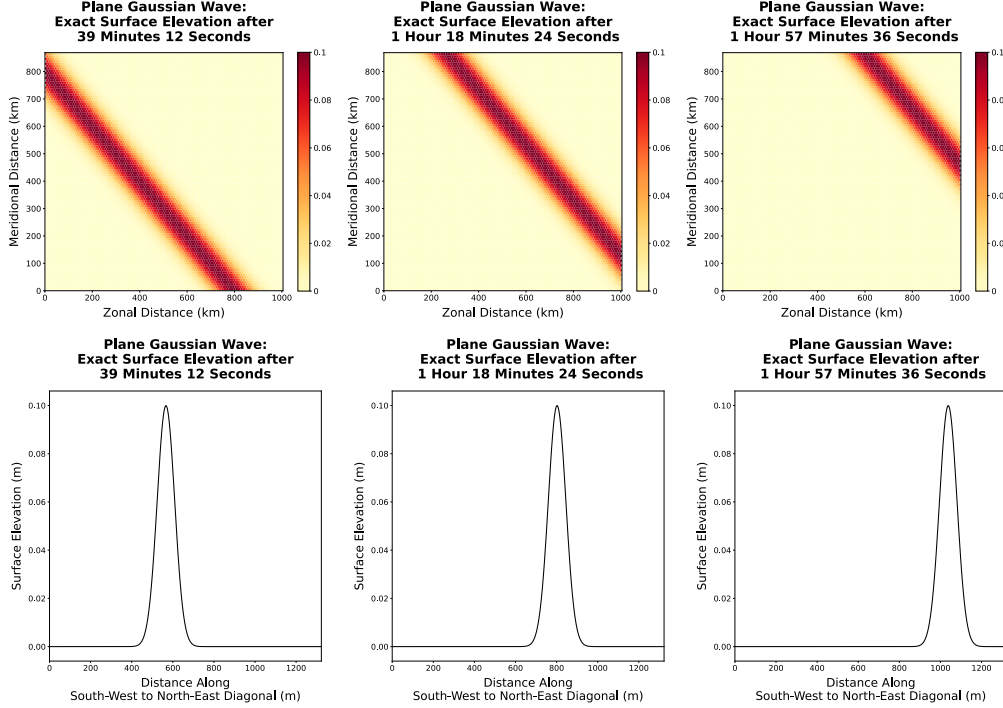


Figure A1. Time evolution of TC7, the plane Gaussian wave, showing the exact surface elevation (first row), and cross-section of the exact surface elevation along the south-west to north-east diagonal (second row).

1627 m s^{-2} , $H = 1000 \text{ m}$ (yielding $c = 100 \text{ m s}^{-1}$), and $R_0 = w/(2\sqrt{2\ln 2})$, where $w = 10^5 \text{ m}$
 1628 denotes the full width at half maximum. For the spectral element mesh, $y_0 = x_0$, and for
 1629 the MPAS-Ocean mesh, $y_0 = \sqrt{3}/2x_0$. Figure A1 depicts the time evolution of the surface
 1630 elevation of this plane wave in the entire domain (first row) and along the south-west to
 1631 north-east diagonal (second row). The error patterns of the non-dispersive Kelvin wave,
 1632 depicted in Figure 10 of the main paper, resemble this plane wave, as they all travel at the
 1633 shallow water gravity wave speed.

1634 **A12 Test Case 8: Diffusion Equation**

1635 The heat or diffusion equation is a fundamental equation in the study of heat transfer
 1636 and diffusion processes. It describes how a quantity, such as temperature or concentration of
 1637 a substance, spreads out over time inside a specified region. In two dimensions, the equation
 1638 is expressed as

$$\varphi_t = \nu \nabla^2 \varphi, \tag{A2}$$

1639 where φ represents the diffusing quantity, and ν is the diffusion coefficient, a measure
 1640 of the rate at which diffusion occurs. Based on Fick's laws of diffusion, (A2) assumes a
 1641 homogeneous and isotropic medium, meaning the properties of the medium do not change
 1642 with direction or position. It essentially states that the rate of change of the scalar field,
 1643 φ , at any point in space is proportional to the curvature of φ at that point. This reflects
 1644 the physical principle that diffusion acts to smooth out variations in the scalar field over
 1645 time. Mathematically, (A2) is an example of a parabolic partial differential equation,
 1646 and is derived under the assumption of a constant diffusion coefficient and the absence
 1647 of any sources or sinks within the domain. Standard texts on partial differential equations
 1648 and numerical analysis, including works by Strauss (2007), J. D. Logan (2014), Farlow

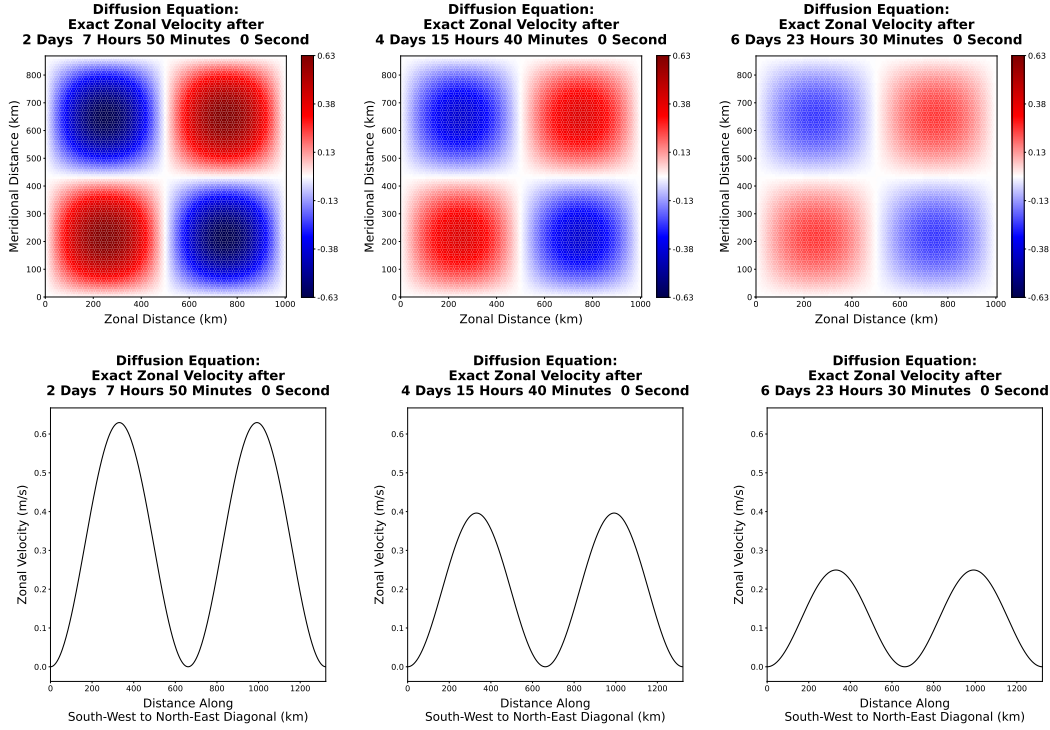


Figure A2. Same as Figure A1 but for TC8, the diffusion equation, showing the exact solution (first row), and cross-section of the exact solution along the south-west to north-east diagonal (second row).

1649 (1993), and Haberman (1998), offer in-depth explorations of this equation. Solving the
 1650 diffusion equation while employing the spatial discretization of an ocean model verifies the
 1651 implementation of the Laplacian operator. In our numerical simulations, we employ the
 1652 exact solution

$$\varphi(x, y, t) = \sin(k_x x) \sin(k_y y) e^{-\kappa t}, \quad (\text{A3})$$

1653 to set the initial and boundary conditions. The diffusivity, $\kappa = \nu (k_x^2 + k_y^2)$, represents the
 1654 rate and pattern of diffusion, factoring in the spatial variability of the system. In a domain
 1655 with a zonal extent of $L_x = 10^6$ m, key parameters include $k_x = 2\pi/L_x$, $k_y = 2\pi/L_y$, and
 1656 $\nu = 25000 \text{ m}^2 \text{ s}^{-1}$. The exact solution's visualization, depicted in Figure A2, showcases
 1657 the diffusion phenomenon across the entire domain (first row) and along the south-west to
 1658 north-east diagonal (second row).

1659 *A13 Test Case 9: Advection-Diffusion Equation*

1660 The advection-diffusion equation models the combined effect of advection and diffusion
 1661 on a scalar field, φ , such as concentration of a substance or temperature. This equation plays
 1662 a pivotal role in fields including fluid dynamics, heat transfer, and environmental sciences.
 1663 Mathematically, the equation is formulated as

$$\varphi_t + \mathbf{u}_0 \cdot \nabla \varphi \equiv \varphi_t + \nabla \cdot (\varphi \mathbf{u}_0) = \nu \nabla^2 \varphi. \quad (\text{A4})$$

1664 Here, φ is the scalar quantity of interest, $\mathbf{u}_0 = u_0 \mathbf{i} + v_0 \mathbf{j}$ is the velocity field causing
 1665 advection, and ν is the diffusion coefficient. Comprehensive derivations and solutions of the
 1666 advection-diffusion equation can be gleaned from standard PDE and numerical analysis
 1667 texts, such as those by Strauss (2007), Smith (1985), Donea and Huerta (2003), and

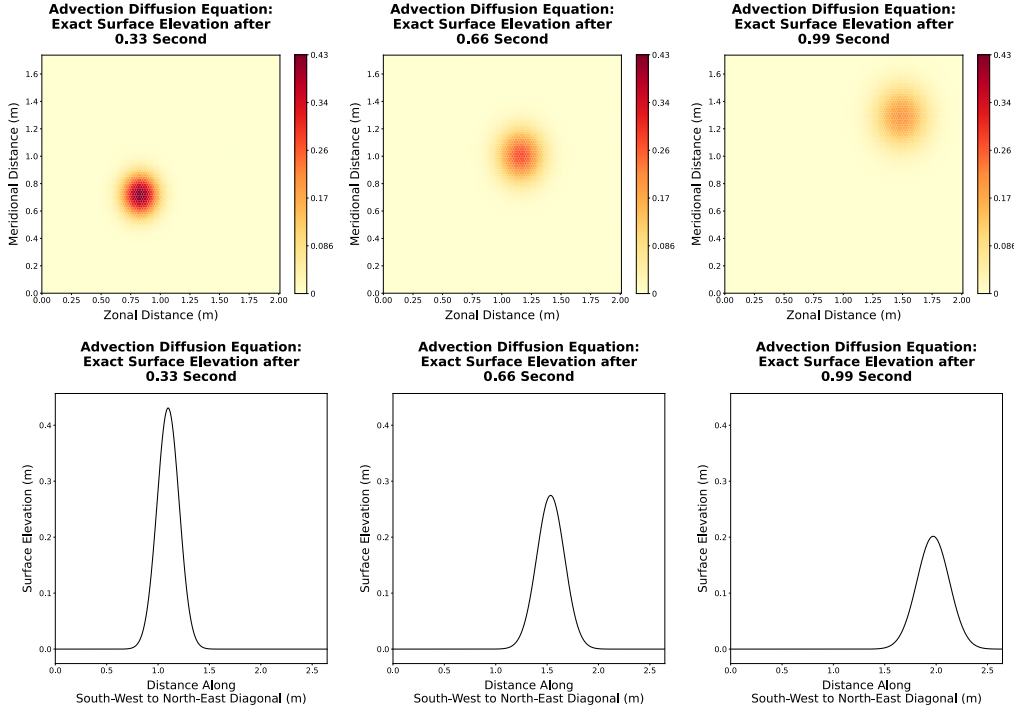


Figure A3. Same as Figure A1 but for TC9, the advection-diffusion equation, showing the exact solution (first row), and cross-section of the exact solution along the south-west to north-east diagonal (second row).

1668 D. A. Kopriva (2009). When the advection-diffusion equation is solved using the spatial
 1669 discretization of an ocean model, the implementation of the divergence and Laplacian
 1670 operators can be verified. In our numerical simulations, we employ the exact solution

$$\varphi(x, y, t) = \frac{1}{4t + 1} \exp \left[-\frac{\left\{ (x - x_0 - u_0 t)^2 + (y - y_0 - v_0 t)^2 \right\}}{\nu(4t + 1)} \right], \quad (\text{A5})$$

1671 to specify the initial and boundary conditions. This solution depicts a two-dimensional
 1672 Gaussian patch with a time-dependent amplitude of $1/(4t + 1)$ and a radial RMS width of
 1673 $\sqrt{\nu(4t + 1)}/2$. This patch is advected by the velocity \mathbf{u}_0 while undergoing diffusion at a rate
 1674 of ν . The Gaussian’s peak is initially located at coordinates (x_0, y_0) . In a domain with a
 1675 zonal extent of $L_x = 2$ m, the parameters are chosen as $x_0 = 0.25L_x = 0.5$ m, $u_0 = 1$ m s⁻¹,
 1676 and $\nu = 0.01$ m² s⁻¹. For the spectral element mesh, the parameters y_0 , and v_0 mirror their
 1677 zonal counterparts. In contrast, on the MPAS-Ocean mesh, these parameters are scaled by
 1678 a factor of $\sqrt{3}/2$ relative to their zonal values. Figure A3 illustrates the exact solution of
 1679 the advection-diffusion equation with the aforementioned parameters, in the entire domain
 1680 (first row) and along the south-west to north-east diagonal (second row).

1681 *A14 Test Case 10: Viscous Burgers’ Equation*

1682 The study of hyperbolic PDEs such as the Burgers’ equation requires understanding
 1683 the notion of “characteristics”. In the context of the simpler linear advection equation,
 1684 $u_t + au_x = 0$, the solution is given by $u(x, t) = u_0(x - at)$, where $u_0(x)$ represents the
 1685 initial condition and a is the advection speed. For this equation, $x - at = c$ (where c takes
 1686 different values) represents straight lines in the $x - t$ plane called characteristics. Along
 1687 these characteristics, the solution remains unchanged, effectively signifying that information

1688 propagates without alteration. Transitioning to the inviscid Burgers' equation, the situation
 1689 becomes non-linear and significantly more complex. Here, the equation reads $u_t + uu_x = 0$
 1690 or $u_t + (f(u))_x = 0$, where $f(u) = u^2/2$. A crucial difference is noticed: while in the
 1691 linear advection equation, the advection speed is constant, in the Burgers' equation, it is
 1692 dependent on the solution magnitude u itself. This means the characteristics are determined
 1693 by the local value of the solution, causing them to curve in the $x-t$ plane rather than being
 1694 straight lines. As the local advection speed u varies across the domain, characteristics either
 1695 converge or diverge.

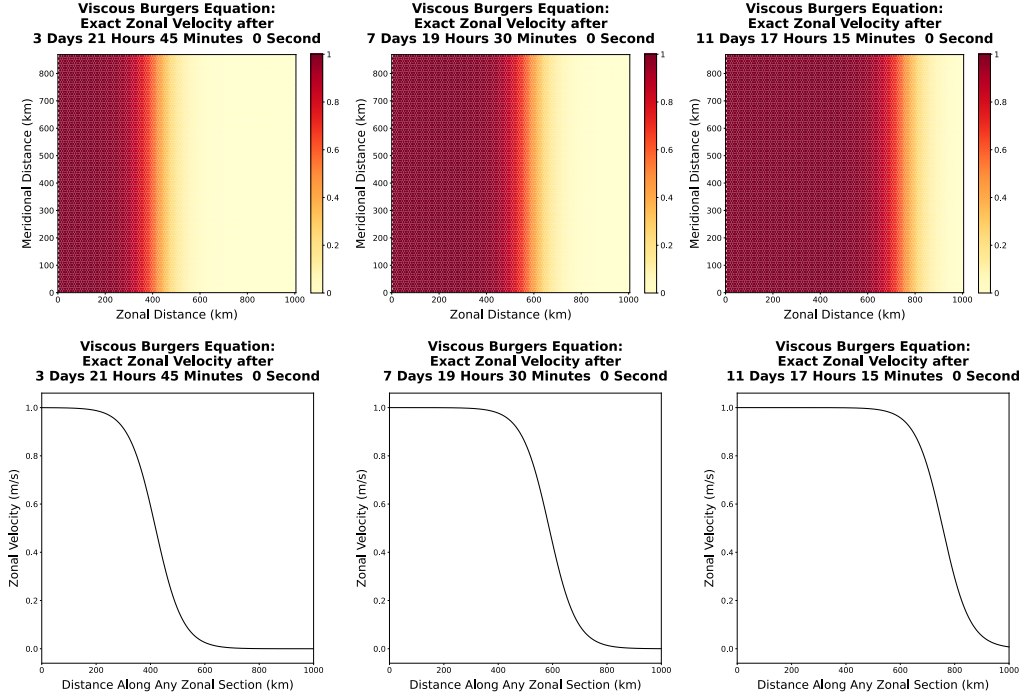


Figure A4. Same as Figure A1 but for TC10, the viscous Burgers' shock wave, showing the exact solution (first row) and cross-section of the exact solution (second row).

1696 The Riemann problem, taken as an example, features a step-like initial condition:

$$u_0(x) = \begin{cases} u_l & \text{if } x < 0, \\ u_r & \text{if } x \geq 0, \end{cases} \quad (\text{A6})$$

1697 where u_l and u_r are constants. Due to the step-like variation, different advection speeds,
 1698 u_l and u_r respectively, are possessed by the left and right sides. Characteristics are either
 1699 caused to converge (if $u_l > u_r$) resulting in a shock wave, or to diverge (if $u_l < u_r$) leading
 1700 to a rarefaction wave. With a smooth initial condition like a Gaussian $u(x, 0) = \exp(-x^2)$,
 1701 the solution is continuously varying, and so is the local advection speed. Initially, the
 1702 solution remains single-valued for every x . However, due to the higher magnitude (and thus
 1703 higher advection speed) at the Gaussian's peak, it starts overtaking its leading edge, causing
 1704 characteristics to converge. A triple-valued solution at certain x values is encountered,
 1705 marking the breaking time. Replacing the multi-valued region with a discontinuity by the
 1706 equal area rule ensures the conservation of the integral of u and sets the shock's position.
 1707 Meanwhile, at the trailing (left) edge of the Gaussian bump, the characteristics diverge due
 1708 to a lower advection speed, causing a rarefaction wave to form.

1709 When characteristics converge leading to a shock formation, numerically the solution
 1710 can become multi-valued in standard discretization schemes. This multi-valuedness is not
 1711 physically realizable and leads to ambiguity. Numerical methods typically are not designed
 1712 to handle multi-valued solutions directly. Instead, when faced with a choice among several
 1713 possible values, the method may inadvertently pick one, leading to an artificially steep
 1714 gradient. These steep gradients can induce numerical instabilities, particularly in explicit
 1715 time-stepping schemes, where high gradients can result in time step restrictions (due to
 1716 the CFL condition) or even solution blow-up. In the case of a rarefaction wave, the
 1717 characteristics spread apart. Numerically, when modeling a rarefaction wave, the solution
 1718 remains single-valued and smoother compared to a shock. There is not the same challenge of
 1719 handling multi-valued solutions. However, if not captured accurately, numerical diffusion, an
 1720 artifact of many discretization schemes, can overly smooth the rarefaction, making it wider
 1721 and less pronounced than it should be. This is a common issue, especially in first-order
 1722 numerical schemes.

1723 We now transition to the viscous Burgers' equation, $u_t + uu_x = \nu u_{xx}$, where ν represents
 1724 the viscosity or diffusion coefficient. The introduction of this viscous term plays a pivotal
 1725 role in smoothing out the discontinuities found in the inviscid case. For instance, in the
 1726 Riemann problem, the introduction of viscosity transforms what would be a shock wave in
 1727 the inviscid case into a smooth transition in space and time, given by

$$u(x, t) = s - \frac{u_l - u_r}{2} \tanh \left\{ \frac{(x - x_0 - st)(u_l - u_r)}{4\nu} \right\}, \quad (\text{A7})$$

1728 where $s = (u_l + u_r)/2$ represents the shock speed, and x_0 denotes the location of the initial
 1729 discontinuity or transition in the solution. In the context of the inviscid Burgers' equation,
 1730 s can be derived using the Rankine-Hugoniot jump condition:

$$s = \frac{\text{jump in } f(u)}{\text{jump in } u} = \frac{f(u_l) - f(u_r)}{u_l - u_r} = \frac{u_l^2 - u_r^2}{2(u_l - u_r)} = \frac{u_l + u_r}{2}. \quad (\text{A8})$$

1731 As $x \rightarrow +\infty$, the hyperbolic tangent function asymptotically approaches 1, ensuring that
 1732 the solution tends to u_r . Conversely, as $x \rightarrow -\infty$, the hyperbolic tangent function gravitates
 1733 towards -1 , and hence the solution aligns with u_l . The term $(x - x_0 - st)(u_l - u_r)$ in the
 1734 numerator ensures the solution progresses with the appropriate shock speed and correctly
 1735 accounts for the position and magnitude of the initial discontinuity. When the viscosity ν
 1736 is allowed to approach zero, the hyperbolic tangent function becomes increasingly sharp.
 1737 In this limiting scenario, the solution of the viscous Burgers' equation converges to the
 1738 step function solution that characterizes the inviscid Riemann problem, illustrating the
 1739 connection between the viscous and inviscid formulations.

1740 Using the viscous Burgers' equation as a verification test for ocean models can be
 1741 quite advantageous. Ocean models inherently do not encounter shock waves due to viscous
 1742 terms and numerical diffusion. The viscous Burgers' equation allows these models to verify
 1743 both their non-linear advection and viscous terms. Moreover, by adjusting the viscosity
 1744 parameter, we can modulate the solution's regularity, allowing us to closely approach a
 1745 discontinuous step function and thus robustly test our numerical methods.

1746 Figure A4 displays the exact solution of the viscous Burgers' equation in the entire
 1747 domain (first row) and along any zonal section (second row). It is uniform in the meridional
 1748 direction. In case of the TRiSK discretization, the normal velocity is the prognostic quantity
 1749 of interest. So, we do not lose any generality by using a velocity field with zero meridional
 1750 component as in this instance. Key parameters include $L_x = 10^6$ m, $x_0 = L_x/4 = 2.5 \times 10^5$
 1751 m, $u_l = 1$ m s⁻¹, $u_r = 0$, $s = (u_l + u_r)/2 = 0.5$ m s⁻¹, and $\nu = 2.5 \times 10^4$ m² s⁻¹.

1752 **A2 Equatorial Waves**

1753 Along the equator, the latitude $\phi_0 = 0$, and the Coriolis parameter $f_0 = 2\Omega \sin \phi_0$
 1754 vanishes. So, the equator is a dynamically special region. Therefore, in the vicinity of the

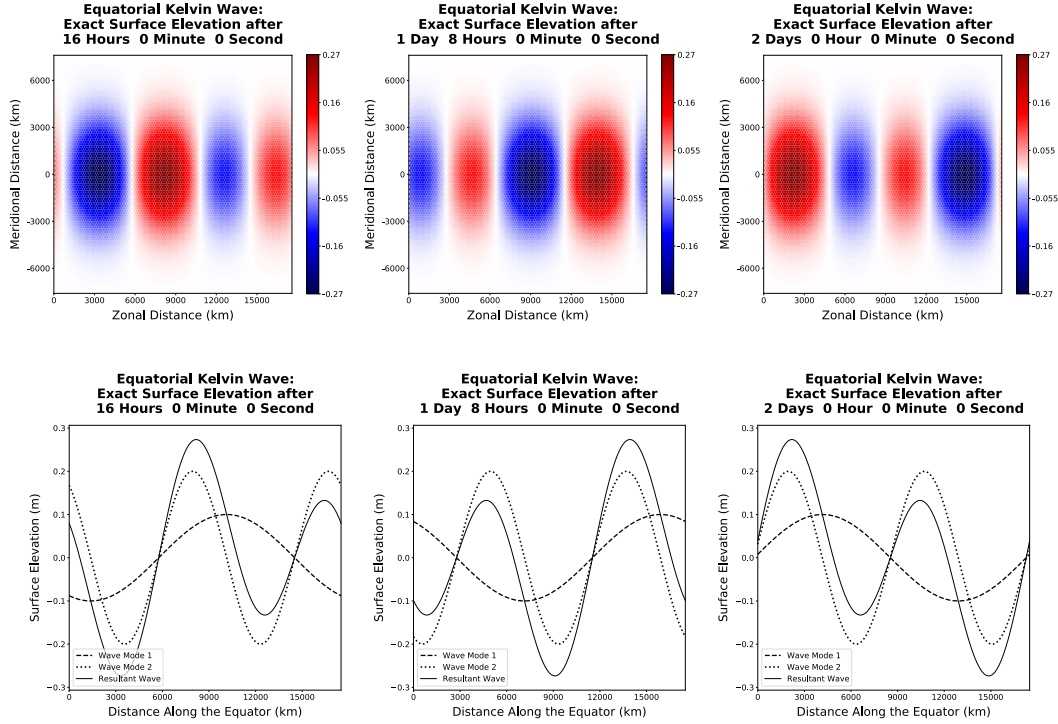


Figure A5. Time evolution of the TC11, the non-dispersive equatorial Kelvin wave, showing the exact surface elevation (first row) and cross-section of the exact surface elevation (second row).

1755 equator, certain geophysical waves develop unusually strong signals and contribute to the
 1756 generation of the Quasi-Biennial Oscillation (QBO) in the atmosphere (Hell, 2020; Baldwin
 1757 et al., 2001) and the El Niño Southern Oscillation (ENSO) phenomenon in the ocean and
 1758 atmosphere (Clarke, 2008; Sarachik & Cane, 2010; Philander et al., 1989).

1759 The equatorial Kelvin, Yanai, Rossby, and inertia-gravity waves are solutions of the
 1760 rotating shallow water equations

$$u_t - \beta_0 y v = -g \eta_x, \quad (\text{A9a})$$

$$v_t + \beta_0 y u = -g \eta_y, \quad (\text{A9b})$$

$$\eta_t + H(u_x + v_y) = 0, \quad (\text{A9c})$$

1761 where u and v are the zonal and meridional velocities, η is the surface elevation, H is the
 1762 mean depth of the ocean with a flat bottom, β_0 is the first-order meridional gradient of the
 1763 Coriolis parameter, and g is the acceleration due to gravity. Equation (A9) is obtained by
 1764 replacing f with $\beta_0 y$ in equation (18) of the main paper. Detailed derivations of equatorial
 1765 wave solutions are found in textbooks specializing in equatorial dynamics (Clarke, 2008)
 1766 and many geophysical fluid dynamics textbooks (Vallis, 2017; Cushman-Roisin & Beckers,
 1767 2011).

1768 **A21 Test Case 11: Equatorial Kelvin Wave**

1769 The equatorial Kelvin wave is a long gravity wave trapped along the equator with decay
 1770 scale $\sqrt{2}R_{eq} = (2c/\beta_0)^{1/2}$, where $c = \sqrt{gH}$ is the shallow water gravity wave speed, and
 1771 R_{eq} is the equatorial Rossby radius of deformation. The equatorial Kelvin wave has zero
 1772 meridional velocity, and travels eastward at speed c . It is non-dispersive and assumes a

1773 solution of the form

$$\eta = HG(x - ct) \exp\left(-\frac{1}{2} \left(\frac{y}{R_{eq}}\right)^2\right), \quad (\text{A10})$$

$$u = cG(x - ct) \exp\left(-\frac{1}{2} \left(\frac{y}{R_{eq}}\right)^2\right). \quad (\text{A11})$$

1774 In our numerical simulations, we specify

$$G(x - ct) = \hat{\eta} \sin(k(x - ct)) = \hat{\eta} \sin(kx - \omega t) = \hat{\eta} \text{Im}\left(e^{i(kx - \omega t)}\right), \quad (\text{A12})$$

1775 where $\hat{\eta}$ is the amplitude, and the phase speed $\omega/k = c$ is a constant.

1776 Figure A5 displays the time evolution of the equatorial Kelvin wave's surface elevation
 1777 across the entire domain (first row) with zonal extent $L_x = 1.75 \times 10^7$ m, and along
 1778 the equator (second row). Similar to our simulations of the coastal Kelvin wave and the
 1779 inertia-gravity wave in the main paper, we specify the exact solutions to be a superposition
 1780 of two wave components, where the second component possesses twice the amplitude and
 1781 wavenumber of the first. Mathematically, $\hat{\eta}^{(2)} = 2\hat{\eta}^{(1)}$ and $k^{(2)} = 2k^{(1)}$, where $\hat{\eta}^{(1)} = 10^{-4}$
 1782 m and $k^{(1)} = 2\pi/L_x$. Being non-dispersive in nature, both components, as well as the
 1783 resultant wave, propagate at an identical phase speed, thereby preserving the initial profile
 1784 of the resultant wave.

1785 ***A22 Test Cases 12, 13, and 14: Equatorial Yanai, Rossby, and Inertia-Gravity Waves***

1787 The equatorial Yanai, Rossby and inertia-gravity waves can be obtained from the
 1788 non-dimensional form of (A9),

$$u'_{t'} - y'v' = -\eta'_{x'}, \quad (\text{A13a})$$

$$v'_{t'} + y'u' = -\eta'_{y'}, \quad (\text{A13b})$$

$$\eta'_{t'} + u'_{x'} + v'_{y'} = 0, \quad (\text{A13c})$$

1789 where $u = cu'$, $v = cv'$, $\eta = H\eta'$, $x = \sqrt{c/\beta_0}x'$, $y = \sqrt{c/\beta_0}y'$, and $t = 1/\sqrt{\beta_0}ct'$.
 1790 Dropping the primes for notational convenience, the non-dimensional meridional velocity
 1791 of the dispersive equatorial Yanai, Rossby and inertia-gravity waves can be expressed in
 1792 modal form as

$$v = \text{Re}\left(e^{i(kx - \omega t)}\psi_m(y)\right) = \cos(kx - \omega t)\psi_m(y), \quad (\text{A14})$$

1793 where the Hermite function $\psi_m(y)$ is

$$\psi_m(y) = \frac{e^{-y^2/2}H_m(y)}{\sqrt{2^m m! \sqrt{\pi}}}, \quad (\text{A15})$$

1794 with $H_m(y)$ being the m^{th} -order Hermite polynomial. Since $H_m(y)$ is an odd function of y
 1795 for odd m and an even function of y for even m , so is $\psi_m(y)$. The Hermite function $\psi(y)$
 1796 satisfies

$$\frac{d^2\psi_m}{dy^2} + \left(\omega^2 - k^2 - \frac{k}{\omega} - y^2\right)\psi \equiv \frac{d^2\psi_m}{dy^2} + (2m + 1 - y^2)\psi = 0, \quad m = 0, 1, \dots, \quad (\text{A16})$$

1797 with the non-dimensional dispersion relation being

$$k^2 + \frac{k}{\omega} - \omega^2 + (2m + 1) = 0, \quad m = 0, 1, \dots \quad (\text{A17})$$

1798 From (A16), it can be seen that $\psi_m(y)$ is oscillatory for $|y| < \sqrt{2m + 1}$ and monotonically
 1799 decaying for $|y| > \sqrt{2m + 1}$. Since the nature of $\psi_m(y)$ changes at $y = \sqrt{2m + 1}$, it is
 1800 referred to as the turning latitude for mode m . Solving the quadratic equation (A17) in k ,

$$k = -\frac{1}{2\omega} \pm \sqrt{\omega^2 + \frac{1}{4\omega^2} - (2m + 1)}. \quad (\text{A18})$$

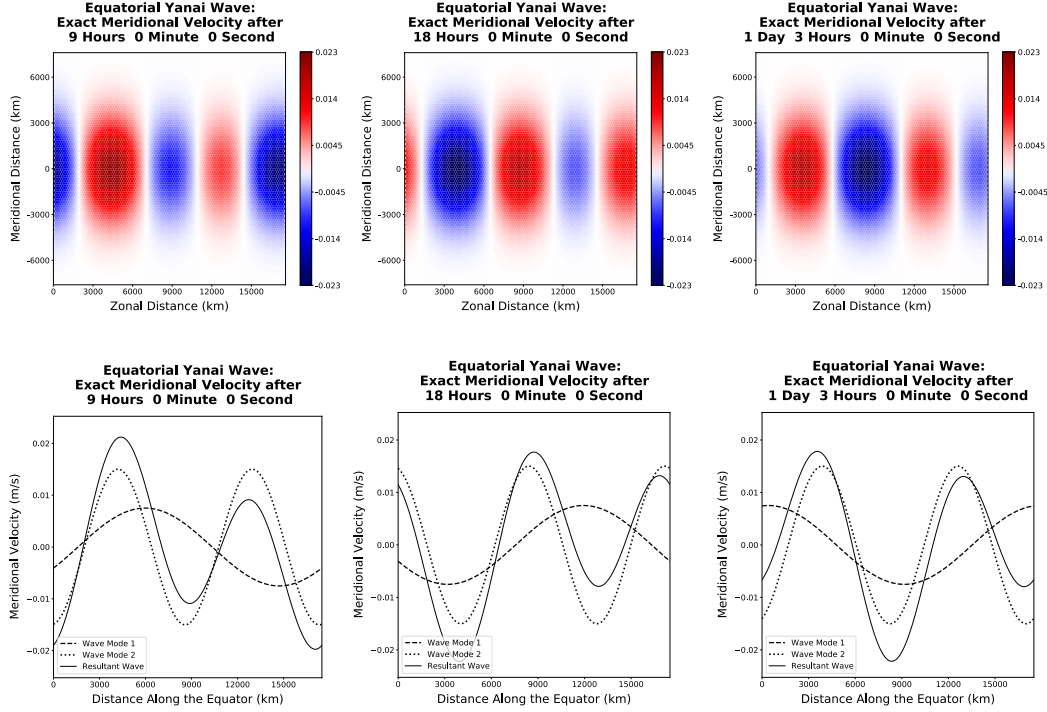


Figure A6. Time evolution of the TC12, the dispersive equatorial Yanai wave, showing the exact meridional velocity (first row) and cross-section of the exact meridional velocity along the equator (second row).

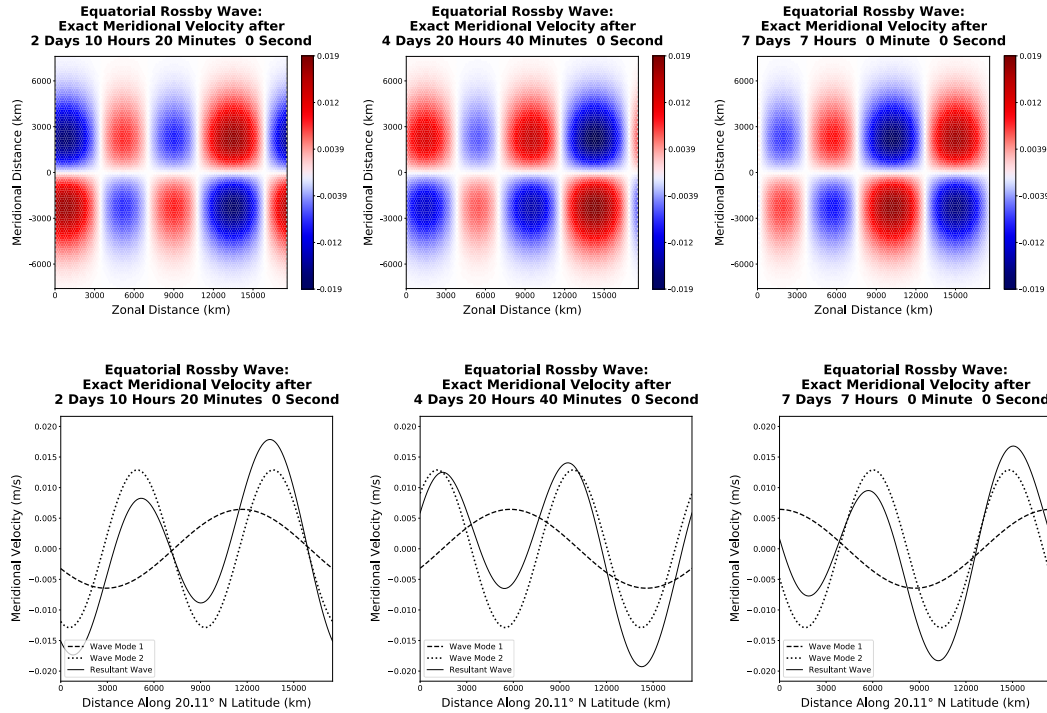


Figure A7. Time evolution of the TC13, the dispersive equatorial Rossby wave, showing the exact meridional velocity (first row) and cross-section of the exact meridional velocity along the 20.11°N latitude with maximum magnitude of the Hermite function $\psi_1(y)$ (second row).

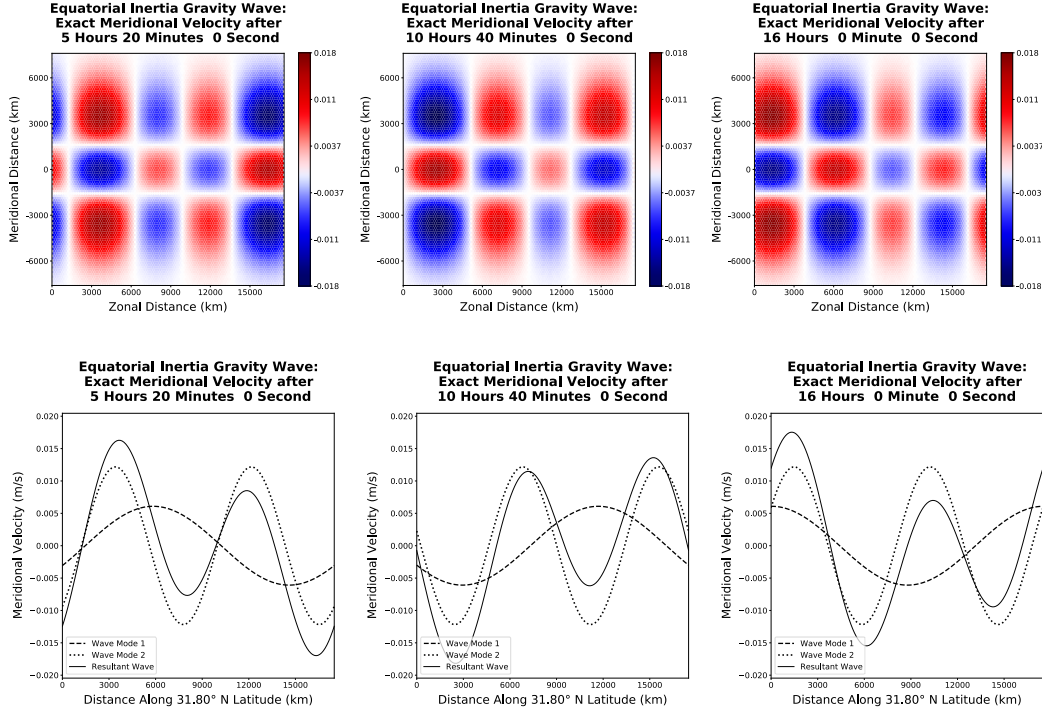


Figure A8. Time evolution of the TC14, the dispersive equatorial inertia-gravity wave, showing the exact meridional velocity (first row) and cross-section of the exact meridional velocity along the 31.80°N latitude with maximum magnitude of the Hermite function $\psi_2(y)$ (second row).

1801 When $m = 0$, the roots are $k = \omega - 1/\omega$ and $k = -\omega$, both of which are real. The
 1802 root $k = -\omega$ corresponds to a westward propagating Kelvin wave with unbounded velocity
 1803 at large distances from the equator, and is therefore not a viable solution. The other root
 1804 $k = \omega - 1/\omega$ gives rise to a Yanai or ‘mixed’ Rossby gravity wave with meridional velocity

$$v = \exp\left(i\left(\omega - \frac{1}{\omega}\right)x - \omega t\right)\psi_0(y). \quad (\text{A19})$$

1805 When the discriminant $\omega^2 + 1/(4\omega^2) - (2m + 1) > 0$ and $m \geq 1$, both roots of (A18)
 1806 are real and result in acceptable wave fields. But depending on the magnitude of ω , these
 1807 waves can belong to one of two categories: low-frequency Rossby waves for small ω , or
 1808 high-frequency inertia-gravity waves for large ω .

1809 Equation (A18) expresses the wave number, k , in terms of the angular velocity, ω .
 1810 Alternatively, the angular velocity, ω , corresponding to a particular wave number, k , can be
 1811 determined by solving the non-linear equation

$$\mathcal{F}(\omega) \equiv \omega^3 - (k^2 + 2m + 1)\omega - k = 0, \quad (\text{A20})$$

1812 which is a variant of (A17). We use the Newton-Raphson method to solve (A20), and specify
 1813 the magnitude of the initial guess for ω to be close to zero for the low-frequency equatorial
 1814 Rossby wave and greater than one for the high-frequency equatorial inertia-gravity wave.

1815

The non-dimensional zonal velocity and surface elevation are

$$u = \operatorname{Re} \left(\frac{k \frac{d\psi_m}{dy} - \omega y \psi_m}{k^2 - \omega^2} i e^{i(kx - \omega t)} \right) = \frac{k \frac{d\psi_m}{dy} - \omega y \psi_m}{\omega^2 - k^2} \sin(kx - \omega t), \quad (\text{A21})$$

$$\eta = \operatorname{Re} \left(\frac{\omega \frac{d\psi_m}{dy} - ky \psi_m}{k^2 - \omega^2} i e^{i(kx - \omega t)} \right) = \frac{\omega \frac{d\psi_m}{dy} - ky \psi_m}{\omega^2 - k^2} \sin(kx - \omega t). \quad (\text{A22})$$

1816

1817

1818

1819

1820

1821

1822

1823

1824

1825

1826

1827

1828

1829

1830

1831

1832

1833

1834

Figures A6 through A8 showcase the meridional velocity of the equatorial Yanai, Rossby, and inertia-gravity waves. As with previous demonstrations, we define the exact solutions for these equatorial waves as a combination of two wave components, wherein the second component possesses twice the amplitude and wavenumber of the first. Mathematically, $\hat{\eta}^{(2)} = 2\hat{\eta}^{(1)}$ and $k^{(2)} = 2k^{(1)}$, where $\hat{\eta}^{(1)} = 10^{-4}$ m, $k^{(1)} = 2\pi/L_x$, and $L_x = 1.75 \times 10^7$ m. The first row of these figures portrays the equatorial wave across the entire domain, while the second row focuses on a segment of the resultant wave solution and its components along the latitude characterized by the peak magnitude of the Hermite function, $\psi_m(y)$. Due to the dispersive nature, these components propagate at different phase speeds causing the resultant wave profile to alter over time. For the equatorial Yanai wave (Figure A6) and inertia-gravity wave (Figure A8), we specify $m = 0$ and $m = 2$, so that the Hermite functions $\psi_0(y)$ and $\psi_2(y)$ are even, and therefore the solution is symmetric across the equator. For the equatorial Rossby wave (Figure A7), we specify $m = 1$, so that the Hermite function $\psi_1(y)$ is odd, and therefore the solution is antisymmetric across the equator. Moreover, $\psi_0(y)$, $\psi_1(y)$, and $\psi_2(y)$ attain their maximum magnitudes at $y = 0$, $y = \pm 1$, and $y = \pm\sqrt{2.5}$. After multiplying by the length scale $\sqrt{c/\beta_0}$, and dividing by the radius of the Earth, these non-dimensional values of y correspond to the 0° latitude or the equator (second row of Figure A6), the 20.11°N and S latitudes (second row of Figure A7), and the 31.80°N and S latitudes (second row of Figure A8).

1835

A3 Numerical Results

1836

1837

1838

1839

1840

We begin this section by addressing the time step limitations inherent to the numerical simulation of the diffusion, advection-diffusion and viscous Burgers' equations. The parabolic nature of these equations, resulting from the diffusion term, necessitates a more restrictive time step. Drawing from the Von Neumann stability analysis of the linear diffusion equation, we define the diffusive time step on a two-dimensional spatial domain as

$$\Delta t_{\text{diffusive}} = \begin{cases} \frac{1}{2\nu \left(\frac{1}{\Delta x^2} + \frac{1}{\Delta y^2} \right)} & \text{for TRiSK,} \\ \frac{1}{2\nu \left(\frac{P_x^2}{\Delta x^2} + \frac{P_y^2}{\Delta y^2} \right)} & \text{for DGSEM.} \end{cases} \quad (\text{A23})$$

1841

1842

1843

1844

Here, ν symbolizes the diffusion coefficient, while Δx and Δy represent the widths of the cell (or element). On a uniform TRiSK mesh with hexagonal cells, we can set $\Delta y = \sqrt{3}/2\Delta x$. In the context of DGSEM, P_x and P_y signify the polynomial orders in the two horizontal directions. Based on (59)–(61) in the main paper, we define the advective time step to be

$$\Delta t_{\text{advective}} = \begin{cases} \frac{C}{\frac{c_x}{\Delta x} + \frac{c_y}{\Delta y}} & \text{for TRiSK,} \\ \frac{C}{\frac{c_x P_x^2}{\Delta x} + \frac{c_y P_y^2}{\Delta y}} & \text{for DGSEM.} \end{cases} \quad (\text{A24})$$

1845

1846

1847

In the equations above, C represents the Courant number. For the advection-diffusion equation, we specify $c_x = u_0$ and $c_y = v_0$. Similarly, for the viscous Burgers' equation, we set $c_x = \max(|u_l|, |u_r|)$ and $c_y = 0$. The actual time step is specified as $\Delta t = \Delta t_{\text{diffusive}}$ for

1848 the diffusion equation and $\Delta t = \min(\Delta t_{\text{advective}}, \Delta t_{\text{diffusive}})$ for the advection-diffusion and
 1849 viscous Burgers' equations.

1850 We present the numerical results, showcasing error plots and their temporal evolution.
 1851 Figures A9 to A12 display the surface elevation errors for the plane Gaussian wave, the
 1852 diffusion and advection-diffusion equation solutions, and the zonal velocity error of the
 1853 viscous Burgers shock wave. Subsequently, Figures A13 to A16 depict the temporal evolution
 1854 of the surface elevation error of the equatorial Kelvin wave, as well as the meridional velocity
 1855 error for equatorial Yanai, Rossby, and inertia-gravity waves. The zonal extent of the
 1856 rectangular domain for each test case is specified as follows: $L_x = 10^6$ m, 10^6 m, 2 m, 10^6 m,
 1857 and 1.75×10^7 m for the plane Gaussian wave, the diffusion equation, the advection-diffusion
 1858 equation, the viscous Burgers' equation, and the equatorial waves respectively. As for the
 1859 meridional extent, it is defined by $L_y = \sqrt{3}/2L_x$ for TRiSK, and by $L_y = L_x$ for DGSEM. In
 1860 each horizontal direction, the planar hexagonal TRiSK mesh comprises $N = 100$ cells, and
 1861 the spectral element mesh consists of $N = 5$ elements. The distance between the hexagonal
 1862 cell centers of the TRiSK mesh, given by $\Delta x = L_x/N$, represents the zonal cell width,
 1863 and $\Delta y = \sqrt{3}/2\Delta x$ provides a measure for the meridional cell width. Meanwhile, for the
 1864 spectral element mesh, the side lengths are equal in both directions: $\Delta x = L_x/N$. The
 1865 smallest grid spacings near the element boundaries approximate to $\Delta x/P^2$, with $P = 10$
 1866 indicating the order of the polynomial basis functions and the spatial order of accuracy of
 1867 our DGSEM. For all test cases, we target an advective Courant number close to 0.5. For
 1868 the diffusion equation, we choose the diffusive time step, and for the advection-diffusion
 1869 and viscous Burgers test cases, we select the minimum between the advective and diffusive
 1870 time steps, as elaborated in the preceding paragraph. When modeled with TRiSK, this
 1871 leads to time step sizes of $\Delta t = 16$ s, 750 s, 5×10^{-3} s, 750 s, 900 s, 450 s, 1200 s, and
 1872 300 s for the plane Gaussian wave, the diffusion equation, the advection-diffusion equation,
 1873 the viscous Burgers' equation, and the equatorial Kelvin, Yanai, Rossby, and inertia-gravity
 1874 waves respectively. With DGSEM, the respective time steps for these cases are set at 3.5 s,
 1875 40 s, 4×10^{-4} s, 30 s, 180 s, 90 s, 240 s, and 60 s.

1876 The first row of Figures A9—A16 demonstrates the error yielded by the second-order
 1877 accurate TRiSK-based finite volume method. In contrast, the second row illustrates the
 1878 error from the 10th-order accurate DGSEM. As anticipated, the TRiSK error is a few orders
 1879 of magnitude smaller, and the DGSEM error is several orders of magnitude smaller than the
 1880 solution magnitude. As observed in our main paper's test case simulations, the error plots
 1881 resonate with the intrinsic physics of the system. For example, the error associated with
 1882 the plane wave propagates at the same phase speed as the solution, mirroring the speed of
 1883 a shallow water gravity wave. In the TRiSK-based mimetic finite volume method, spurious
 1884 reflections observed at domain boundaries are likely due to the implementation of Dirichlet
 1885 boundary conditions that do not fully capture the characteristics of the incoming wave.
 1886 The method involves updating the normal velocities at the boundary edges of the hexagonal
 1887 mesh using exact solution values, whereas the normal velocities at the interior edges and the
 1888 surface elevation at cell centers are updated prognostically through numerical gradient and
 1889 divergence and formulations respectively. However, without direct boundary constraints on
 1890 surface elevation, discrepancies can arise during wave-boundary interactions. In contrast,
 1891 DGSEM updates zonal and meridional velocities as well as surface elevation at the interior
 1892 Gauss quadrature points of each element, with tendencies computed from both interior fluxes
 1893 at the quadrature points and numerical fluxes at the element's edges. Moreover, DGSEM
 1894 applies the exact solution as the external state at boundary edges, offering a more accurate
 1895 wave representation and minimizing reflections, aided by the dissipative properties of the
 1896 LLF Riemann solver at these edges. This distinction in boundary treatment between the
 1897 methods helps explain the observed differences in wave reflection.

1898 Given that the error magnitude is contingent on the exact solution and its gradients,
 1899 pronounced errors in regions characterized by high spatial gradients are unsurprising. This
 1900 is most prominent for the plane Gaussian wave error (both TRiSK and DGSEM), and the

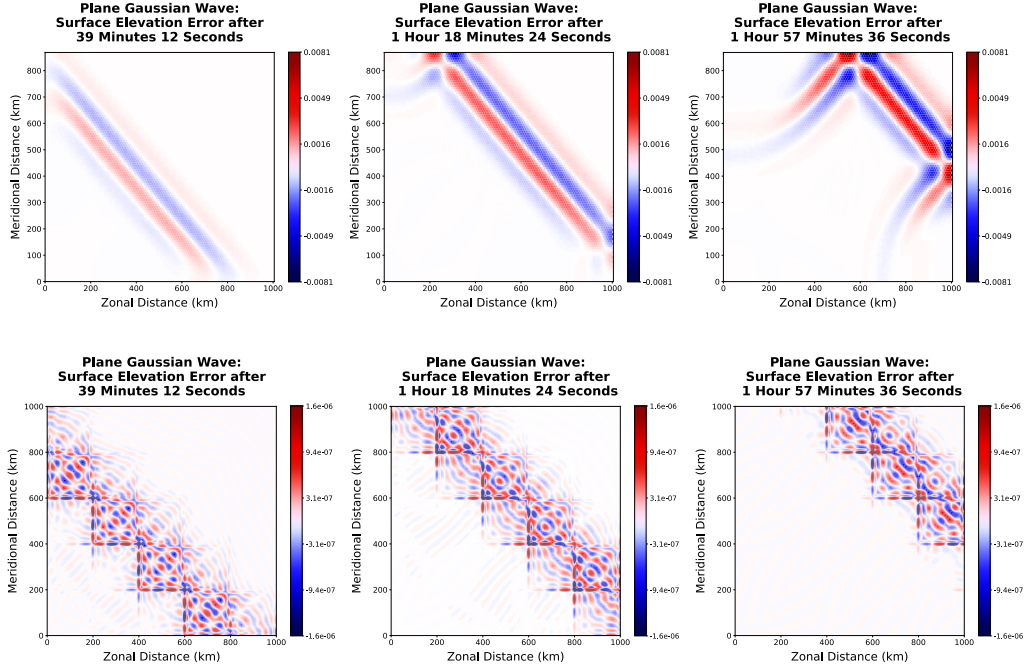


Figure A9. Time evolution of the surface elevation error of TC7, the plane Gaussian wave, spatially discretized with the TRiSK-based mimetic finite volume method (first row), and DGSEM using 5 elements and polynomial basis functions of order 10 in each horizontal direction (second row).

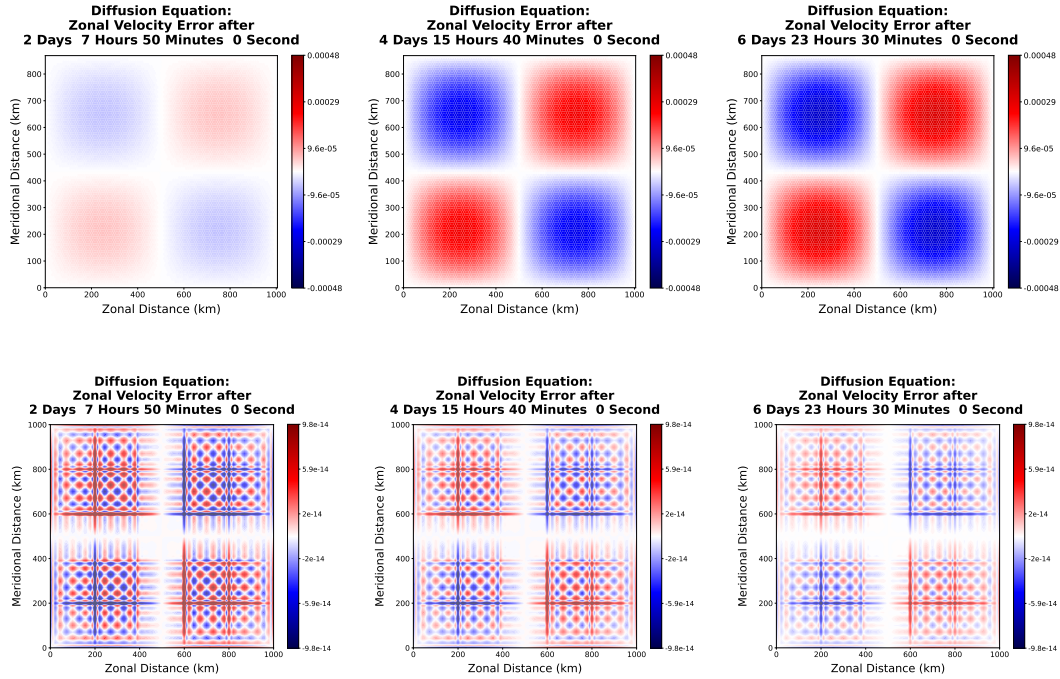


Figure A10. Same as Figure A9 but for TC8, the diffusion equation, showing error for TRiSK (first row) and DGSEM (second row).

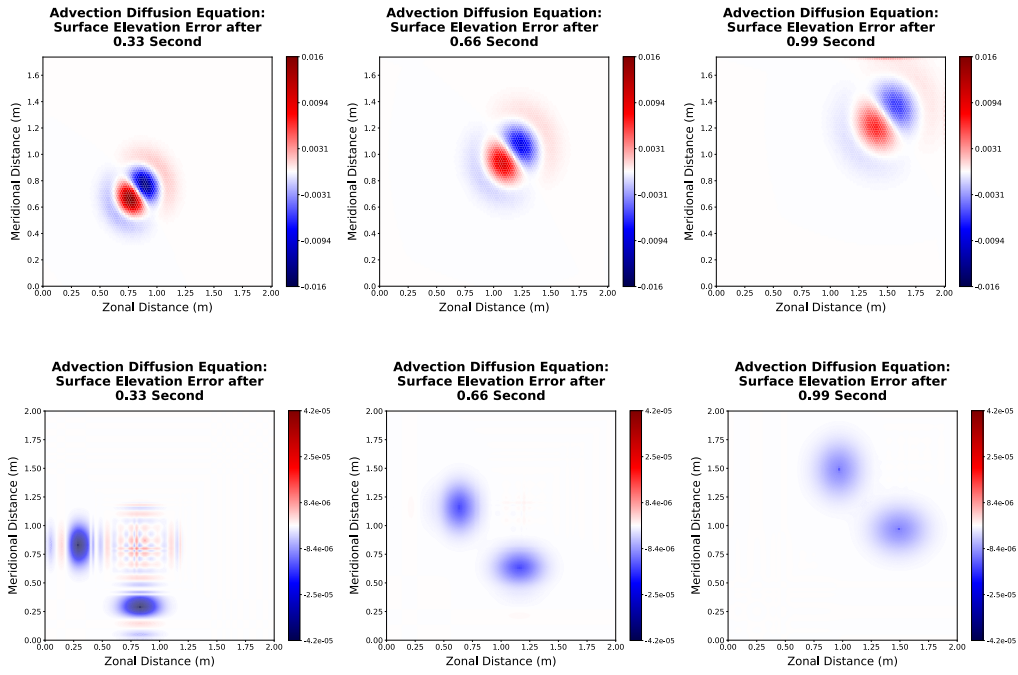


Figure A11. Same as Figure A9 but for TC9, the advection-diffusion equation, showing error for TRiSK (first row) and DGSEM (second row).

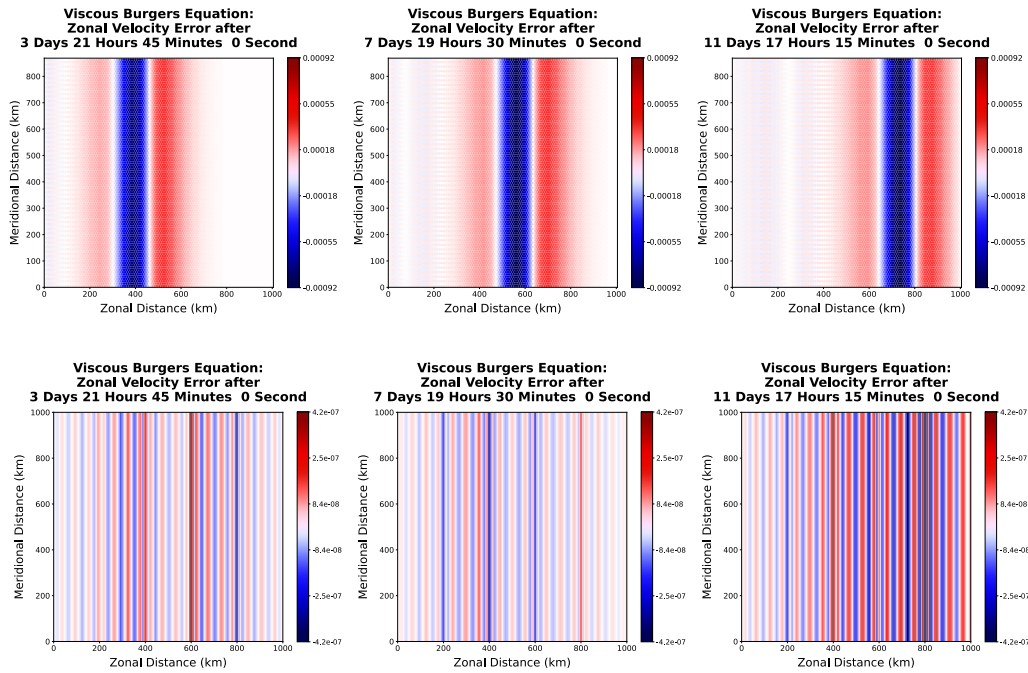


Figure A12. Same as Figure A9 but for TC10, the viscous Burgers shock wave, showing error for TRiSK (first row) and DGSEM (second row).

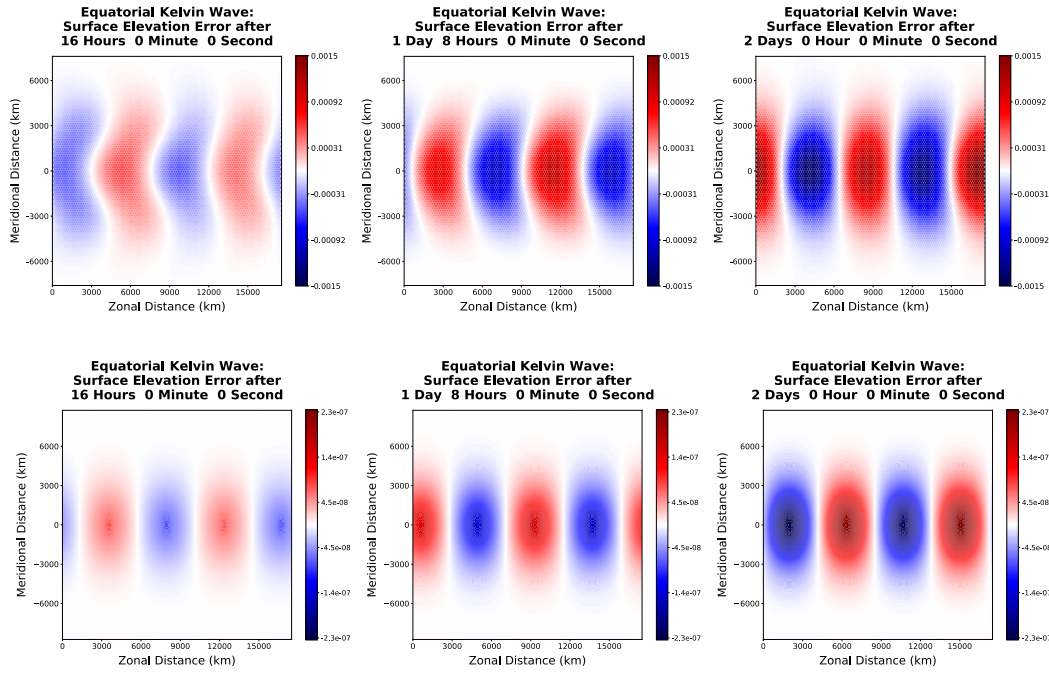


Figure A13. Time evolution of the surface elevation error of TC11, the non-dispersive equatorial Kelvin wave, spatially discretized with TRiSK (first row) and DGSEM (second row).

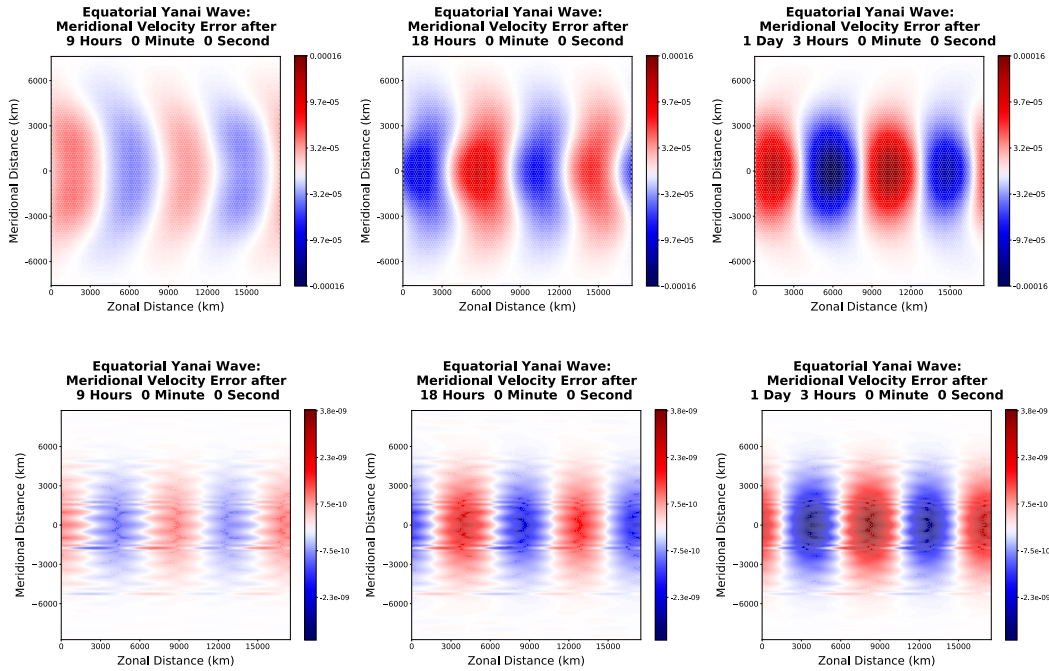


Figure A14. Same as Figure A13 but for TC12, the dispersive equatorial Yanai wave, showing the meridional velocity error for TRiSK (first row) and DGSEM (second row).

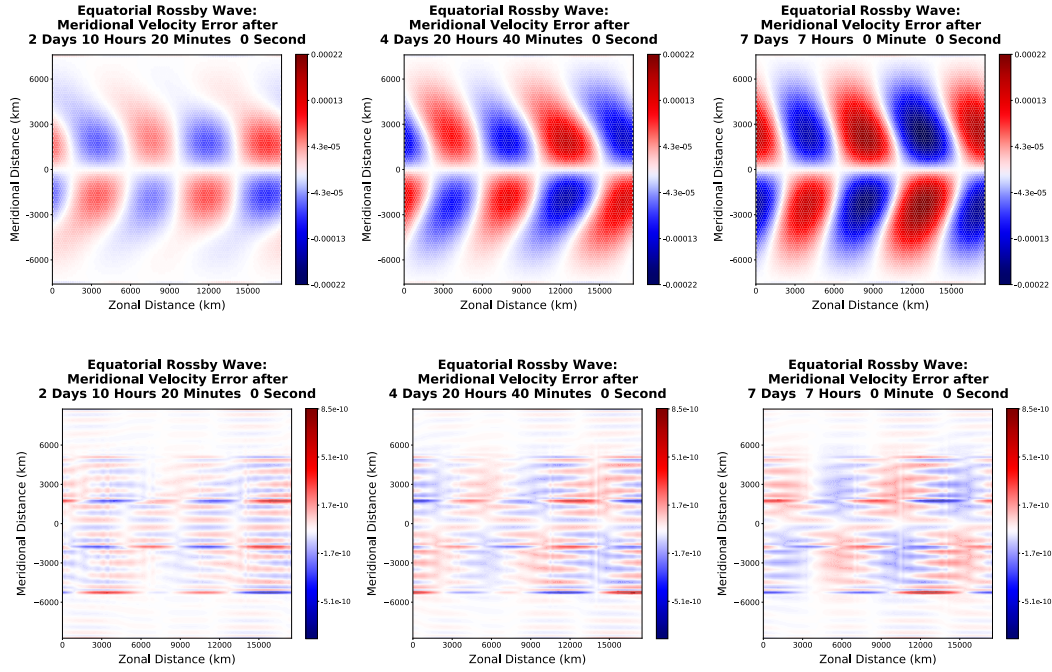


Figure A15. Same as Figure A13 but for TC13, the dispersive equatorial Rossby wave, showing the meridional velocity error for TRiSK (first row) and DGSEM (second row).

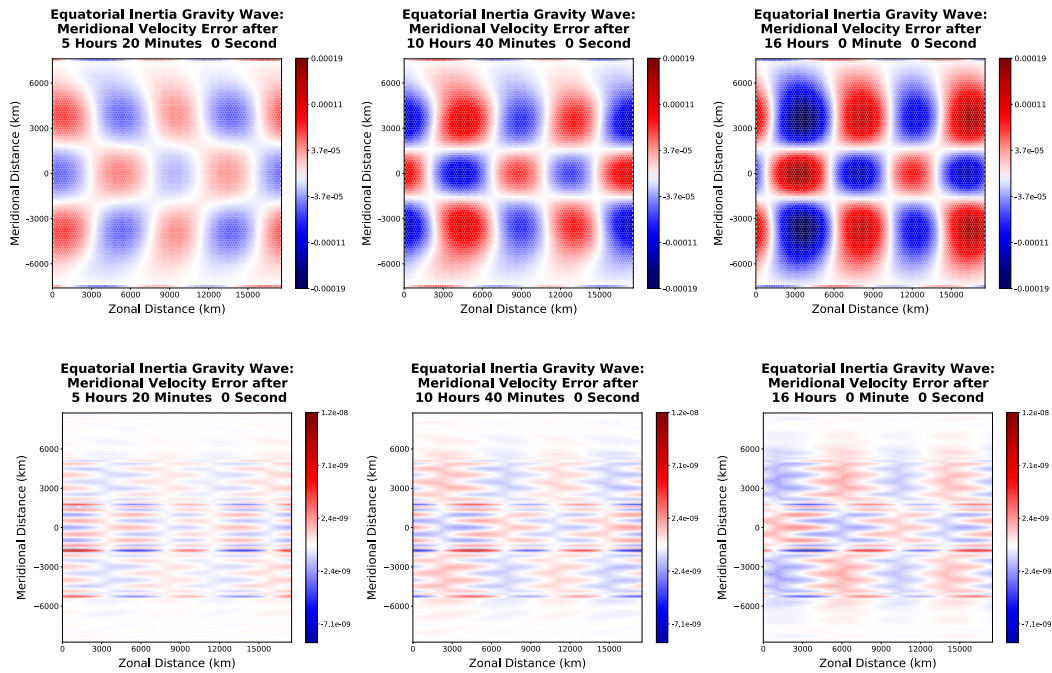


Figure A16. Same as Figure A13 but for TC14, the dispersive equatorial inertia-gravity wave, showing the meridional velocity error for TRiSK (first row) and DGSEM (second row).

1901 TRiSK error for the diffusion, advection-diffusion, and viscous Burgers' equations. The
 1902 DGSEM errors manifest in various forms, including numerical dispersion and dissipation,
 1903 and spurious oscillations (Section 5). The setup for the viscous Burgers' equation amplifies
 1904 the numerical dispersion and spurious oscillations (Figure A12), especially when compared to
 1905 linear test cases like the barotropic tide. The dispersive errors traverse element boundaries
 1906 and exit the domain at velocities surpassing that of the shock wave. For the equatorial
 1907 Kelvin, Yanai, Rossby, and inertia-gravity waves, the inherent dissipation of the mimetic
 1908 TRiSK scheme largely curtails the dispersive error prevalent in the DGSEM error. We
 1909 again encourage interested readers to access low p - and h -resolution DGSEM solution plots
 1910 from Bishnu (2024a), which reveal increased numerical dispersion and dissipation, although
 1911 spurious oscillations are not as prevalent. This observation is attributed to the deployment
 1912 of the LLF Riemann solver, whose primary function is to suppress such oscillations at the
 1913 edges of spectral elements. However, this solver introduces its own dissipative error, which
 1914 becomes more noticeable in coarser meshes where fewer elements are available to absorb it,
 1915 leading to visibly enhanced errors at element boundaries. Despite not affecting the spatial
 1916 order of accuracy (Section 5.1), the global pattern of this dissipative error unveils the element
 1917 boundaries, revealing the spectral elements' positions in the mesh. This, in conjunction with
 1918 the linear scaling of the color bars, rendering any error of magnitude lower than the dominant
 1919 error nearly invisible, can create the impression of mesh effects in the plots (Figures A9
 1920 and A10). Numerical dispersion is accentuated in the coarser meshes due to less accurate
 1921 representation of the physical phenomena at a given scale. For instance, the equatorial
 1922 Kelvin wave, akin to its coastal counterpart, exhibits no physical dispersion. However,
 1923 when simulated with less than three elements and third-order polynomial basis functions
 1924 in each horizontal direction, numerical dispersion significantly alters the phase speed across
 1925 varying wavelengths, which in turn, distort the shape of these physically non-dispersive
 1926 Kelvin waves as the simulation unfolds.

1927 **Appendix B Problem of Multiple Time Scales and Barotropic-Baroclinic** 1928 **Splitting in Ocean Models**

1929 In this section, we highlight the applicability of shallow water test cases within the
 1930 context of baroclinic-barotropic splitting in an ocean model. We initiate our discussion with
 1931 the challenge of multiple time scales inherent in ocean models, elucidating how the splitting
 1932 approach can effectively address this complication and boost computational efficiency. As
 1933 a practical example of the splitting procedure, we derive the barotropic and baroclinic
 1934 equations from the governing equations of MPAS-Ocean. We then demonstrate that the
 1935 barotropic equations assume the form of inhomogeneous rotating shallow water equations.

1936 Numerical ocean circulation models typically admit motions varying on a wide range
 1937 of time scales. For instance, the fast external gravity waves, approximately independent of
 1938 depth, propagate at a speed of $\mathcal{O}(100 \text{ ms}^{-1})$. On the other hand, the major current systems
 1939 and internal gravity waves exhibit velocities of $\mathcal{O}(1 \text{ ms}^{-1})$ i.e. two orders of magnitude less.
 1940 This vast disparity of time scales imposes a tremendous constraint on numerically modelling
 1941 oceanic phenomena. For explicit time-stepping methods, the CFL condition states that, for
 1942 a given Courant number, the maximum permissible time step of a hyperbolic system should
 1943 be inversely proportional to the wave speed to attain a numerically stable solution (see,
 1944 e.g. Griffies et al. (2005, Section 12.8). Therefore, the presence of external gravity waves
 1945 forces the time step to be much smaller than what is required to resolve the internal gravity
 1946 waves. Solving the full three-dimensional momentum equations with the smallest time
 1947 step dictated by the CFL condition of the fastest waves is computationally impractical, as
 1948 running a global simulation at high resolution (10 km grid cells or smaller) would require
 1949 time steps on the order of minutes. While restrictions of the time step size can be addressed
 1950 by using an implicit method, this would require solving a system of non-linear equations at
 1951 every time step thereby compensating for the reduction in computational time achieved by
 1952 increasing the time step size. A traditional alternative is to split the governing equations

1953 into two subsystems: a barotropic one for solving the fast depth independent motions and
 1954 a baroclinic one for solving the much slower depth dependent motions, as described in
 1955 Griffies et al. (2005); T. Ringler et al. (2013). Being independent of the vertical coordinate,
 1956 the fast barotropic subsystem is two-dimensional and the computational cost involved in
 1957 solving it, either explicitly using a small time step or implicitly using a large time step, is
 1958 drastically reduced. The full three-dimensional baroclinic subsystem modeling the slower
 1959 internal motions is solved explicitly using a much larger time step. Finally, if the baroclinic
 1960 variables are advanced explicitly using a small time step, a time-averaging filter is applied
 1961 over the barotropic solutions to minimize mode-splitting and aliasing errors (Shchepetkin
 1962 & McWilliams, 2005). The resulting time-averaged barotropic solutions are then reconciled
 1963 with their baroclinic counterparts to arrive at the total 3D states.

1964 As an illustrative example, we briefly discuss the barotropic-baroclinic splitting in
 1965 MPAS-Ocean. The MPAS-Ocean z -level formulation solves the following equations for
 1966 thickness, momentum, and tracers at layer k :

$$\frac{\partial h_k}{\partial t} + \nabla \cdot (h_k^{edge} \mathbf{u}_k) + \frac{\partial}{\partial z} (h_k w_k) = 0, \quad (B1)$$

$$\begin{aligned} \frac{\partial \mathbf{u}_k}{\partial t} + \frac{1}{2} \nabla |\mathbf{u}_k|^2 + (\mathbf{k} \cdot \nabla \times \mathbf{u}_k) \mathbf{u}_k^\perp + f \mathbf{u}_k^\perp + w_k^{edge} \frac{\partial \mathbf{u}_k}{\partial z} = & -\frac{1}{\rho_0} \nabla p_k + \nu_h \nabla^2 \mathbf{u}_k \\ & + \frac{\partial}{\partial z} \left(\nu_v \frac{\partial \mathbf{u}_k}{\partial z} \right), \end{aligned} \quad (B2)$$

$$\begin{aligned} \frac{\partial h_k \varphi_k}{\partial t} + \nabla \cdot (h_k^{edge} \varphi_k^{edge} \mathbf{u}_k) + \frac{\partial}{\partial z} (h_k \varphi_k w_k) = & \nabla \cdot (h_k^{edge} \kappa_h \nabla \varphi_k) \\ & + h_k \frac{\partial}{\partial z} \left(\kappa_v \frac{\partial \varphi_k}{\partial z} \right). \end{aligned} \quad (B3)$$

1967 The layer thickness h , vertical velocity w , pressure p , and tracer φ , are scalar quantities
 1968 defined at the center of near-hexagonal cells of the primal MPAS-Ocean mesh. The horizontal
 1969 velocity vector \mathbf{u} and the variables with *edge* superscript are defined at the edges of the
 1970 cells. The gradient, divergence and curl operators are all defined on the horizontal plane.
 1971 The barotropic and baroclinic velocities are

$$\bar{\mathbf{u}} = \frac{\sum_{k=1}^{N^{edge}} h_k^{edge} \mathbf{u}_k}{\sum_{k=1}^{N^{edge}} h_k^{edge}}, \quad (B4)$$

$$\mathbf{u}'_k = \mathbf{u}_k - \bar{\mathbf{u}}, \quad k = 1, 2, \dots, N. \quad (B5)$$

1972 If H is the mean depth in the absence of bottom topography, $h_b(x, y)$ is the topographic
 1973 height at (x, y) , and η is the surface elevation or the sea surface height (SSH),

$$\eta = \sum_{k=1}^{N^{edge}} h_k - \{H - h_b(x, y)\}. \quad (B6)$$

1974 Summing over all layers results in the barotropic surface elevation equation

$$\frac{\partial \eta}{\partial t} + \nabla \cdot \left(\bar{\mathbf{u}} \sum_{k=1}^{N^{edge}} h_k^{edge} \right) \equiv \frac{\partial \eta}{\partial t} + \nabla \cdot [\bar{\mathbf{u}} \{\eta + H - h_b(x, y)\}] = 0, \quad (B7)$$

1975 using the boundary conditions $w_{\frac{1}{2}} = w_{N+\frac{1}{2}} = 0$. Defining

$$\begin{aligned} \mathbf{T}(\mathbf{u}_k, w_k, p_k) = & -\frac{1}{2} \nabla |\mathbf{u}_k|^2 - (\mathbf{k} \cdot \nabla \times \mathbf{u}_k) \mathbf{u}_k^\perp - w_k^{edge} \frac{\partial \mathbf{u}_k}{\partial z} \\ & - \frac{1}{\rho_0} \nabla p_k + \nu_h \nabla^2 \mathbf{u}_k + \frac{\partial}{\partial z} \left(\nu_v \frac{\partial \mathbf{u}_k}{\partial z} \right), \end{aligned} \quad (B8)$$

1976 (B2) can be written in the more compact form

$$\frac{\partial \mathbf{u}_k}{\partial t} + f \mathbf{u}_k^\perp = \mathbf{T}(\mathbf{u}_k, w_k, p_k). \quad (\text{B9})$$

1977 Extracting the barotropic component of (B9),

$$\frac{\partial \bar{\mathbf{u}}}{\partial t} + f \bar{\mathbf{u}}^\perp = \bar{\mathbf{T}}(\mathbf{u}_k, w_k, p_k) \equiv -g \nabla \eta + \bar{\mathbf{G}}, \quad (\text{B10})$$

1978 where $\bar{\mathbf{T}}$ is the barotropic average of $\mathbf{T}_k = \mathbf{T}(\mathbf{u}_k, w_k, p_k)$ over all layers computed similar
 1979 to $\bar{\mathbf{u}}$ with \mathbf{u}_k replaced by \mathbf{T}_k in (B4), and $\bar{\mathbf{G}}$ is defined as $\bar{\mathbf{G}} = \bar{\mathbf{T}}(\mathbf{u}_k, w_k, p_k) + g \nabla \eta$.
 1980 Subtracting the barotropic equation (B10) from the total momentum equation (B9), we
 1981 obtain the baroclinic momentum equation

$$\frac{\partial \mathbf{u}'_k}{\partial t} + f \mathbf{u}'_k{}^\perp = \mathbf{T}(\mathbf{u}_k, w_k, p_k) + g \nabla \eta - \bar{\mathbf{G}}. \quad (\text{B11})$$

1982 It is evident that the barotropic equations (B7) and (B10) exhibit a resemblance to
 1983 the inviscid inhomogeneous rotating shallow water equations. However, this similarity is
 1984 marked by two key differences: the omission of the non-linear advection term and the
 1985 incorporation of a source term $\bar{\mathbf{G}}$ within the barotropic momentum equation. This latter
 1986 term, $\bar{\mathbf{G}}$, represents the barotropic average of $\mathbf{T}(\mathbf{u}_k, w_k, p_k) + g \nabla \eta$. The splitting procedure
 1987 and the split equations may vary slightly among different ocean models. One variation, as
 1988 observed in Blumberg and Mellor (1987), is to extract the diffusion of the barotropic velocity
 1989 out of the $\bar{\mathbf{G}}$ term so that the barotropic momentum equation becomes equivalent to the
 1990 viscous inhomogeneous linear rotating shallow water momentum equation

$$\frac{\partial \bar{\mathbf{u}}}{\partial t} + f \bar{\mathbf{u}}^\perp = -g \nabla \eta + \nu_h \nabla^2 \bar{\mathbf{u}} + \bar{\mathbf{G}}. \quad (\text{B12})$$

1991 Appendix C Details of Numerical Implementation

1992 In this section, we discuss subtle details in the numerical implementation of the shallow
 1993 water equations. Constructing the initial-boundary value problem to numerically obtain
 1994 the solution of the various test cases necessitates careful attention, particularly in ensuring
 1995 that the initial and boundary conditions are correctly applied on hexagonal meshes, and the
 1996 source terms for the manufactured solutions are exact. We will methodically tackle these
 1997 aspects, using a uniform MPAS-Ocean mesh with hexagonal primal cells and triangular
 1998 dual cells as a case study. The discussion culminates with addressing the crucial process
 1999 of interpolating the numerical solution or the error to the coarsest spatial mesh, before
 2000 calculating the error norm, for refinement only in space.

2001 C1 Specifying Initial and Boundary Conditions on Hexagonal Meshes

2002 For MPAS-Ocean, the prognostic variables are the surface elevations defined at the
 2003 centers of the primal cells and the normal velocities defined at the primal cell edges. The
 2004 spatial discretization of MPAS-Ocean based on the TRiSK scheme belongs to the category of
 2005 finite volume methods, which study the time evolution of cell- and edge-averaged quantities
 2006 in two dimensions, as opposed to the cell- and edge-centered ones. So, for a test case, it is
 2007 imperative to adopt an averaging procedure to determine the mean values of the prognostic
 2008 variables within every cell and edge. Since the cell-averaged quantity is the cell-integrated
 2009 quantity divided by the cell area, we need to first integrate the quantity over the area
 2010 spanned by a hexagonal cell. If the quantity consists of a complex combination of polynomial,
 2011 trigonometric, and exponential functions, performing the integration analytically may be a
 2012 Herculean task if not impossible. So, we resort to numerical quadrature, which may not
 2013 be exact but is definitely more accurate than the value at the cell center times the area of
 2014 the cell. Rules for evaluating numerical quadrature on regular hexagons first appeared in

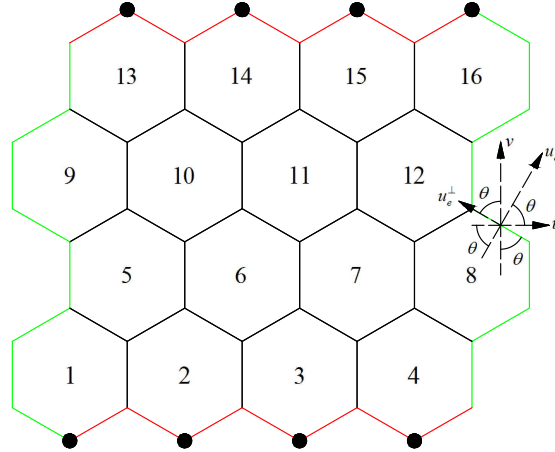


Figure C1. A 4×4 MPAS-Ocean mesh with non-periodic zonal and periodic meridional boundaries, showing the components of zonal and meridional velocities normal and tangential to an edge.

2015 Stroud (1971) followed by Lyness and Monegato (1977). In all test cases, we employ Lyness’
 2016 rule for integrating any scalar quantity over the hexagonal MPAS-Ocean cells. For exact
 2017 evaluation of the integral of polynomials upto degree 15 over the unit hexagon inscribed
 2018 within the unit circle centered at the origin, Table A.1 in Lyness and Monegato (1977) lists
 2019 the number of quadrature points, their coordinates, and weights.

2020 We use the Gauss-Legendre quadrature method to specify the edge-averaged normal
 2021 velocity at the midpoint of

- 2022 (a) every edge for the initial condition,
- 2023 (b) every edge along a non-periodic boundary for the boundary condition.

2024 Figure C1 is a schematic of a 4×4 MPAS-Ocean mesh with periodic zonal and
 2025 non-periodic meridional boundaries. It also shows the resolution of the zonal and meridional
 2026 velocities in the normal and tangential directions of a non-periodic boundary edge. Since
 2027 the prognostic variables include only the normal and not the tangential velocity, we do
 2028 not lose any generality by conducting a test case with zero zonal velocity (e.g. the Coastal
 2029 Kelvin wave) or one with zero meridional velocity (e.g. the non-linear manufactured solution)
 2030 since the normal velocity on these hexagonal MPAS-Ocean meshes will, in general, remain
 2031 non-zero in either case.

2032 C2 Specifying Source Terms for Manufactured Solutions

2033 The non-linear manufactured solution (38) satisfies inhomogeneous non-linear rotating
 2034 inviscid shallow water equations (38) on a flat bottom. The source terms (40) are obtained by
 2035 inserting the manufactured solution and its spatial and temporal gradients into the left-hand
 2036 side of these equations. On a hexagonal MPAS-Ocean mesh, the source term for the normal
 2037 velocity on an edge, where the normal makes an angle θ with the positive direction of the
 2038 x -axis is

$$s^{u^n} = s^u \cos \theta + s^v \sin \theta. \quad (C1)$$

2039 The cell-averaged source term for the surface elevation and the edge-averaged one for the
 2040 normal velocity can be obtained by following the same procedure outlined in Section C1 for
 2041 computing the cell-averaged surface elevation and the edge-averaged normal velocity.

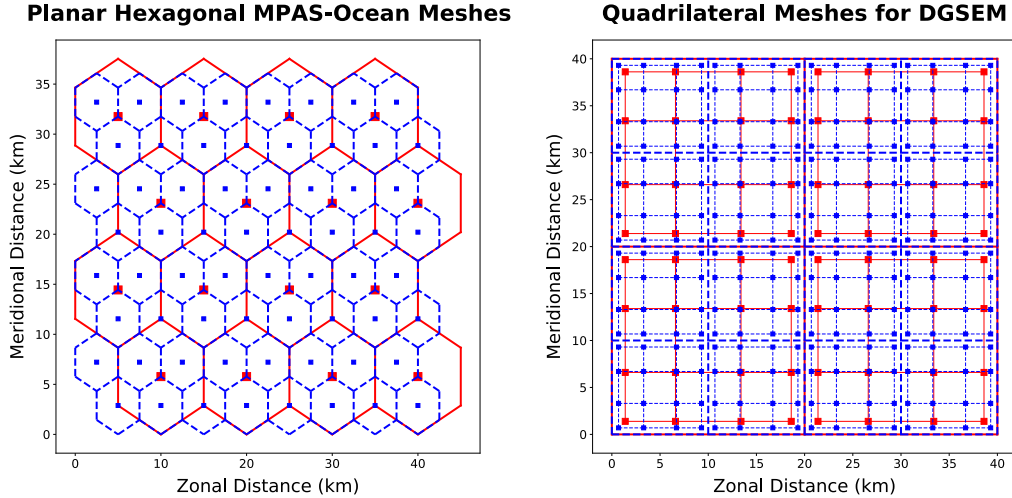


Figure C2. (a) A planar hexagonal MPAS-Ocean mesh consisting of 8 cells of width 5 km in each horizontal direction (in blue), superimposed on a coarser mesh consisting of 4 cells of width 10 km in each direction (in red) on the left. (b) A discontinuous Galerkin spectral element mesh (DGSEMesh) consisting of 4 elements of width 10 km and polynomial basis functions of order 4 in each horizontal direction (in blue) superimposed on a coarser mesh consisting of 2 elements of width 20 km and the same polynomial order in each direction (in red) on the right.

2042

C3 Interpolation to the Coarsest Mesh

2043

2044

2045

2046

2047

2048

2049

2050

2051

2052

2053

2054

2055

2056

2057

2058

2059

As a final note, for refinement only in space, we need to interpolate the numerical solution (or the error) to the coarsest mesh before taking the difference in the numerical solution (or the error) for successive spatial resolutions and computing its norm. Figure C2 illustrates (a) a planar hexagonal MPAS-Ocean mesh consisting of 8 cells of width 5 km in each horizontal direction (in blue), superimposed on a coarser mesh consisting of 4 cells of width 10 km in each direction (in red); and (b) a discontinuous Galerkin spectral element mesh (DGSEMesh) consisting of 4 elements of width 10 km and polynomial basis functions of order 4 in each horizontal direction (in blue) superimposed on a coarser mesh consisting of 2 elements of width 20 km and the same polynomial order in each direction (in red). The cell centers of the MPAS-Ocean meshes and the quadrature nodes within each element of the DGSEMeshes are represented by square markers. In Figure C2(a), the numerical solution (or the error) on the finer mesh is interpolated to the coarser mesh with a bilinear interpolant (Vetterling & Press, 1992). In Figure C2(b), a Newton-Raphson method is used to determine the physical coordinates of the quadrature nodes of the coarser mesh with respect to the computational coordinates of the quadrature nodes of the finer mesh. Then, the polynomial representation of the solution (or the error) on the finer mesh is evaluated at these physical coordinates.

2060

Open Research Section

2061

2062

2063

2064

2065

The model code and visualization scripts may be accessed from the GitHub repository at https://github.com/siddharthabishnu/Rotating_Shallow_Water_Verification_Suite/tree/v1.2.5, and may also be downloaded from the Zenodo release (Bishnu, 2024a) at <https://doi.org/10.5281/zenodo.10460245>. The mesh files (Bishnu, 2023) used for initialization, may be obtained from <https://doi.org/10.5281/zenodo.10161055>, and

2066 the output files (Bishnu, 2024b) including the solution, error and convergence plots, may be
2067 downloaded from <https://doi.org/10.5281/zenodo.10460252>.

2068 Acknowledgments

2069 Siddhartha Bishnu has been supported by Scientific Discovery through Advanced Computing
2070 (SciDAC) projects LEAP (Launching an Exascale ACME Prototype) and CANGA (Coupling
2071 Approaches for Next Generation Architectures) under the U.S. Department of Energy
2072 (DOE), Office of Science, Office of Biological and Environmental Research (BER). Mark
2073 Petersen was supported as part of the Energy Exascale Earth System Model (E3SM)
2074 project, also funded by the DOE BER. This research used resources provided by the
2075 Los Alamos National Laboratory Institutional Computing Program, which is supported by
2076 the U.S. Department of Energy National Nuclear Security Administration under Contract
2077 No. 89233218CNA000001.

2078 The authors extend their profound gratitude to the anonymous reviewers for their
2079 constructive feedback, encouraging comments, and invaluable recommendations. Their
2080 contributions have been instrumental in enhancing both the quality and the presentation
2081 of this paper. Additionally, the authors recognize the beneficial interactions with Tomasz
2082 Plewa and Sachin Shanbhag at the Florida State University and Darren Engwirda at the
2083 Los Alamos National Laboratory.

2084 References

- 2085 Asay-Davis, X., & Begeman, C. (2024). *Polaris*. [https://github.com/E3SM-Project/](https://github.com/E3SM-Project/polaris)
2086 [polaris](https://github.com/E3SM-Project/polaris). GitHub.
- 2087 Asay-Davis, X., Begeman, C., & Petersen, M. (2024). *COMPASS (Configuration Of Model*
2088 *for Prediction Across Scales Setups) repository*. [https://github.com/MPAS-Dev/](https://github.com/MPAS-Dev/compass)
2089 [compass](https://github.com/MPAS-Dev/compass). GitHub.
- 2090 Baldwin, M., Gray, L., Dunkerton, T., Hamilton, K., Haynes, P., Randel, W. J., . . . others
2091 (2001). The quasi-biennial oscillation. *Reviews of Geophysics*, *39*(2), 179–229.
- 2092 Barbeiro, S., Ferreira, J., & Grigorieff, R. (2005). Supraconvergence of a finite difference
2093 scheme for solutions in h s $(0, 1)$. *IMA journal of numerical analysis*, *25*(4), 797–811.
- 2094 Bassi, F., & Rebay, S. (1997). A high-order accurate discontinuous finite element method
2095 for the numerical solution of the compressible navier–stokes equations. *Journal of*
2096 *computational physics*, *131*(2), 267–279.
- 2097 Bathe, K.-J. (2006). *Finite element procedures*. Klaus-Jurgen Bathe.
- 2098 Beel, A., Kim, T.-Y., Jiang, W., & Song, J.-H. (2019). Strong form-based meshfree
2099 collocation method for wind-driven ocean circulation. *Computer Methods in Applied*
2100 *Mechanics and Engineering*, *351*, 404–421.
- 2101 Bishnu, S. (2021). *Time-Stepping Methods for Partial Differential Equations and Ocean*
2102 *Models* (Doctoral dissertation, Florida State University). doi: 10.5281/zenodo
2103 .7439539
- 2104 Bishnu, S. (2023, November). *MPAS-Ocean Shallow Water Meshes*. Zenodo. Retrieved
2105 from <https://doi.org/10.5281/zenodo.10161055> doi: 10.5281/zenodo.10161055
- 2106 Bishnu, S. (2024a, January). *Rotating shallow water verification suite*. Zenodo. Retrieved
2107 from <https://doi.org/10.5281/zenodo.10460245> doi: 10.5281/zenodo.10460245
- 2108 Bishnu, S. (2024b, January). *Rotating shallow water verification suite output*. Zenodo.
2109 Retrieved from <https://doi.org/10.5281/zenodo.10460252> doi: 10.5281/zenodo
2110 .10460252
- 2111 Bishnu, S., Strauss, R. R., & Petersen, M. R. (2023). Comparing the Performance of
2112 Julia on CPUs versus GPUs and Julia-MPI versus Fortran-MPI: a case study with
2113 MPAS-Ocean (Version 7.1). *Geoscientific Model Development*, *16*(19), 5539–5559.
2114 Retrieved from <https://gmd.copernicus.org/articles/16/5539/2023/> doi: 10
2115 .5194/gmd-16-5539-2023

- 2116 Blackburn, M., & Hoskins, B. J. (2013). Context and aims of the aqua-planet experiment.
2117 *Journal of the Meteorological Society of Japan. Ser. II*, *91*, 1–15.
- 2118 Blackburn, M., Williamson, D. L., Nakajima, K., Ohfuchi, W., Takahashi, Y. O., Hayashi,
2119 Y.-Y., ... others (2013). The aqua-planet experiment (ape): Control sst simulation.
2120 *Journal of the Meteorological Society of Japan. Ser. II*, *91*, 17–56.
- 2121 Blumberg, A. F., & Mellor, G. L. (1987). A description of a three-dimensional coastal ocean
2122 circulation model. *Three-dimensional coastal ocean models*, *4*, 1–16.
- 2123 Boyd, J. P. (1988). Spectral methods in fluid dynamics (c. canuto, my hussaini, a. quarteroni,
2124 and ta zang). *SIAM Review*, *30*(4), 666–668.
- 2125 Burchard, H., & Rennau, H. (2008). Comparative quantification of physically and
2126 numerically induced mixing in ocean models. *Ocean Modelling*, *20*(3), 293–311.
- 2127 Calandrini, S., Engwirda, D., & Petersen, M. (2021). Comparing numerical accuracy and
2128 stability for different horizontal discretizations in MPAS-Ocean. *Ocean Modelling*,
2129 *168*, 101908. Retrieved from [https://www.sciencedirect.com/science/article/
2130 pii/S146350032100161X](https://www.sciencedirect.com/science/article/pii/S146350032100161X) doi: <https://doi.org/10.1016/j.ocemod.2021.101908>
- 2131 Canuto, C., Hussaini, M. Y., Quarteroni, A., & Zang, T. A. (2007a). *Spectral methods:
2132 evolution to complex geometries and applications to fluid dynamics*. Springer Science
2133 & Business Media.
- 2134 Canuto, C., Hussaini, M. Y., Quarteroni, A., & Zang, T. A. (2007b). *Spectral methods:
2135 fundamentals in single domains*. Springer Science & Business Media.
- 2136 Capodaglio, G., & Petersen, M. (2022). Local time stepping for the shallow water equations
2137 in MPAS. *Journal of Computational Physics*, *449*, 110818. Retrieved from [https://
2138 www.sciencedirect.com/science/article/pii/S0021999121007130](https://www.sciencedirect.com/science/article/pii/S0021999121007130) doi: [https://
2139 doi.org/10.1016/j.jcp.2021.110818](https://doi.org/10.1016/j.jcp.2021.110818)
- 2140 Carpenter, M. H., & Kennedy, C. A. (1994). *Fourth-order 2N-storage Runge-Kutta schemes*.
2141 Langley Research Center.
- 2142 Chavas, D. R., & Reed, K. A. (2019). Dynamical aquaplanet experiments with uniform
2143 thermal forcing: System dynamics and implications for tropical cyclone genesis and
2144 size. *Journal of the Atmospheric Sciences*, *76*(8), 2257–2274.
- 2145 Chen, C., Beardsley, R. C., & Cowles, G. (2006, March). An unstructured grid, finite-volume
2146 coastal ocean model (fvcom) system. *Oceanography*, *19*, 78–89. Retrieved from
2147 <https://doi.org/10.5670/oceanog.2006.92>
- 2148 Chen, Q., & Ju, L. (2018). Conservative finite-volume schemes for the quasi-geostrophic
2149 equation on coastal-conforming unstructured primal–dual meshes. *Quarterly Journal
2150 of the Royal Meteorological Society*, *144*(713), 1106–1122.
- 2151 Clarke, A. J. (1991). The dynamics of barotropic tides over the continental shelf and slope.
2152 *Tidal Hydrodynamics*, *79*, 108.
- 2153 Clarke, A. J. (2008). *An introduction to the dynamics of el niño and the southern oscillation*.
2154 Elsevier.
- 2155 Clarke, A. J., & Battisti, D. S. (1981). The effect of continental shelves on tides. *Deep Sea
2156 Research Part A. Oceanographic Research Papers*, *28*(7), 665–682.
- 2157 Cockburn, B., & Shu, C.-W. (1989). Tvb runge-kutta local projection discontinuous galerkin
2158 finite element method for conservation laws. ii. general framework. *Mathematics of
2159 computation*, *52*(186), 411–435.
- 2160 Cockburn, B., & Shu, C.-W. (1998). The runge–kutta discontinuous galerkin method for
2161 conservation laws v: multidimensional systems. *Journal of computational physics*,
2162 *141*(2), 199–224.
- 2163 Comblen, R., Lambrechts, J., Remacle, J.-F., & Legat, V. (2010). Practical evaluation of
2164 five partly discontinuous finite element pairs for the non-conservative shallow water
2165 equations. *International Journal for Numerical Methods in Fluids*, *63*(6), 701–724.
- 2166 Cushman-Roisin, B., & Beckers, J.-M. (2011). *Introduction to geophysical fluid dynamics:
2167 physical and numerical aspects*. Academic press.
- 2168 Danilov, S., Kivman, G., & Schröter, J. (2004). A finite-element ocean model: principles
2169 and evaluation. *Ocean Modelling*, *6*(2), 125–150.
- 2170 Dennis, J. M., Edwards, J., Evans, K. J., Guba, O., Lauritzen, P. H., Mirin, A. A., ...

- 2171 Worley, P. H. (2012). Cam-se: A scalable spectral element dynamical core for
 2172 the community atmosphere model. *The International Journal of High Performance*
 2173 *Computing Applications*, 26(1), 74–89.
- 2174 Donea, J., & Huerta, A. (2003). *Finite element methods for flow problems*. John Wiley &
 2175 Sons.
- 2176 Donohoe, A., Frierson, D. M., & Battisti, D. S. (2014). The effect of ocean mixed layer
 2177 depth on climate in slab ocean aquaplanet experiments. *Climate dynamics*, 43(3-4),
 2178 1041–1055.
- 2179 Drago, M., & Iovenitti, L. (2000). σ -coordinates hydrodynamic numerical model for coastal
 2180 and ocean three-dimensional circulation. *Ocean Engineering*, 27(10), 1065–1085.
- 2181 Düben, P. D., Korn, P., & Aizinger, V. (2012). A discontinuous/continuous low order
 2182 finite element shallow water model on the sphere. *Journal of Computational Physics*,
 2183 231(6), 2396–2413.
- 2184 Evans, K. J., Archibald, R. K., Gardner, D. J., Norman, M. R., Taylor, M. A., Woodward,
 2185 C. S., & Worley, P. H. (2019). Performance analysis of fully explicit and fully implicit
 2186 solvers within a spectral element shallow-water atmosphere model. *The International*
 2187 *Journal of High Performance Computing Applications*, 33(2), 268–284.
- 2188 Eymard, E., Gallouët, T., & Herbin, R. (2003). *Finite volume method handbook of numerical*
 2189 *analysis, editors: Pg ciarlet and jl lions, vol. 70*. Amsterdam, North Holland.
- 2190 Ezer, T., & Mellor, G. L. (2004). A generalized coordinate ocean model and a comparison of
 2191 the bottom boundary layer dynamics in terrain-following and in z-level grids. *Ocean*
 2192 *Modelling*, 6(3-4), 379–403.
- 2193 Farlow, S. J. (1993). *Partial differential equations for scientists and engineers*. Courier
 2194 Corporation.
- 2195 Ferreira, J. A., & Grigorieff, R. D. (1998). On the supraconvergence of elliptic finite
 2196 difference schemes. *Applied numerical mathematics*, 28(2-4), 275–292.
- 2197 Foster, E. L., Iliescu, T., & Wang, Z. (2013). A finite element discretization of the
 2198 streamfunction formulation of the stationary quasi-geostrophic equations of the ocean.
 2199 *Computer Methods in Applied Mechanics and Engineering*, 261, 105–117.
- 2200 Fringer, O., Gerritsen, M., & Street, R. (2006). An unstructured-grid, finite-volume,
 2201 nonhydrostatic, parallel coastal ocean simulator. *Ocean Modelling*, 14(3-4), 139–173.
- 2202 Garcia, M., Choboter, P. F., Walter, R. K., & Castillo, J. E. (2019). Validation of the
 2203 nonhydrostatic general curvilinear coastal ocean model (gccom) for stratified flows.
 2204 *Journal of computational science*, 30, 143–156.
- 2205 Gassner, G. J., Winters, A. R., & Kopriva, D. A. (2016). A well balanced and entropy
 2206 conservative discontinuous galerkin spectral element method for the shallow water
 2207 equations. *Applied Mathematics and Computation*, 272(P2), 291-308. Retrieved
 2208 from [https://EconPapers.repec.org/RePEc:eee:apmaco:v:272:y:2016:i:p2:p:](https://EconPapers.repec.org/RePEc:eee:apmaco:v:272:y:2016:i:p2:p:291-308)
 2209 291-308
- 2210 Gibson, A. H., Hogg, A. M., Kiss, A. E., Shakespeare, C. J., & Adcroft, A. (2017).
 2211 Attribution of horizontal and vertical contributions to spurious mixing in an arbitrary
 2212 Lagrangian–Eulerian ocean model. *Ocean Modelling*, 119, 45–56.
- 2213 Gill, A. E. (2016). *Atmosphere—ocean dynamics*. Elsevier.
- 2214 Griffies, S. M., Gnanadesikan, A., Dixon, K. W., Dunne, J. P., Gerdes, R., Harrison, M. J.,
 2215 ... Zhang, R. (2005, September). Formulation of an ocean model for global climate
 2216 simulations. *Ocean Sci.*, 1(1), 45–79. Retrieved 2018-02-21, from [https://www.ocean-](https://www.ocean-sci.net/1/45/2005/)
 2217 [sci.net/1/45/2005/](https://www.ocean-sci.net/1/45/2005/) doi: 10.5194/os-1-45-2005
- 2218 Haberman, R. (1998). *Elementary applied partial differential equations: With fourier series*
 2219 *and boundary value problems*. Prentice-Hall.
- 2220 Haidvogel, D. B., & Beckmann, A. (1999). *Numerical ocean circulation modeling*. World
 2221 Scientific.
- 2222 Hecht, M. W., Wingate, B. A., & Kassis, P. (2000). A better, more discriminating test
 2223 problem for ocean tracer transport. *Ocean Modelling*, 2(1-2), 1–15.
- 2224 Hell, M. C. (2020). *Atmosphere-ocean momentum exchange by extra-tropical storms*.
 2225 University of California, San Diego.

- 2226 Herzfeld, M., Schmidt, M., Griffies, S., & Liang, Z. (2011). Realistic test cases for limited
2227 area ocean modelling. *Ocean Modelling*, *37*(1-2), 1–34.
- 2228 Hesthaven, J., & Warburton, T. (2007). *Nodal discontinuous galerkin methods: Algorithms,*
2229 *analysis, and applications*. Springer Science & Business Media.
- 2230 Hughes, T. (2012). *The finite element method: Linear static and dynamic finite element*
2231 *analysis*. Dover Publications.
- 2232 Hussaini, M. Y., & Zang, T. A. (1987). Spectral methods in fluid dynamics. *Annual review*
2233 *of fluid mechanics*, *19*(1), 339–367.
- 2234 Ilıcak, M., Adcroft, A. J., Griffies, S. M., & Hallberg, R. W. (2012). Spurious dianeutral
2235 mixing and the role of momentum closure. *Ocean Modelling*, *45*, 37–58.
- 2236 Jalali, M., Rapaka, N. R., & Sarkar, S. (2014). Tidal flow over topography: effect of
2237 excursion number on wave energetics and turbulence. *Journal of fluid mechanics*,
2238 *750*, 259–283.
- 2239 Jankowski, J. A. (1999). *A non-hydrostatic model for free surface flows* (Unpublished
2240 doctoral dissertation). Inst. für Strömungsmechanik und Elektronisches Rechnen im
2241 Bauwesen.
- 2242 Jiang, W., & Kim, T.-Y. (2016). Spline-based finite-element method for the stationary
2243 quasi-geostrophic equations on arbitrary shaped coastal boundaries. *Computer*
2244 *Methods in Applied Mechanics and Engineering*, *299*, 144–160.
- 2245 Kärnä, T., Kramer, S. C., Mitchell, L., Ham, D. A., Piggott, M. D., & Baptista, A. M.
2246 (2018). Thetis coastal ocean model: discontinuous galerkin discretization for the
2247 three-dimensional hydrostatic equations. *Geoscientific Model Development*, *11*(11),
2248 4359–4382.
- 2249 Kärnä, T., Legat, V., & Deleersnijder, E. (2013). A baroclinic discontinuous galerkin finite
2250 element model for coastal flows. *Ocean Modelling*, *61*, 1–20.
- 2251 Karniadakis, G., & Sherwin, S. (2005). *Spectral/hp element methods for computational fluid*
2252 *dynamics*. Numerical Mathematics and Scie.
- 2253 Kim, T.-Y., Iliescu, T., & Fried, E. (2015). B-spline based finite-element method for the
2254 stationary quasi-geostrophic equations of the ocean. *Computer Methods in Applied*
2255 *Mechanics and Engineering*, *286*, 168–191.
- 2256 Kopera, M. A., Gahounzo, Y., Enderlin, E. M., Giraldo, F. X., & Maslowski, W. (2023).
2257 Non-hydrostatic unified model of the ocean with application to ice/ocean interaction
2258 modeling. *GEM-International Journal on Geomathematics*, *14*(1), 2.
- 2259 Kopera, M. A., Giraldo, F. X., & Maslowski, W. (2018). *Ice-sheet/ocean interaction model*
2260 *for greenland fjords using high-order discontinuous galerkin methods* (Tech. Rep.).
2261 University of California, Santa Cruz/Naval Postgraduate School.
- 2262 Kopriva, D., & Gassner, G. (2010, 08). On the quadrature and weak form choices in
2263 collocation type discontinuous galerkin spectral element methods. *J. Sci. Comput.*,
2264 *44*, 136-155. doi: 10.1007/s10915-010-9372-3
- 2265 Kopriva, D. A. (2009). *Implementing spectral methods for partial differential equations:*
2266 *Algorithms for scientists and engineers*. Springer Science & Business Media.
- 2267 Kopriva, D. A., Nordström, J., & Gassner, G. J. (2017). Error boundedness of discontinuous
2268 galerkin spectral element approximations of hyperbolic problems. *Journal of Scientific*
2269 *Computing*, *72*, 314–330.
- 2270 Lax, P. D., & Richtmyer, R. D. (1956). Survey of the stability of linear finite difference
2271 equations. *Communications on pure and applied mathematics*, *9*(2), 267–293.
- 2272 Legg, S., Hallberg, R. W., & Girton, J. B. (2006). Comparison of entrainment in overflows
2273 simulated by z-coordinate, isopycnal and non-hydrostatic models. *Ocean Modelling*,
2274 *11*(1-2), 69–97.
- 2275 LeVeque, R. J. (2002). *Finite volume methods for hyperbolic problems* (Vol. 31). Cambridge
2276 university press.
- 2277 Levine, N. (1985). Superconvergent recovery of the gradient from piecewise linear
2278 finite-element approximations. *IMA Journal of numerical analysis*, *5*(4), 407–427.
- 2279 Logan, D. L. (2022). *First course in the finite element method, enhanced edition, si version*.
2280 Cengage Learning.

- 2281 Logan, J. D. (2014). *Applied partial differential equations*. Springer.
- 2282 Lyness, J., & Monegato, G. (1977). Quadrature rules for regions having regular hexagonal
2283 symmetry. *SIAM Journal on Numerical Analysis*, *14*(2), 283–295.
- 2284 Maday, Y., & Patera, A. T. (1989). Spectral element methods for the incompressible
2285 navier-stokes equations. *IN: State-of-the-art surveys on computational mechanics*
2286 *(A90-47176 21-64)*. New York, 71–143.
- 2287 Madec, G., et al. (2023, July). *Nemo ocean engine reference manual*. Zenodo. Retrieved
2288 from <https://doi.org/10.5281/zenodo.8167700> doi: 10.5281/zenodo.8167700
- 2289 Marshall, J., Adcroft, A., Hill, C., Perelman, L., & Heisey, C. (1997). A finite-volume,
2290 incompressible Navier Stokes model for studies of the ocean on parallel computers.
2291 *Journal of Geophysical Research: Oceans*, *102*(C3), 5753–5766.
- 2292 Medeiros, B., Williamson, D. L., & Olson, J. G. (2016). Reference aquaplanet climate in
2293 the community atmosphere model, version 5. *Journal of Advances in Modeling*
2294 *Earth Systems*, *8*(1), 406–424.
- 2295 Merlis, T. M., & Held, I. M. (2019). Aquaplanet simulations of tropical cyclones. *Current*
2296 *Climate Change Reports*, *5*(3), 185–195.
- 2297 Möbis, B., & Stevens, B. (2012). Factors controlling the position of the intertropical
2298 convergence zone on an aquaplanet. *Journal of Advances in Modeling Earth Systems*,
2299 *4*(4).
- 2300 Munk, W. H., & Carrier, G. F. (1950). The wind-driven circulation in ocean basins of
2301 various shapes. *Tellus*, *2*(3), 158–167.
- 2302 Myers, P. G., & Weaver, A. J. (1995). A diagnostic barotropic finite-element ocean
2303 circulation model. *Journal of Atmospheric and Oceanic Technology*, *12*(3), 511–526.
- 2304 Neale, R. B., & Hoskins, B. J. (2000). A standard test for agcms including their physical
2305 parametrizations: I: The proposal. *Atmospheric Science Letters*, *1*(2), 101–107.
- 2306 Patankar, S. (2018). *Numerical heat transfer and fluid flow*. Taylor & Francis.
- 2307 Patera, A. (1984). A spectral element method for fluid dynamics: Laminar flow in a channel
2308 expansion. *Journal of Computational Physics*, *54*(3), 468–488.
- 2309 Pedlosky, J. (1987). *Geophysical fluid dynamics* (Vol. 710). Springer.
- 2310 Petersen, M. R., Jacobsen, D. W., Ringler, T. D., Hecht, M. W., & Maltrud, M. E. (2015).
2311 Evaluation of the arbitrary Lagrangian–Eulerian vertical coordinate method in the
2312 MPAS-Ocean model. *Ocean Modelling*, *86*, 93–113.
- 2313 Philander, S., Holton, J., & Dmowska, R. (1989). *El nino, la nina, and the southern*
2314 *oscillation*. Elsevier Science. Retrieved from [https://books.google.com/books?id=](https://books.google.com/books?id=9fwrkW\B1YYC)
2315 [9fwrkW\B1YYC](https://books.google.com/books?id=9fwrkW\B1YYC)
- 2316 Ramadhan, A., Wagner, G. L., Hill, C., Campin, J.-M., Churavy, V., Besard, T., ...
2317 Marshall, J. (2020). Oceananigans.jl: Fast and friendly geophysical fluid dynamics
2318 on gpus. *Journal of Open Source Software*, *5*(53), 2018. Retrieved from [https://](https://doi.org/10.21105/joss.02018)
2319 doi.org/10.21105/joss.02018 doi: 10.21105/joss.02018
- 2320 Ranocha, H. (2016, dec). Shallow water equations: split-form, entropy stable, well-balanced,
2321 and positivity preserving numerical methods. *GEM - International Journal on*
2322 *Geomathematics*, *8*(1), 85–133. Retrieved from <https://doi.org/10.1007%2Fs13137>
2323 [-016-0089-9](https://doi.org/10.1007/s13137-016-0089-9) doi: 10.1007/s13137-016-0089-9
- 2324 Reckinger, S. M., Petersen, M. R., & Reckinger, S. J. (2015). A study of overflow simulations
2325 using MPAS-Ocean: Vertical grids, resolution, and viscosity. *Ocean Modelling*,
2326 *96, Part 2*, 291 - 313. Retrieved from [http://www.sciencedirect.com/science/](http://www.sciencedirect.com/science/article/pii/S146350031500164X)
2327 [article/pii/S146350031500164X](http://www.sciencedirect.com/science/article/pii/S146350031500164X) doi: <http://dx.doi.org/10.1016/j.ocemod.2015.09>
2328 .006
- 2329 Reddy, J. N. (2019). *Introduction to the finite element method*. McGraw-Hill Education.
- 2330 Ringler, T., Petersen, M., Higdon, R., Jacobsen, D., Jones, P., & Maltrud, M. (2013).
2331 A multi-resolution approach to global ocean modeling. *Ocean Modelling*, *69*(0),
2332 211–232. Retrieved from [http://www.sciencedirect.com/science/article/pii/](http://www.sciencedirect.com/science/article/pii/S1463500313000760)
2333 [S1463500313000760](http://www.sciencedirect.com/science/article/pii/S1463500313000760) doi: <http://dx.doi.org/10.1016/j.ocemod.2013.04.010>
- 2334 Ringler, T. D., Thuburn, J., Klemp, J. B., & Skamarock, W. C. (2010). A unified approach
2335 to energy conservation and potential vorticity dynamics for arbitrarily-structured

- 2336 C-grids. *Journal of Computational Physics*, 229(9), 3065–3090.
- 2337 Roache, P. J. (2002). Code verification by the method of manufactured solutions. *J. Fluids*
2338 *Eng.*, 124(1), 4–10.
- 2339 Rotundo, N., Kim, T.-Y., Jiang, W., Heltai, L., & Fried, E. (2016). Error analysis of
2340 a b-spline based finite-element method for modeling wind-driven ocean circulation.
2341 *Journal of Scientific Computing*, 69(1), 430–459.
- 2342 Rusanov, V. (1961). Calculation of interaction of non-steady shock waves with obstacles.
2343 *J. Comp. Math. Phys.*, 1, 267–279.
- 2344 Salari, K., & Knupp, P. (2000). *Code verification by the method of manufactured solutions*
2345 (Tech. Rep.). Sandia National Labs., Albuquerque, NM (US).
- 2346 Santilli, E., & Scotti, A. (2015). The stratified ocean model with adaptive refinement
2347 (somar). *Journal of Computational Physics*, 291, 60–81.
- 2348 Sarachik, E. S., & Cane, M. A. (2010). *The el nino-southern oscillation phenomenon*.
2349 Cambridge University Press.
- 2350 Shchepetkin, A. F., & McWilliams, J. C. (2005). The regional oceanic modeling system
2351 (ROMS): a split-explicit, free-surface, topography-following-coordinate oceanic model.
2352 *Ocean modelling*, 9(4), 347–404.
- 2353 Smith, G. D. (1985). *Numerical solution of partial differential equations: finite difference*
2354 *methods*. Oxford university press.
- 2355 Spatz, W. F., Smith, T. M., Demeshko, I. P., & Fike, J. A. (2015). Aeras: A next generation
2356 global atmosphere model. *Procedia Computer Science*, 51, 2097–2106.
- 2357 Stommel, H. (1948). The westward intensification of wind-driven ocean currents. *Eos*,
2358 *Transactions American Geophysical Union*, 29(2), 202–206.
- 2359 Strauss, W. A. (2007). *Partial differential equations: An introduction*. John Wiley & Sons.
- 2360 Strohmaier, E., & Dongarra, J. (2023). *Top 500, the list*. Retrieved 2023-08-01, from
2361 <https://www.top500.org/>
- 2362 Stroud, A. H. (1971). *Approximate calculation of multiple integrals*. Prentice-Hall.
- 2363 Taylor, M., Tribbia, J., & Iskandarani, M. (1997). The spectral element method for the
2364 shallow water equations on the sphere. *Journal of Computational Physics*, 130(1),
2365 92–108.
- 2366 Thomas, S. J., & Loft, R. D. (2002). Semi-implicit spectral element atmospheric model.
2367 *Journal of Scientific Computing*, 17(1), 339–350.
- 2368 Thuburn, J., Ringler, T. D., Skamarock, W. C., & Klemp, J. B. (2009). Numerical
2369 representation of geostrophic modes on arbitrarily structured C-grids. *Journal of*
2370 *Computational Physics*, 228(22), 8321–8335.
- 2371 Vallis, G. K. (2017). *Atmospheric and oceanic fluid dynamics*. Cambridge University Press.
- 2372 Versteeg, H. K., & Malalasekera, W. (2007). *An introduction to computational fluid*
2373 *dynamics: the finite volume method*. Pearson education.
- 2374 Vetterling, W. T., & Press, W. H. (1992). *Numerical recipes: example book c*. Cambridge
2375 University Press.
- 2376 Vitousek, S., & Fringer, O. B. (2014). A nonhydrostatic, isopycnal-coordinate ocean model
2377 for internal waves. *Ocean Modelling*, 83, 118–144.
- 2378 Walko, R. L., & Avissar, R. (2008). The ocean–land–atmosphere model (olam). part i:
2379 Shallow-water tests. *Monthly Weather Review*, 136(11), 4033–4044.
- 2380 Wang, D.-P. (1984). Mutual intrusion of a gravity current and density front formation.
2381 *Journal of Physical Oceanography*, 14(7), 1191–1199.
- 2382 Wang, Q., Danilov, S., & Schröter, J. (2008). Comparison of overflow simulations on different
2383 vertical grids using the finite element ocean circulation model. *Ocean Modelling*, 20(4),
2384 313–335.
- 2385 Wang, Q., Danilov, S., Sidorenko, D., Timmermann, R., Wekerle, C., Wang, X., ...
2386 Schröter, J. (2014). The finite element sea ice-ocean model (fesom) v. 1.4: formulation
2387 of an ocean general circulation model. *Geoscientific Model Development*, 7(2),
2388 663–693.
- 2389 Williamson, D. L., Drake, J. B., Hack, J. J., Jakob, R., & Swarztrauber, P. N. (1992).
2390 A standard test set for numerical approximations to the shallow water equations in

- 2391 spherical geometry. *Journal of Computational Physics*, 102(1), 211–224.
2392 Williamson, J. (1980). Low-storage runge-kutta schemes. *Journal of Computational Physics*,
2393 35(1), 48–56.
2394 Zarzycki, C. M., Levy, M. N., Jablonowski, C., Overfelt, J. R., Taylor, M. A., & Ullrich,
2395 P. A. (2014). Aquaplanet experiments using cam’s variable-resolution dynamical core.
2396 *Journal of Climate*, 27(14), 5481–5503.
2397 Zienkiewicz, O., Taylor, R., & Zhu, J. (2005). *The finite element method: Its basis and*
2398 *fundamentals*. Elsevier Butterworth-Heinemann.